NOTE TO USERS

DISSERTATION

INVESTIGATION OF NANOSTRUCTURES ON MoS_2 AND $MoTe_2$ PRODUCED BY VOLTAGE PULSES FROM A STM TIP AND Ar^+ AND He^+ BOMBARDMENTS

Submitted by
Joon Bum Park
Department of Chemistry

In partial fulfillment of the requirements
for the degree of Doctor of Philosophy
Colorado State University
Fort Collins, Colorado
Fall 2004

COLORADO STATE UNIVERSITY

MAY 12, 2004

WE HEREBY RECOMMEND THAT THE DISSERTATION PREPARED UNDER OUR SUPERVISION BY JOON BUM PARK ENTITLED "INVESTIGATION OF NANOSTRUCTURES ON MoS_2 AND $MoTe_2$ PRODUCED BY VOLTAGE PULSES FROM A STM TIP AND Ar^+ AND He^+ BOMBARDMENTS" BE ACCEPTED AS FULLFILLING IN PART REQUIREMENTS FOR THE DEGREE OF DOCTOR OF PHILOSOPHY

Committee on Graduate Work

Elliot Bernstein

David Grainger

Eugene Chen

John Mahan

Adviser-Bruce Parkinson

Department Head

ABSTRACT OF DISSERTATION

INVESTIGATION OF NANOSTRUCTURES ON MoS_2 AND $MoTe_2$ PRODUCED BY VOLTAGE PULSES FROM A STM TIP AND Ar^+ AND He^+ BOMBARDMENTS

MoS_2 and $MoTe_2$ have been of interest due to their catalytic activity for hydrodesulfurization (HDS) where organic sulfur is removed from petroleum and coal feedstocks by reaction with hydrogen gas to form H_2S. The catalytic activity of MoS_2 and $MoTe_2$ for HDS has been associated with exposed Mo atoms at the edge sites and basal plane defects (sulfur or tellurium vacancies). In these studies, the catalytic sites (nanostructures) on MoS_2 and $MoTe_2$ crystals have been fabricated by bombardments with Ar^+ and He^+ as well as voltage pulses from a tip of STM.

Nanostructures were fabricated on natural MoS_2 crystals by bombardment with Ar^+ and He^+ with energies ranging from 100 eV to 5 keV. Ar^+ with energies of 100 eV or less remove very few, if any, sulfur atoms from the surface but STM and XPS studies reveal that the electronic structure of the MoS_2 surface is altered. Ar^+ with energies greater than 100 eV have a higher probability of sputtering sulfur atoms from the surface, producing protrusion-like structures. On the basis of XPS and bias dependent STM studies, the protrusions could be associated with sulfur atom vacancies. He^+ sputtering of MoS_2 showed similar trends in nanostructure fabrication to Ar^+ sputtering. However, it produced smaller nanostructures. He^+ with the energy of 750eV selectively removed 1 ~ 3 sulfur atoms. These vacancies in STM images with the negative sample biases appear as bright ring or triangular shapes. These bright features are associated with exposed Mo atoms below the basal plane from the current imaging tunneling spectroscopic (CITS) analysis.

We have used the STM to generate atomic scale nanostructures on $MoTe_2$ and MoS_2 by applying voltage pulses between –10 V and 10V. The voltage pulse method showed that there are distinct threshold voltages for surface modification of $MoTe_2$ and

MoS_2. It was found that the geometry of STM tips plays an important role in nanostructure fabrication. The polarity dependence of nanostructure fabrication was explained by the difference of the magnitude of applied electric fields.

Joon Bum Park
Department of Chemistry
Colorado State University
Fort Collins, CO 80523
Fall 2004

Acknowledgments

I would like to thank my advisor Dr. Bruce Parkinson for his financial and intellectual supports. Former graduate students, C. B. France and P. F. Schroeder, are acknowledged for their assistance in many experiments and helpful discussions pertaining this work. I would like to also thank the Parkinson group, Y. Lu, A. Chick, D. Seley, and M. Woodhouse, J. Tomlinson, and S. Ushiroda, for their supports of my research efforts and understanding.

I would like to offer special thanks to my parents during my graduate studies. I would like to thank Eu-kyu Park and Bu-sa Jun for their emotional support and especially for their financial support. Kwang-nam Kim, and Jung-ok Lim are acknowledged for their helpful guidance. I would like to thank my sister and brother, Ji-eun Park and Young-bum Kim for their emotional support. Ha-min Bong, Se-eun Kim, and Joon-hyeng Kim are acknowledged for their interests on my work.

Finally, I would like to specially thank my wife and children, Se Young, Sinae, and Siwon for their endurance, emotional support, and their health during my prolonged academic career.

Joon Bum Park
Department of Chemistry
Colorado State University
Fort Collins, CO 80523
Spring 2004

Table of Contents

Index of Figures

Objectives:

Hydrodesulfurization (HDS) is the catalytic removal of organic sulfur containing compounds from petroleum and coal feedstock by reacting with hydrogen gas and catalysts.[1-3] Current environmental regulations require a substantial decrease in the sulfur content of raw petroleum during processing. Additionally, sulfur in raw petroleum poisons catalysts used in many steps of the refinement process, thus adding substantial costs to the finished products. Understanding the mechanism of catalysts and the nature of active sites for the HDS process will be essential for generating catalysts with superior efficiency and resistance to poisoning.[4] Industrial catalysts typically consist of MoS_2 crystallites on alumina supports promoted with Ni or Co.[5] The catalytic activity of MoS_2 for HDS has been associated with edge sites (exposed Mo atoms), which are more numerous on small particles employed in supported HDS catalysts.[6-9] Basal plane defects (exposed Mo atoms) produced at high temperatures during HDS have also been proposed to be active catalytic sites.[10,11]

In this research, we attempt to create individual catalytic sites (exposed Mo atoms below basal plane) on MoS_2 and $MoTe_2$ surfaces using two methods. The first method involves the selective removal of chalcogenide atoms (sulfur or tellurium) from the basal plane via application of voltage pulses from a tip of scanning tunneling microscope

(STM) operating in ultrahigh vacuum (UHV). By varying the magnitude of the applied voltage pulses, we will produce reaction sites with a variety of sizes and shapes. Atoms will be removed individually or in groups of adjacent atoms to prepare a specific geometry of exposed metal sites. There may be significant reactivity differences for HDS among the catalytic sites due to the different coordination of the exposed Mo atoms. The different morphologies and electronic properties of the catalytic sites (vacancies) will be investigated and characterized by STM and STS (Scanning Tunneling Spectroscopy). One objective of this research is to establish reproducible voltage pulse conditions including voltage pulse height, pulse duration, and current to prepare sulfur and tellurium atomic vacancies in a controlled fashion.

The second method is to sputter the MoS_2 surface with Ar^+ or He^+ ions to selectively remove sulfur atoms from the basal plane. The sizes of sulfur atomic vacancies (the numbers of removed sulfur atoms) are strongly influenced by the ion energies and ion masses due to different momentum transfer to the sample. We will attempt to determine optimum sputtering conditions for the controlled production of reaction sites of a variety of sizes and shapes. The morphologies of the generated catalytic sites will be investigated by STM and their electronic states will be characterized by both X-ray photoelectron spectroscopy (XPS) and scanning tunneling

spectroscopy (STS). Future studies will use the created sulfur and tellurium vacancies to study HDS reactions from individual catalytic sites by dosing the surface with sulfur containing molecules, including thiophene and its derivatives.

References

[1] R. R. Chianelli, Catal. Rev. -Sci. Eng. **34,** 361-393 (1984).

[2] T. Kabe, A. Ishihara, and W. Quian, *Hydrodesulfurization and Hydrodenitrogenation* (Kodansha, Tokyo, 1999).

[3] P. T. Vasudevan and J. L. G. Fierro, Catal. Rev. -Sci. Eng. **38,** 161 (1996).

[4] J. G. Kushmerick, S. A. Kandel, P. Han, J. A. Johnson, and P. S. Weiss, J. Phys. Chem. B **104,** 2908-2988 (2000).

[5] R. Prins, V. H. J. D. Beer, and Somorjai, Catal. Rev. -Sci. Eng. **331,** 1-41 (1989).

[6] S. Helveg, J. V. Lauritsen, I. Lagsgaard, J. K. Stensgaard, J. K. Norskov, B. S. Clausen, H. Topsoe, and F. Besenbacher, Phys. Rev. Lett. **84,** 951 (2000).

[7] M. Daage and R. R. Chianelli, J. Catal. **149,** 414-417 (1994).

[8] J. V. Lauritsen, S. Helveg, I. Lagsgaard, B. S. Clausen, H. Topsoe, and F. Besenbacher, J. Catal. **197,** 1 (2001).

[9] M. V. Bollinger, J. V. Lauritsen, K. W. Jacobsen, J. K. Norskov, S. Helveg, and F. Besenbacher, Phys. Rev. Lett. **87,** 196803 (2001).

[10] S. L. Peterson and K. H. Schultz, Langmuir **12,** 941-945 (1996).

[11] C. G. Weigenstein and K. H. Schultz, J. Phys. Chem. B **103,** 6913-6918 (1999).

Chapter 1.

Introduction to Scanning Tunneling Microscopy (STM), Transition Metal Dichalcogenides (TMD's), and Hydrodesufurization

1.1 Principles of Scanning Tunneling Microscopy (STM)

Since the invention of the scanning tunneling microscopy (STM) by G. Binning and H. Rohrer in 1982[1], this imaging technique has made a dramatic impact in fields as diverse as material science, semiconductor physics, biology, electrochemistry, surface chemistry and catalysis. The main reason for this huge influence of STM in science is that it provides three-dimensional (3-D) real space images of a surface with atomic scale resolution and allows for spatially localized spectroscopic measurements of surface

structures. In this section, basic principle of STM, its spectroscopic applications, and STM tip-fabricating methods will be discussed.

Principle of electron tunneling process

In STM, an atomically sharp tip is held within electron tunneling distance (less than 10 Å) from the sample surface and a potential is applied between the tip and sample (usually from a few tenths of volts to several volts). Electrons from a nearly atomically sharp tip tunnel into the sample (or vice versa) depending polarity of the applied bias. As the STM tip is raster scanned across the surface, under the control of piezoelectric actuator, a feedback mechanism senses the tunneling current to produce topological images of semiconducting or conducting materials.

STM operation relies on a basic quantum mechanical principle, electron tunneling through a barrier. In classical mechanics, an electron with energy E, momentum p_z (in one dimension), and the mass m will not penetrate a potential barrier when the electron energy E is less than the potential barrier U(z), according to

$$U(z) = E - \frac{p_z^2}{2m} \tag{1.2.1}$$

Therefore, the condition E > U(z) should be satisfied for electrons to climb over the potential barrier. However, quantum mechanics allows for electron tunneling through potential barriers. In quantum mechanics, the electron is described by a wave function, solutions of the Schrödinger equation, Ψ(z).

$$-\frac{h^2}{8\pi^2 m}\frac{d^2}{dz^2}\Psi(z) + U(z)\Psi(z) = E\Psi(z) \qquad (1.2.2)$$

where h is a Planck's constant. When the electron energy E is less than U(z) (classically not allowed region), the solutions are

$$\Psi(z) = \Psi(0)e^{-\kappa z} \quad \text{where} \quad \kappa = \frac{2\pi\sqrt{2m(U-E)}}{h} \qquad (1.2.3)$$

From above equation (1.2.3), we can see that there is a finite possibility that an electron can tunnel through the barrier even when E < U(z). The absolute square, $|\Psi(z)|^2$, of the wave function gives the probability that an electron will be found at a point z. This tunneling phenomenon can be observed when the tip and sample are close but not in contact [Figure 1.1.1].

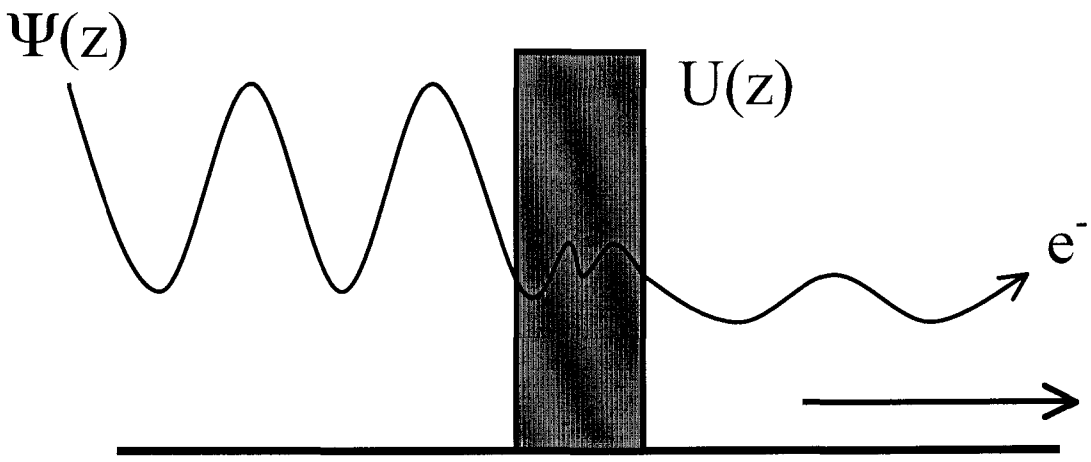

Figure 1.1.1. The electron tunneling process. In classical mechanics, an electron with energy less than the potential barrier height U(z) will not penetrate the barrier. However, quantum mechanics allows penetration with a finite probability via tunneling

When the tip is close to a metal or semiconductor surface, but not in contact, there will be an energy barrier between tip and sample as shown in Figure 1.1.2. If there is no applied bias voltage, the Fermi levels of the tip and sample should be same and there will be no net flow of electrons since tunneling occurs equally in both directions [Figure 1.2.1 (a)]. If a bias voltage is applied between the tip and sample, the shape of energy barrier is changed and there is a driving force for electrons to tunnel from filled states on one side to empty states on other side of the barrier [Figure 1.2.1 (b)]. The probability that an electron will penetrate the barrier is related to the tunneling current (I) and it decays exponentially with the barrier width z as

$$I \propto e^{-\kappa z} \tag{1.2.4}$$

The tunneling decay constant (κ) is given by:

$$\kappa = 2\pi(2m\phi)^{\frac{1}{2}}/h \tag{1.2.4}$$

where ϕ is the effective local potential barrier height *(U-E)* in 1.2.3, h is a Planck's constant and m is the mass of the tunneling electrons. This equation indicates that for every 1Å of distance between the tip and sample the tunneling current will decrease by one order of magnitude.

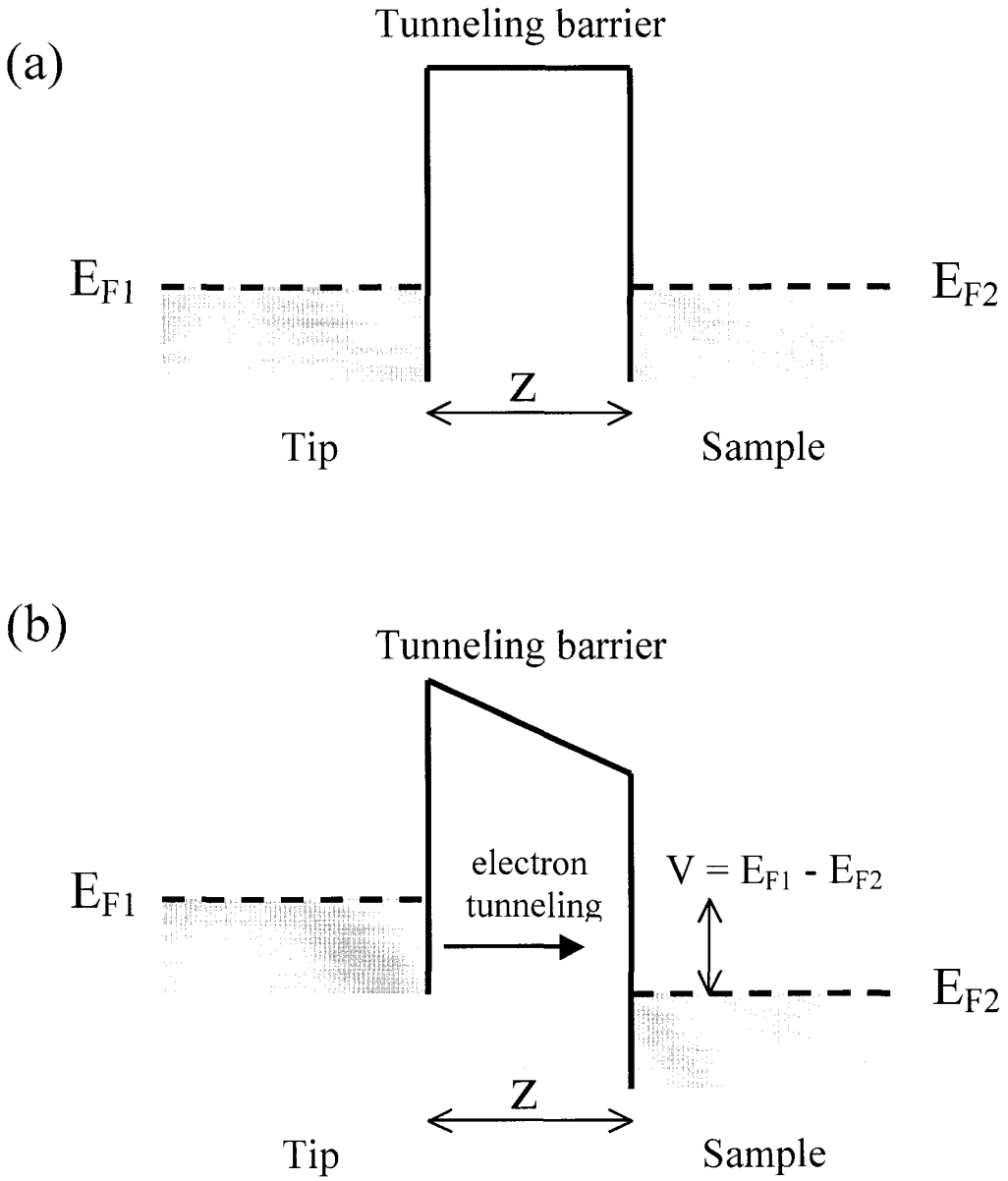

Figure 1.1.2. The energy levels separated by vacuum barrier (a) with no bias applied between the tip and sample (b) with negative tip bias. Fermi levels for the tip and sample are indicated by E_{F1} and E_{F2}, respectively. The applied bias V is E_{F1} - E_{F2} and z is the thickness of the barrier.

Moving the atomically sharp tip across the sample surface and monitoring the tunneling current allows for the production of high-resolution images. There are two common methods for producing an STM image: constant height mode and constant current mode.[2] In the constant current mode [Figure 1.1.3 (a)], the feedback mechanism sets a constant current while a constant bias is applied between the tip and sample. As the tip is raster scanned over the surface, the vertical position of the tip is altered by a piezoelectric actuator to maintain a constant tip sample current. The signal required to alter the vertical tip position produces the surface image, which represents a constant charge density contour of the surface. While this constant current mode appears straightforward, it is important to remember that the images produced with this technique is a convolution of both height and electronic effects of the sample surface. The detail discussion of this point will be presented in later chapters. This imaging mode is most widely used and all of the images in this thesis are obtained using this method.

An alternative method is constant height mode where a constant tip height and constant applied bias are simultaneously maintained. [Figure 1.2.3 (b)] The tip is then raster scanned over the sample surface. A variation in current during scanning a surface reflects the atomic scale topography. An advantage to this mode is that scan rates are not limited by response of the STM feedback mechanism, provided that the scan speed is not

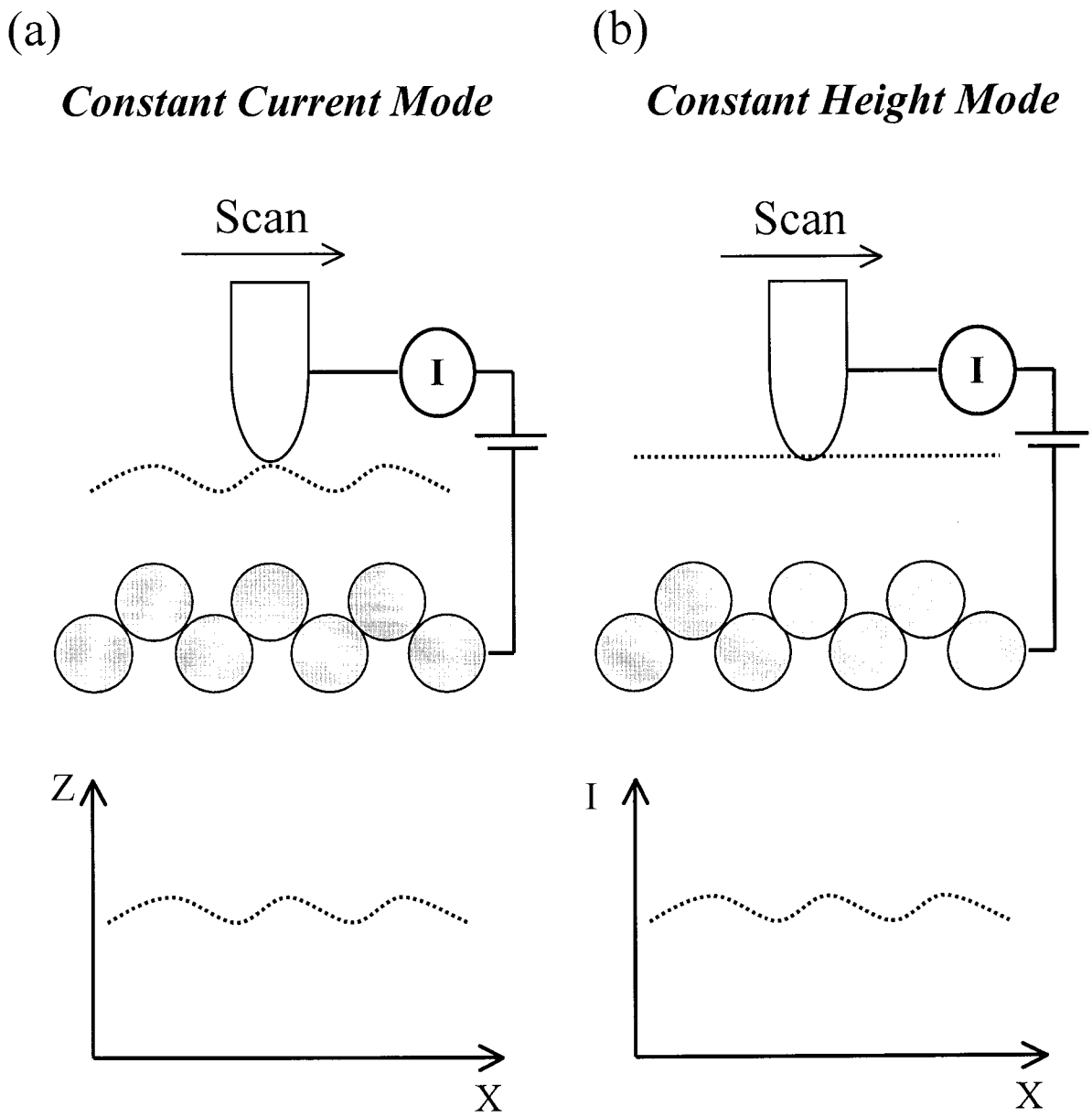

Figure 1.1.3. Two possible modes of operating STM. (a) constant current mode (b) constant height mode

faster than the instrument preamplifier. However, the analysis of a rough surface with this constant height mode may cause the tip to crash into the surface, thus inducing damage on the tip and destroying the resolution of an atomically sharp tip.

STM tip fabrication

There has been considerable interest in making high performance STM tips, since the quality of STM tips is the most important factor in determining the resolution of STM images. The tip shape and its sharpness are the two most important parameters for obtaining reliable surface images. Too high an aspect ratio (tip length / tip radius) may result in a tip vibration during scanning, resulting in distortion of the images. Blunt tips will make it difficult to obtain atomic resolution images of the surface. STM tips are typically produced from metal wires of platinum iridium (Pt-Ir)[3,4], tungsten (W)[5-7], or gold (Au)[8], and many tip preparation techniques have been developed over the last decade (electrochemical etching[5,6], ion sputtering[9], electron bombardment[10], and cutting of the metal wire[11]). The electrochemical etching is known as a simple and fast method producing reproducible STM tips. This method will be discussed in detail later in this section.

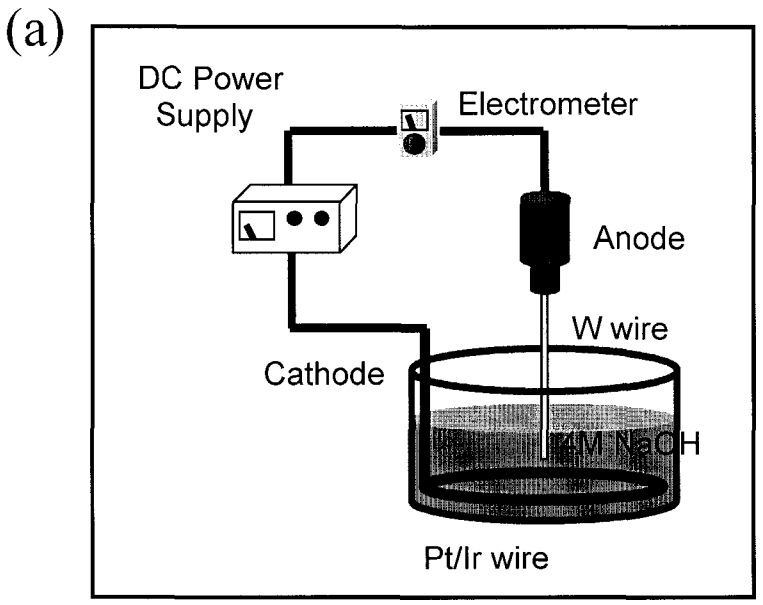

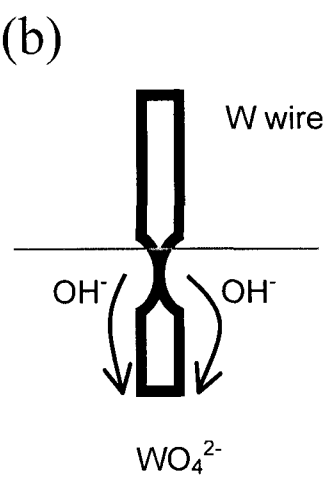

Cathode	$6H_2O + 6e^- \longrightarrow 3H_2(g) + 6OH^-$	$E^0 = -0.828V$
Anode	$W(s) + 8OH^- \longrightarrow WO_4^{2-} + 4H_2O + 6e^-$	$E^0 = 1.05V$
	$W(s) + 2OH^- + 2H_2O \longrightarrow WO_4^{2-} + 3H_2(g)$	$E^0 = 0.222V$

Figure 1.1.4. (a) Schematic diagram of the electrochemical cell shows the W wire (anode) being etched in 4M NaOH. The cathode consists of a Pt/Ir wire surrounding the anode. (b) Schematic illustration of the etching mechanism shows that the W wire is etched at air/electrolyte interface.

The electrochemical etching procedure usually involves the anodic dissolution of the metal wire electrodes. Etching occurs at the air/electrolyte interface when a positive voltage is applied to the wire (anode). Figure 1.1.4 (a) shows a schematic of the electrochemical cell. As a first step for preparing STM tips, the W wire was annealed in vacuum (resistively heated) for 3 hours to increase the crystallite size in the W metal wire. The annealed W wire is placed in the center of the cell and serves as the anode. The electrochemical etching cell consists of a beaker containing approximately 100 ml of 4 M NaOH and the metal wire is mounted on a micrometer so that its position relative to the surface of the electrolyte can be adjusted. The counter electrode (cathode) is a piece of Pt/Ir wire that is formed into a loop to fit inside the beaker.

The STM tips can be produced with either an alternating-current (AC) or a direct-current (DC) voltage. Each procedure yields a different tip shape. The AC etched tips have a conical shape and much larger cone angles than the DC etched tips whereas the DC etched tips have hyperboloid shapes, are much sharper than AC etched tips, and are preferable for high resolution STM imaging. All of the STM tips in our STM studies are prepared by a DC drop off method where etching occurs at the air/electrolyte interface causing the portion of wire in solution to drop off when its weight exceeds the tensile

strength of the etched or necked down region of wire [Figure 1.1.4 (b)]. The DC drop off method normally produces two tips simultaneously but the upper part is most often used in STM imaging. The cutoff time (etching time after separation of the wire for final formation of the tip) has an significant effect on the radius of curvature of the etched tip because the upper part will continue to be etched as long as it remains in the electrolyte under the applied potential. It has been shown that shorter the cut off times produced sharper tips.[12] The tip apex radii vary from 10 to 300 nm depending on the cutoff time. After the separation of the wire, the upper part was quickly removed and washed with HF solution to remove any oxide layer and then distilled water. Its structure was then investigated with an optical microscope. The tip is then mounted in a magnetic tip holder and loaded into the UHV system. Figure1.1.5 shows a Scanning Electron Microscope (SEM) images of an electrochemically etched W tip.

As mentioned earlier, the cut off time is a critical factor in the preparation of atomically sharp tips due to a continuous etching of a metal wire after a lower part drops off. A lot of work has been done to reduce this cut off time.[3,4,13-15] Nakamura and coworker showed that the tip apex radius could be reduced to as low as 8 nm when the etching cutoff time was shortened to 50 nsec by using a circuit that quickly shuts off the power supply automatically to prevent further etching.[13] In 1999, Muller, et. al. showed

that a tip with apex radius less than 10nm could be fabricated through a lamella drop-off technique.[16] The etching apparatus consists of a Ta plate (0.25 mm thickness) with a centered hole of 3mm diameter. The W wire is threaded through the hole and the upper end is fixed with a screw. The lower end is hanging over a plastic tube of 2 mm diameter. A drop of etching solution (2M NaOH) is given in the hole and a DC bias (2 V) is applied between the W wire and Ta plate. Even though a circuit did not precisely control the automatic shut-off, very sharp tips were obtained since the lower part of the tip was used instead of upper part that were subjected to the residual etching. We attempted to reproduce this method to obtain sharper tips. For a 0.38mm W wire, the etching lasts about 10min. the tip apex radius could be reduced to less than 10nm. Unfortunately, this method also showed poor performance due to the higher tip apex radius and asymmetry of the tip.

For the fabrication of sharper tips, we used a special power supply that was prepared in the electronic shop in the Department of Chemistry at CSU. At the end of etching, the potential between the anode (W wire) and cathode (Pt loop) is suddenly dropped as the lower part of the wire drops off. The power supply senses this voltage drop and automatically switches off the applied voltage within 500nsec. The rapid switching of the voltage results in very sharp tips with apex radii less than 30nm. Figure

(a)

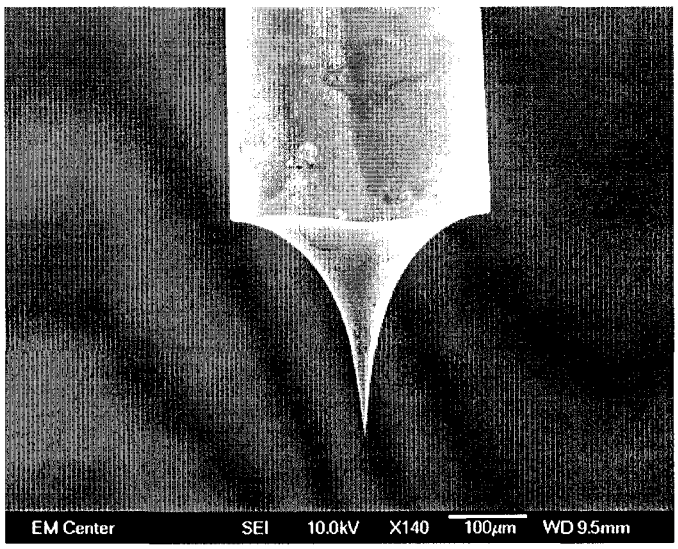

(b)

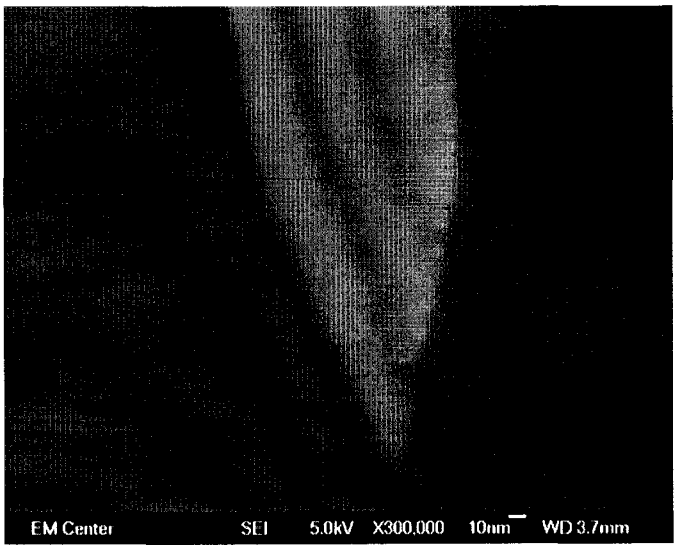

Figure 1.1.5. (a) a Scanning Electron Microscopy (SEM) image of electrochemically etched W tip (b) an SEM image of sharp W tip. This image shows a low resolution due to the tip vibration during the image measurement.

1.1.5(b) shows a Scanning Electron Microscope (SEM) image of an electrochemically etched W tip. The apex radius of the tip was determined to be about 10nm.

Scanning Tunneling Spectroscopy

As mentioned earlier, the STM images can contain both electronic and topological information about the sample surface. However, separating the contributions of electronic and geometric structure is not straightforward. One way of obtaining spectroscopic (electronic) information from the STM is scanning tunneling spectroscopy (STS) technique developed by Binning and Rohrer[1]. To perform STS experiments, the voltage is ramped between voltage set points (normally –2 V and 2 V) while the tip is positioned over a feature of interest and recording the tunneling current. Since during this measurement the feedback is deactivated, the current measurement is performed at a constant tip sample distance that is determined by the imaging voltage. This current measurement results in voltage vs. current (I-V) curves related to the electronic structure at a specific x and y location on the surface. Therefore, studying the bias dependent tunneling current using STS allows for the extraction of electronic information about surface structures on an atomic scale.

Acquisition of an I-V curve at every pixel within the topographic image would provide a complete picture of the local electronic states of the surface. This spectroscopic capability combined with topographic images of the surface is called current imaging tunneling spectroscopy (CITS). It allows us to correlate the electronic structure with surface topography. When the feedback loop is switched on, the tip height is adjusted to maintain a constant tunneling current, and a constant bias (imaging bias) is applied between the tip and sample, providing with a conventional topological surface image. When the feedback is deactivated, the tip remains at a constant height and the voltage applied between tip and sample is ramped and an I-V curve is measured. The voltage is then set back to the imaging bias and the feedback loop is switched back on. All of these processes allow for simultaneous generation of topographic images and spatially resolved I-V curve (current image).

To demonstrate the information we can obtain from the CITS, we will consider a simple energy diagram for a system consisting of a tunneling tip and semiconductor sample that are separated by a small vacuum gap [Figure 1.1.6 (a)]. When no bias is applied, the Fermi levels of tip and sample are at equilibrium. Application of a bias to the sample results in a shift of the energy levels upwards or downward depending on the polarity of the bias. For positive sample biases, the Fermi level of the sample shifts

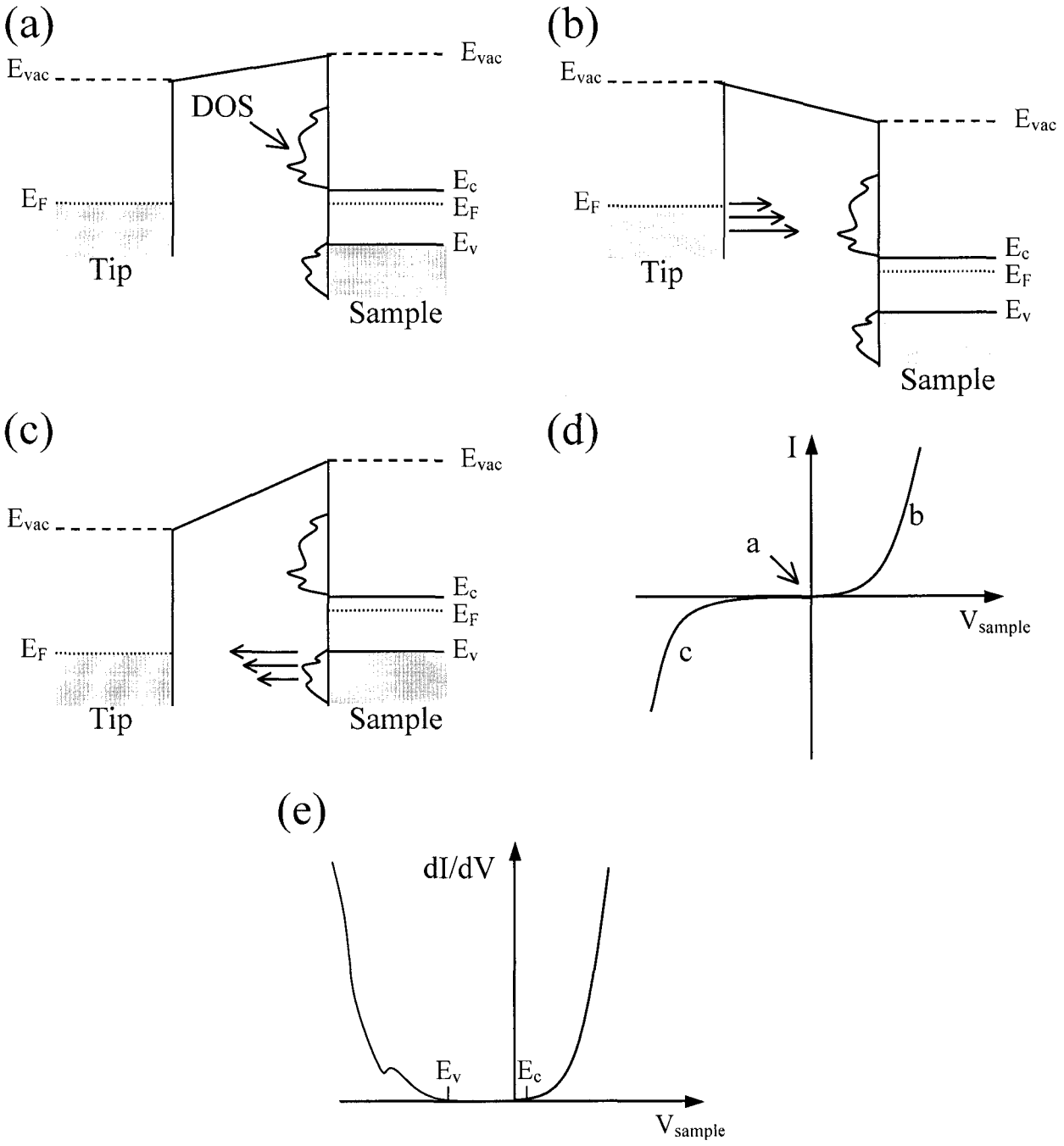

Figure 1.1.6. Potential energy level diagrams for tip and sample (n-type semiconductor) from a CITS. (a) The sample and tip are in equilibrium. (b) A negative bias is applied to the tip where electrons are tunneling from the tip and sample. (c) A positive bias is applied to the tip where electrons are tunneling from the sample to tip. (d) The scheme indicate I-V curve characteristic of n type semiconductor. (e) the scheme shows conductance (dI/dV) curve at the tip sample interface

downward by an amount of |eV|, and electrons tunnel from occupied states of the tip to unoccupied states of the sample [Figure 1.1.6 (b)]. With negative sample biases, electrons tunnel from occupied states of the sample to unoccupied states of the tip [Figure 1.1.6 (c)]. The polarity of the bias therefore determines whether the occupied or unoccupied electronic states in the sample are probed.

By varying the bias, it is possible to select the electronic states that contribute to the tunneling current and, in principle, we can measure the local electronic density of states (DOS) of the sample. As the bias voltage is ramped, electrons will tunnel out of and into the energy levels of the sample depending on a polarity. Figure 1.1.6 (d) shows a shape of I-V curve taken on n-type semiconductor. Points a, b, and c on the curve indicate bias conditions represented in the energy diagram shown in Figure 1.1.6 (a), (b), and (c), respectively. The first derivative (dI/dV) of current is related to the electronic density of states to a first approximation [Figure 1.1.6 (e)]. Detailed discussion of the correlation of conductance (dI/dV) with the DOS of materials will be presented in next section.

Correlation of STM images with STS

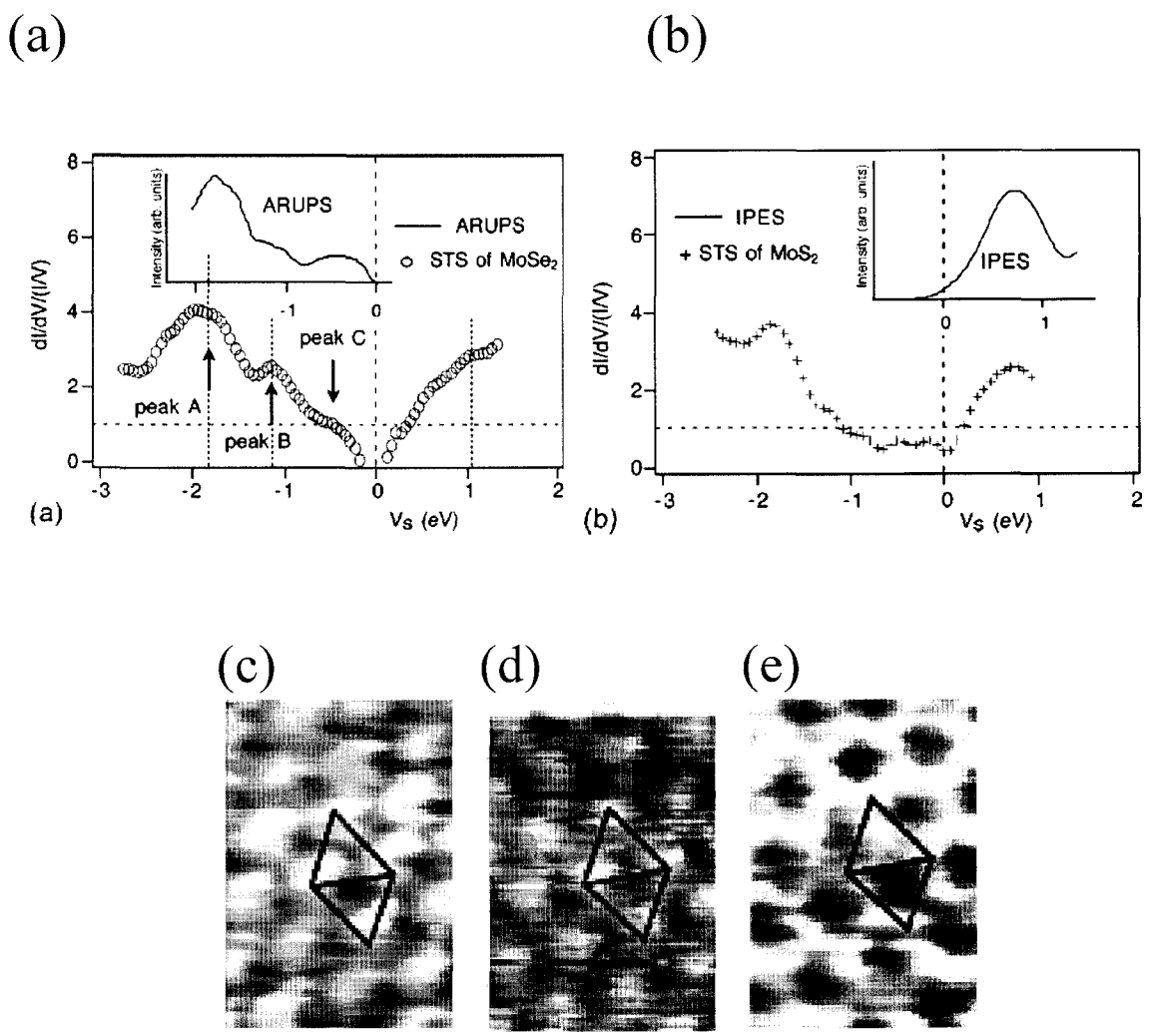

Figure 1.1.7. (a) Normalized differential conductance vs. sample bias relative to the Fermi energy of $MoSe_2$ (open circle). Upper curve shows a UPS spectrum (solid line). (b) Normalized differential conductance of MoS_2 and IPES spectrum (solid line). (c) ~ (e) topological image of 1.5 x 1.0 nm^2 area of MoS_2 (0001) at a tunneling current of 0.23 nA. The sample biases are (c) -0.31V (d) -1.08V and (e) -1.24V. (Ref 17)

Figure 1.1.7 (a) and (b) shows spatially averaged STS spectra (dI/dV, normalized differential conductance) of $MoSe_2$ and MoS_2 surfaces that were obtained by Murata and Koma by averaging more than a hundred I-V curves.[17] The STS spectra are compared with spectra obtained by phtoemission. The valence band of $MoSe_2$ and the conduction band of MoS_2 are investigated by ultra-violet photoelectron spectroscopy (UPS) and inverse photoemission spectroscopy (IPES), respectively. The spectrum of $MoSe_2$ in the negative sample bias region, representing the occupied states of sample, is very similar to the DOS obtained from UPS, while the spectrum of MoS_2 in the positive sample bias region, representing the unoccupied states of sample, is very similar to the DOS obtained from IPES. Therefore, the STS spectra (normalized differential conductance, dI/dV) obtained from the $MoSe_2$ and MoS_2 reflect their electronic DOS. Figure 1.1.7 (c) – (e) show bias dependent STM images from CITS at three different sample biases where honey-comb and spherical structures were observed. When the sample bias is close to zero, the spherical shape of atoms is observed, whereas the honey-comb structures are observed at a higher negative sample bias (-1.3V).[17] Since $MoSe_2$ and MoS_2 are layered compounds, consisting of stacked chalcogenide-metal-chalcogenide layers held together only by van der Waals forces (this will be discussed in detail in next chapter), the images of Figure 1.1.7(c) and (e) come from localized atomic orbital of chalcogen (p_z orbitals of

S or Se) and low lying in plane orbitals (p_x and p_y orbitals) of chalcogen. Figure 1.1.7 (d) will be a mixed image of Figure 1.1.7 (c) and (e). Therefore, these bias dependant STM images indicate that there are at least two spatially distinct occupied states near the surface. The peak C in Figure 1.1.7 (a) represents the localized atomic orbitals (p_z) of the chalcogen at ~ -0.7V and the peak B indicates in plane orbitals (p_x and p_y) at –1.2V.

Another example of the utility of CITS is to determine the energy level of donors or acceptors in the near surface region of a semiconductor.[18] Figure 1.1.8 (a) shows a constant current image of low temperature grown (LTG) p-type GaAs layer where excess As gives rise to a high concentration of As anti-site defects (As_{Ga}). This image was obtained at a negative sample bias and numerous protrusions, associated with the As anti-site defects, are clearly seen. The curve (1) and (2) in Figure 1.1.8 (b) indicate tunneling spectra acquired from the substrate and an As anti-site defects in the LTG layer, respectively. The Fermi level of the substrate (curve 1), located at 0V, is closer to valence band edge due to the p-type doping of the substrate and no mid gap states are observed. However, the spectrum from As anti-sites contains a contribution from the mid gap states, located at –0.5V from the E_F. This peak is associated with the donor levels of the bulk antisite defects in GaAs. Thus, using the CITS method, one can actually map out the filled and empty states of the surface at different voltages.

(a)

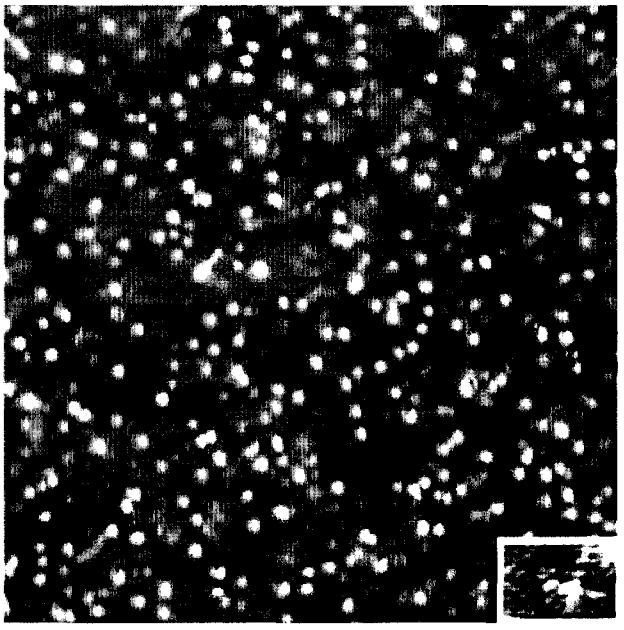

(b)

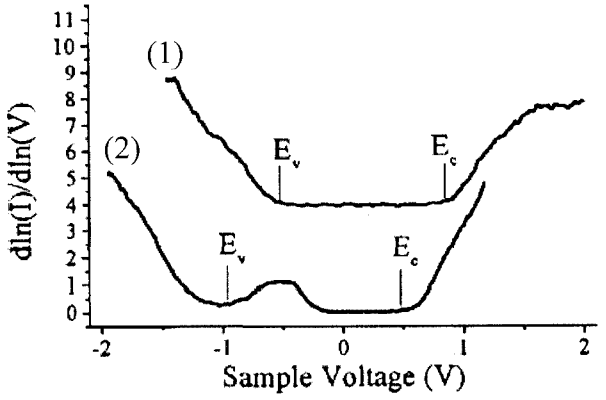

Figure 1.1.8. (a) Constant current image of the (110) cleaved face of LTG-GaAs, obtained from a sample bias of -2.0V. The inset shows an enlarged view of a point defect where satellites peaks can be observed surrounding the central core. (b) Tunneling spectra obtained from (1) the substrate and (2) an As antisites. A midgap states appears within the band gap of spectrum. (Ref. 18)

REFERENCES

[1] G. Binning, C. Roher, and E. Weibel, Phys. Rev. Lett. **49,** 57 (1982).

[2] D. Bonnell, *Scanning probe microscopy and spectroscopy*, Vol. 2, second ed. (Wiley VCH, New York, 2001).

[3] L. Libioulle, Y. Houbion, and J.-M. Gilles, Rev. Sci. Instrum. **66,** 97 (1995).

[4] M. Klein and G. Schwitzgebel, Rev. Sci. Instrum. **68,** 3099 (1997).

[5] R. Zahang and D. G. Ivey, J. Vac. Sci. Technol. B **14,** 1 (1996).

[6] L. Ottaviano, L. Lozzi, and S. Santucci, Rev. Sci. Instrum. **74,** 3368 (2003).

[7] J. P. Song, N. H. Pryds, K. Glejbol, K. A. Morch, A. R. Tholen, and L. N. Christensen, Rev. Sci. Instrum. **64,** 900 (1993).

[8] M. Fotino, Rev. Sci. Instrum. **64,** 159-166 (1993).

[9] P. Hoffrogge, H. Kopf, and R. Reichelt, J. Appl. Phys. **90,** 5322 (2001).

[10] I. Ekvall, E. Wahlstrom, D. Claesson, H. Olin, and E. Olsson, Meas. Sci. Technol. **10,** 11 (1999).

[11] J. Garnes, K. Kraph, K. A. Morch, and A. R. Throlen, J. Vac. Sci. Technol. A **8,** 441 (1990).

[12] O. L. Guise, J. W. Ahner, M. Jung, P. C. Goughnour, and J. T. Yates, Nano Lett. (2002).

[13] Y. Nakamura, Y. Mera, and K. Maeda, Rev. Sci. Instrum. **70,** 3373 (1999).

[14] J. P. Ibe, J. Bey, P. P., S. L. Brandow, R. A. Brizollara, N. A. Burnham, D. P. Diella, K. P. Lee, C. R. K. Marrian, and R. J. Colten, J. Vac. Sci. Technol. A **8,** 3570 (1990).

[15] H. Lemke, T. Goodenhenrich, H. P. Bochem, U. Hartmann, and C. Heiden, Rev. Sci. Instrum. **61,** 2538 (1990).

[16] A. D. Muller, F. Muller, M. Hietschold, F. Demmimg, J. Jersch, and K. Dickmann, Rev. Sci. Instrum. **70,** 3970-3972 (1999).

[17] H. Murata and A. Koma, Phys. Rev. B **59,** 10327 (1999).

[18] B. Grandidier, X. Broise, D. Stievenard, C. Delerue, M. Lannoo, M. Stellmacher, and J. Bourgoin, Appl. Phys. Lett. **76,** 3142 (2000).

1. 2 STM Studies of Transition Metal Dichalcogenides (TMDs)

Structure and properties of transition metal dichalcogenide (TMDs)

Transition metal dichalcogenides (TMDs) are layered materials that consist of a repetition of a three-layer sandwich; top chalcogenide layer (S, Se, or Te), a middle transition metal layer (Ti, V, Nb, Mo, Ta, or W), and a bottom chalcogenide layer [Figure 1.2.1]. The bonding within each sandwich is covalent and neighboring sandwiches are held together mainly by van der Waals forces. The coordination geometry around the transition metal atoms can either be octahedral or trigonal prismatic. The 1T type of TMD's has octahedral coordination of the metal atoms with respect to the chalcogen atoms [Figure 1.2.2 (a)]. Each unit cell consists of one transition metal layer surrounded by two chalcogenide layers. The 2H phases have trigonal prismatic coordination of the metal atoms with respect to the chalcogen atoms and each unit cell consists of two MX_2 sandwiches [Figure 1.2.2 (b)].

The TMD's have wide range of electrical properties ranging from metal ($NbSe_2$ and WTe_2), semiconductor (MoS_2, $MoSe_2$, $MoTe_2$) to insulator (HfS_2).[1] The MoS_2 and WSe_2 samples, that we used in these experiments, are layered metal dichalcogenide

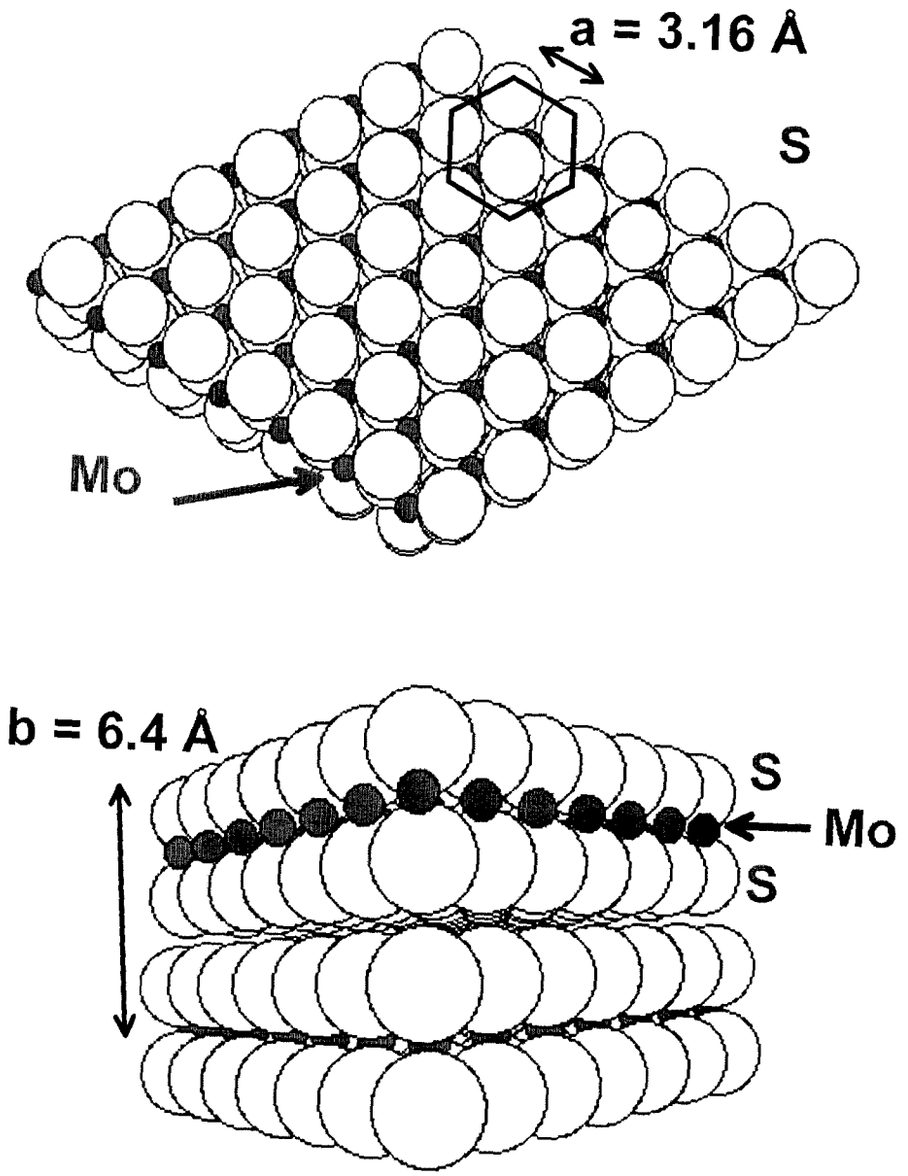

Figure 1.2.1. Structure of transition metal dichalcogenice (TMD). This figures indicate a structure of MoS_2.

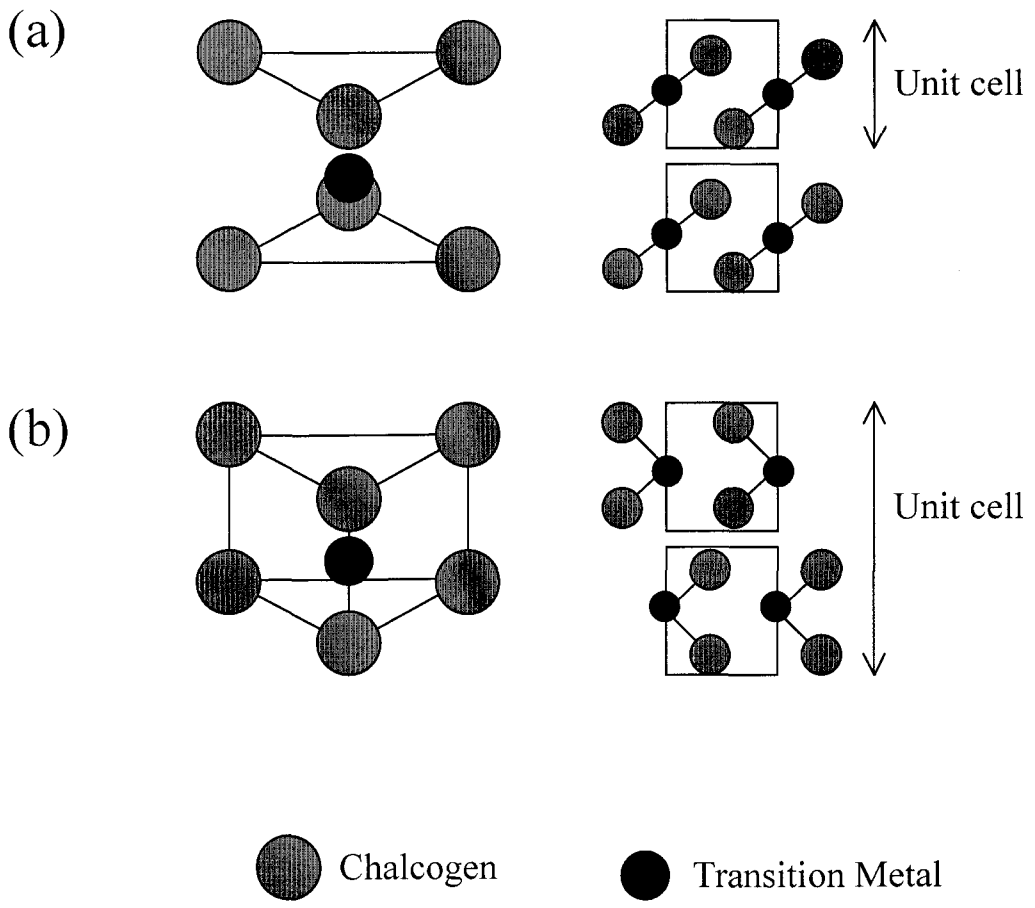

Figure 1.2.2 Structure of (a) 1T-phase and (b) 2H-phase. The cross sections are shown perpendicular to the (1000) planes. (c) 4H phase structure is alternating layers of T and H

semiconductors both with a similar band gap of ~ 1.2eV.[2] The layers are held together by van der Waals forces and can be easily peeled off to expose a clean surface for surface investigation. The surface of TMD's (basal plane) consisting of chalcogenide atoms are relatively inert due to the lack of dangling bonds. Therefore atomic resolution STM studies can be performed even in air or liquid phases.

Atomic scale STM studies of MoS_2 and $MoTe_2$

We have obtained atomically resolved STM images of TMD surface in UHV. Figure 1.2.3 (a) and (b) show STM images of $MoTe_2$ and MoS_2 acquired with a sample bias of 0.5V and - 0.1V ($I_{tunneling}$ = 0.1nA), respectively. Hexagonal arrays of sulfur atoms on the MoS_2 surface are clearly visualized whereas the $MoTe_2$ surface exhibits a distortion of the hexagonal array of Te atoms due to the thermal drift during imaging. The measured lattice constants for $MoTe_2$ and MoS_2 are 0.37nm and 0.32nm, quite close to the reference value [a = 0.352nm ($MoTe_2$) and 0.316nm(MoS_2)]. [3,4]

Principles of charge transfer in STM

The bias applied between the tip and sample causes the conduction band (E_c) and valence band (E_v) of a semiconductor to bend near the surface. For example, n-type MoS_2

(a)

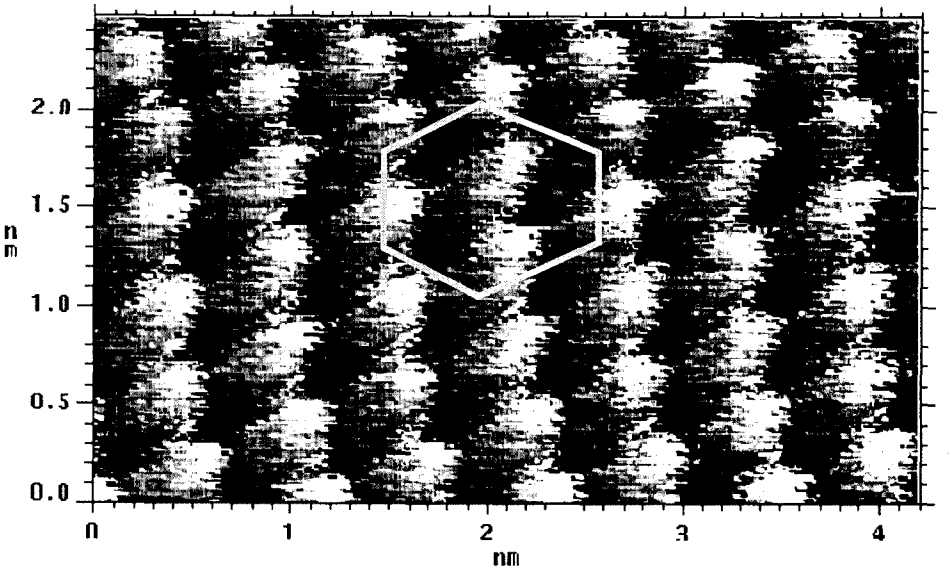

(b)

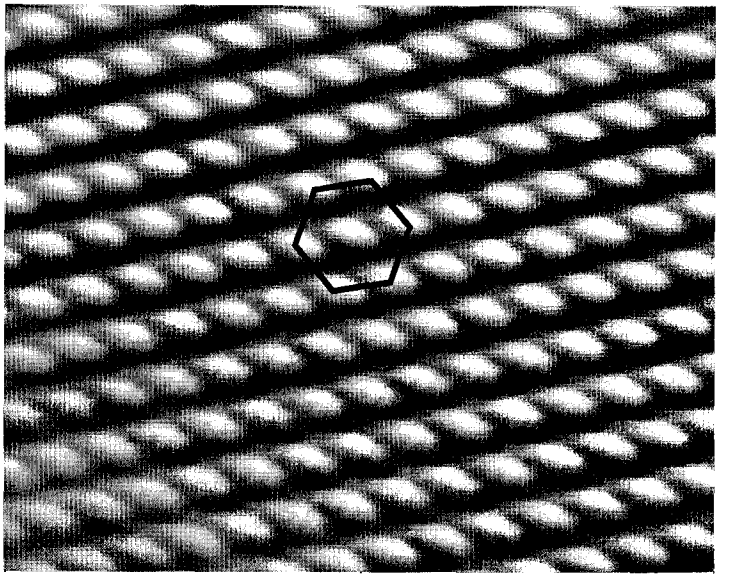

Figure 1.2.3. Typical STM images of (a) $MoTe_2$ surface (V_{sample} = 0.5Vand I = 1.0nA) and (b) MoS_2 surface (V_{sample} = -0.1V and I = 1.0nA)

has electrons as majority carriers. For an electron to tunnel from the sample to the tip, the MoS_2 sample should be biased negative relative to the metallic tip. This negative sample bias (positive tip bias) lowers the E_F of the tip, and E_c and E_v of MoS_2 to bend down since the E_F of MoS_2 equilibrates with that of the tip [Figure1.2.4 (a)]. Thus, the resulting electric fields created between the tip and sample favor the flow of the electrons. This causes an accumulation of negative charge at the MoS_2 surface. Likewise, positive charges will be accumulated at the surface of p-type MoS_2 with positive sample bias voltage. Depletion of n-type MoS_2 occurs when a negative bias is applied to the tip, and thus the E_F of the tip is raised above the E_F of MoS_2 [Figure1.2.4 (b)]. The E_c and E_v of the sample will bend up, and the electric field induces the electrons to flow from the tip to the sample. The negative bias to the metallic tip deposits negative charge on the metal and requires a corresponding net positive charge at the MoS_2 surface, resulting in depletion of electrons from the region from the surface. If a higher positive sample bias is applied to the sample, the bands at the semiconductor surface bend up more strongly. In fact, a sufficiently large voltage can bend E_F below E_i (intrinsic level). This is a particularly interesting case, since $E_i >> E_F$ implies a large hole concentration in the valence band [Figure1.2.4 (c)]. This is called inversion due to the accumulation of

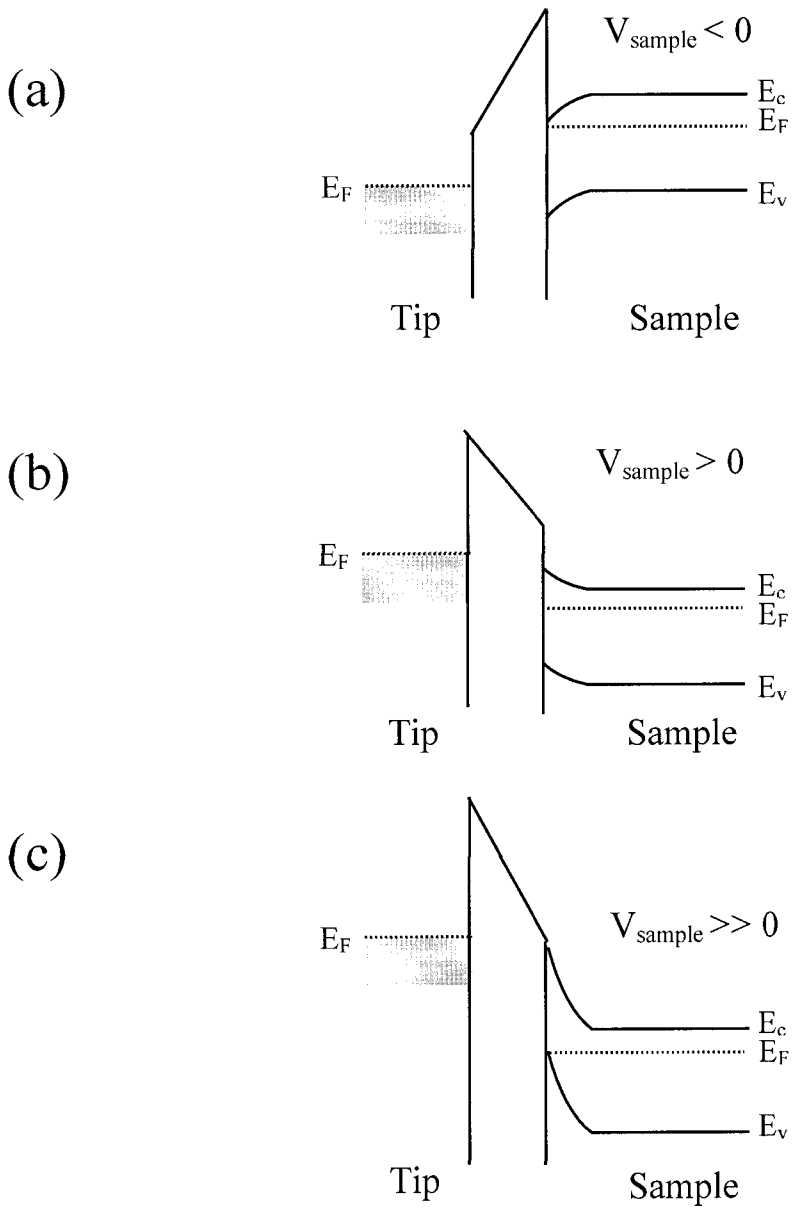

Figure 1.2.4. (a) A negative sample voltage causes electron "accumulation" in the n-type semiconductor. (b) A positive sample voltage causes electron 'depletion" in the n-type semiconductor. (c) A large positive sample voltage causes "deep depletion or inversion" in the n-type semiconductor.

holes at the n-type semiconductor. These electronic effects will be discussed in detail in next sections to aid the interpretation of the electronic effects of natural defects and prepared nanostructures on MoS_2.

Observations of protrusions and depressions of MoS_2

Various natural defects such as ring shape structures, topological hillocks, and depressions have been observed on natural MoS_2 crystal surfaces with STM.[5-13] Some of these natural defects have been interpreted as impurities intercalated between van der Waals layers during the natural formation process.[5,7,12] Figure 1.2.5 (a) and (b) show typical STM images of a natural MoS_2 crystal of an area (150 x 150 nm^2) containing impurities at a positive (0.5 V) and negative sample bias (-0.5 V), respectively. The arrows in Figure 1.2.5 point to the same natural defect and highlight how their topological shapes were changed depending on the polarity of the applied bias. All protrusions and depressions shown have a similar spatial extent of 5~8 nm and their apparent heights vary from 1.0nm above the surface to 0.8nm below the surface.

These interesting topological features on MoS_2 surfaces have been previously reported by several research groups, and their chemical natures and electronic effects

(a)

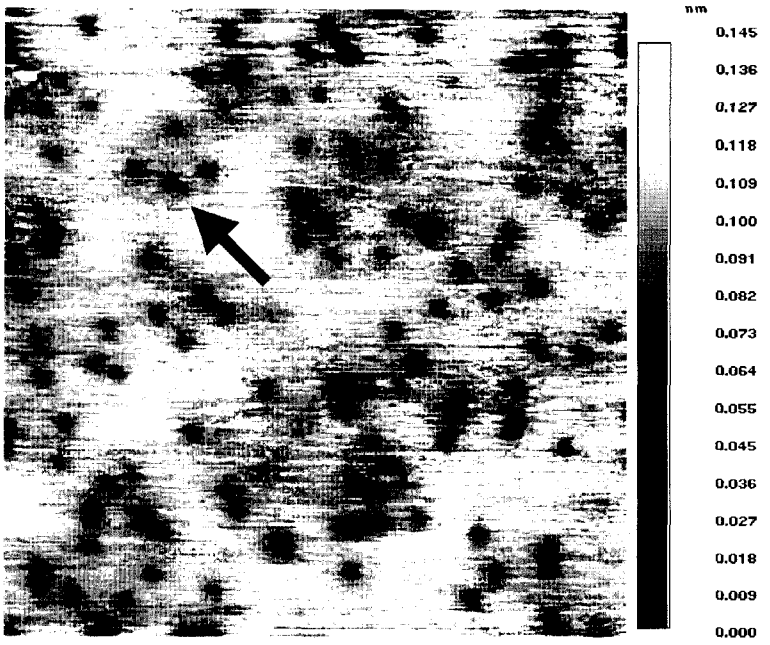

(b)

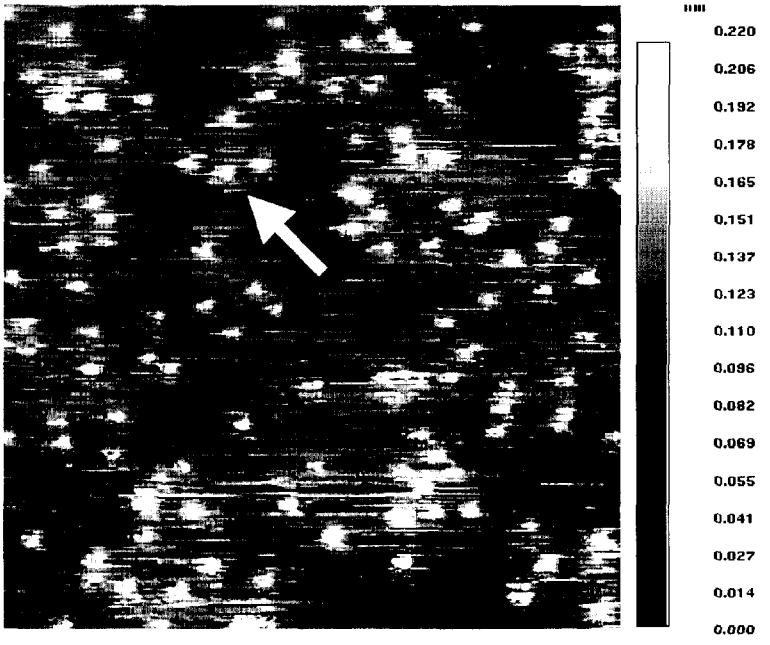

Figure 1.2.5. STM images of electronic effects from natural defects in MoS_2 (150 x 150 nm^2). The topological protrusions and depressions are attributed to natural defects. These images were acquired at (a) a positive sample bias of 0.5Vand (b) a negative sample bias of -0.5V with a tunneling current of 0.1nA. Note that the topological depressions at 0.5V are changed into topological protrusions at -0.5V and each arrow indicates the same natural defect.

have been intensively investigated for several years.[6,7,12,13] However, the exact chemical nature of these natural defects is still debated. Weimer *et al.* observed island-shaped features with diameters ranging from 5 to 10nm on MoS_2 surface. It was proposed that these islands might be due to interstitial contaminants between sulfur layers.[12] Heckl *et al.* reported ring-shaped protrusions on the surface of MoS_2 with ring diameters ranging from 1.5nm to 4 nm with a height of about 0.3nm.[13] They suggested that the rings could be organic or biological remnants intercalated when the mineral was formed. This was based on their comparison of secondary ion mass spectrometry (SIMS) measurements of their natural crystals with a synthetic MoS_2 crystal where no ring-shape feature was imaged with the STM. The mass spectra of the two materials were identical except for the presence of carbon in the spectrum of the natural MoS_2. Therefore, the sources of the ring-shaped features were attributed to the organic molecules such as benzene in the natural MoS_2.

A similar STM study of natural MoS_2 by Permana *et al.*[7] showed that the ring structures and small protrusions were due to the presence of vanadium and fluoride ions that were detected by SIMS. They could not detect the carbon impurities that were proposed by Heckl, et. al., indicating that organic impurities are not responsible for the ring structures. They suggested that the protrusions and ring shape structures were

electronic effects of intercalated dopants on the STM images. The protrusions changed into depressions when the imaging bias was switched from positive to negative and the ring shape protrusions also changed from bright to dark. It was proposed that, based on their ionic charges, the vanadium ions were observed as protrusions and fluoride ions as rings. No further explanation was given as to why the ions are imaged differently.

Later studies by Ha *et al.*[6] supported the studies of Permana *et al.* by analyzing the natural MoS_2 sample with glow discharge mass spectrometry (GDMS). STM images of natural MoS_2 revealed protrusions and ring-shaped structures with a diameter between 3 and 8 nm, whereas AFM images of the same MoS_2 surface did not show any structures. They suggested that the ring structures and protrusions are due to titanium and vanadium ions because their concentrations were comparable to the average number density of protrusions and ring structures in the sample. The ring shape structures may appear as an electronic effect caused by two kinds of band bending near the impurities included in the sample.

Interpretations of electronic effects of natural defects in MoS_2

There have been a lot of theoretical and experimental studies on how bias polarity and defects (e.g. atomic vacancy, donor and acceptor substitution of metal and chalcogen,

intercalated impurities) can influence the topographical contrast of impurities in STM images of TMD's. Whangbo *et al.* attempted to classify STM images of point defects through theoretical analysis.[10] In an effort to correlate STM image imperfections and point defects, they performed a theoretical analysis of how point defects modify the energy levels in valence bond and conduction band region of an ideal defect-free MoS_2 layer as well as how they will be imaged. The theoretical results were then used to correlate with STM images of imperfections on MX_2 (M = Mo, W; X = S, Se) surface. An example of a topological height change that depends on the polarity of applied bias polarities is when a donor atom such as a Cl on a S site (Cl_S) in MoS_2 sample creates an electron state below the conduction band [Figure1.2.6]. In this case it is energetically more favorable for this electron to be trapped near the donor cation (Cl^+). At negative sample bias voltages, tunneling occurs predominantly from the E_F of the sample to an empty state of the tip [Figure 1.2.7 (a)]. When the Fermi level of the sample is closer to the donor level than to the valence band top, the donor level will contribute more to the tunneling process, resulting that the area with electron traps appears brighter than the surrounding area in the STM images (protrusions). If the magnitude of applied bias is

(a)

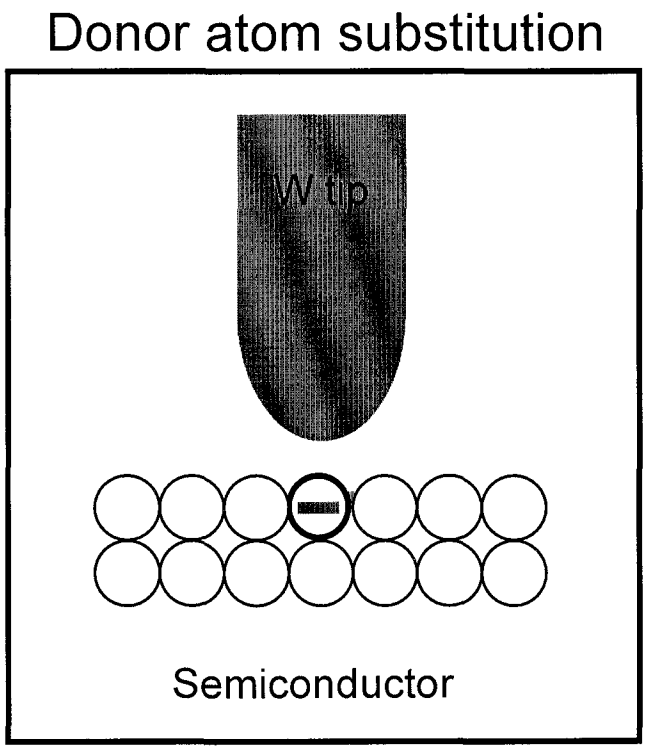

(b)

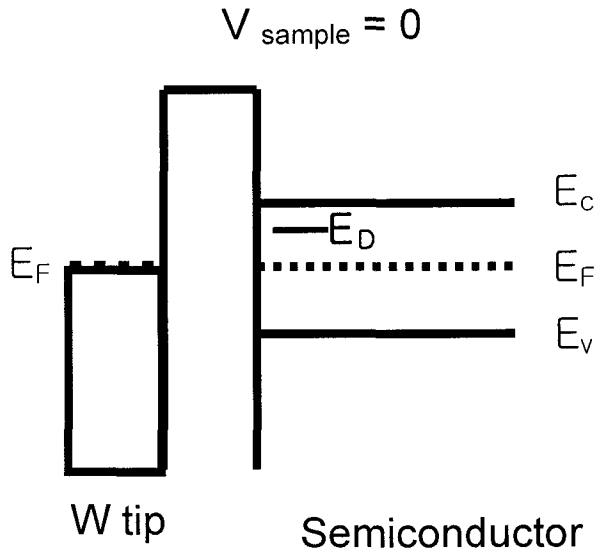

Figure 1.2.6. A donor atom is substituted such as Cl at the S site (Cl_S) in MoS_2 sample. the donor atom substitution creates an electron at the bottom of the conduction band within band gap.

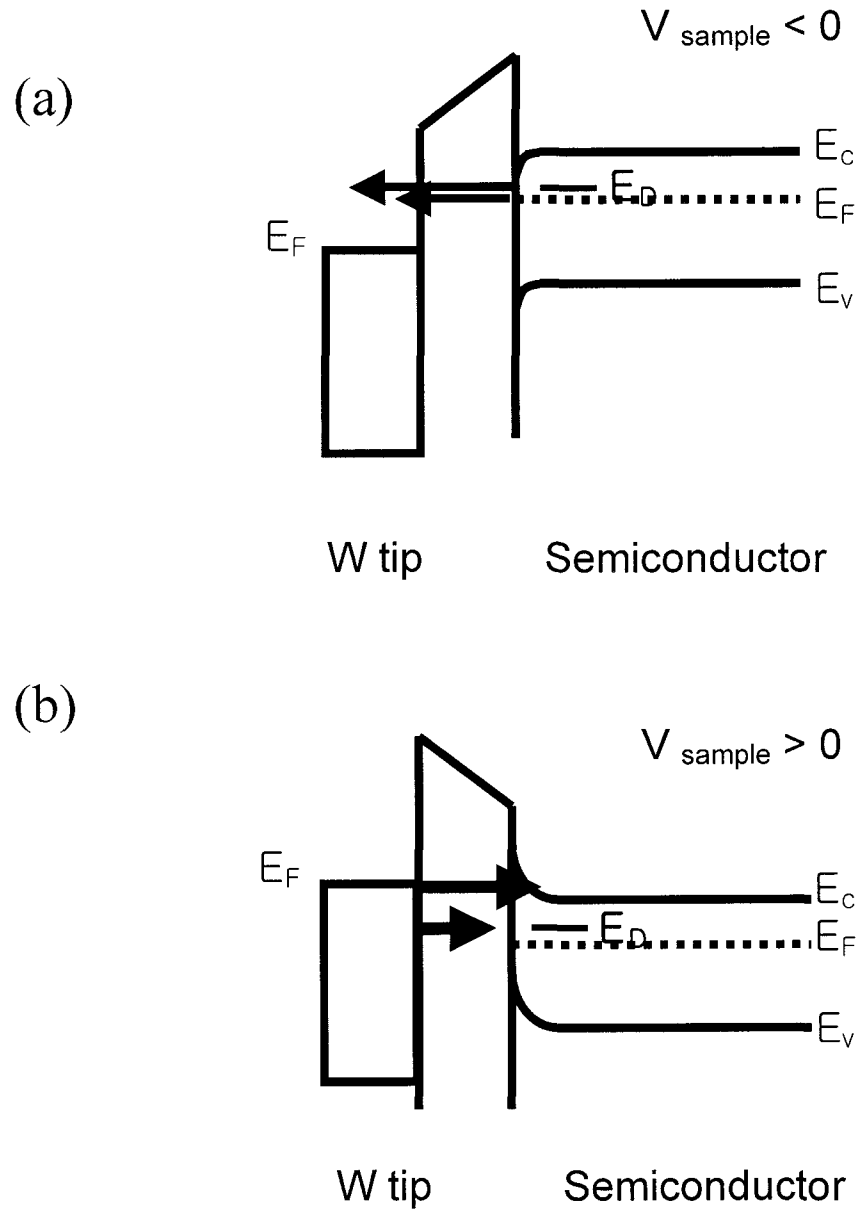

Figure 1.2.7. (a) At the negative sample bias voltage, tunneling occurs predominantly from the E_F of the sample to empty state of the tip. (b) At the positive bias, both donor level and conduction band bottom can receive electrons from the tip. Note that the electron transfer is dominant at conduction band.

large enough for the E_F of the tip to lie below the valance band top, the energy states near the top of valence band dominate the tunneling current. The electrons will predominantly tunnel out of the top of valance band, decreasing the image contrast of the defect. At the positive sample bias voltages, the bottom of donor level and conduction band can receive electrons from the tip [Figure 1.2.7 (b)]. However, the area with electron-traps (donor site, Cl_S) has less tendency to receive electrons from the tip than the surrounding atoms due to its trapped electron. Therefore the area with electron traps will appear darker than its surrounding at positive sample biases

Matthes *et al.*[8] proposed that the topographical contrast near acceptor sites on p-type WSe_2 is induced by two competing current mechanisms involving tunneling into valence band and conduction band states. In STM images of p-type WSe_2, the acceptor sites appear as depressions and protrusion at a positive and negative sample bias, respectively. For positive sample bias, the p-type semiconductor surface gets into accumulation. The tunneling current increases with applied bias and will consist of two components, a minority carrier (electron) injection current into the conduction band of the sample (J_{CB}) and a majority carrier (hole) extraction current from the valence band (J_{VB}). At a small positive sample bias, J_{VB} is dominant due to tunneling of holes from the valence band into the tip, whereas at larger positive sample bias, the additional applied

bias essentially drops in the tunneling gap and J_{CB} dominates the tunneling current due to tunneling of electrons from the tip into unoccupied states in the conduction band. When the tip is located above an acceptor site, the tip (negative potential) has an opposite polarity of the acceptor (positive charge), resulting in both conduction and balance bands being bent further upward due to the additional coulomb potential. Therefore, J_{VB} will increase at an acceptor site while J_{CB} is reduced. At a large positive bias (J_{CB} is a dominant), local reduction of J_{CB} decreases the total tunneling current, causing the tip to move close to the surface in order to maintain constant current. This STM tip movement toward the surface makes the acceptor site appears as a depression.

STM experiments on Si and GaAs have revealed that the apparent height or depth of features associated with dopants is in the range of ± 0.1nm. The appearance of dopants in topological images is normally due to localized band bending or a change of the local density of states around the dopant atoms. STM investigations of TMD's yield similar dopant related features but with ten fold change in the height of protrusions than those observed with Si and GaAs. These height changes cannot be explained solely by electronic effects since a 0.1nm tip sample distance corresponds to a change in the occupied density of states of about one order of magnitude. This implies that the occupied density of TMD's states need to change an impossibly large ten orders of

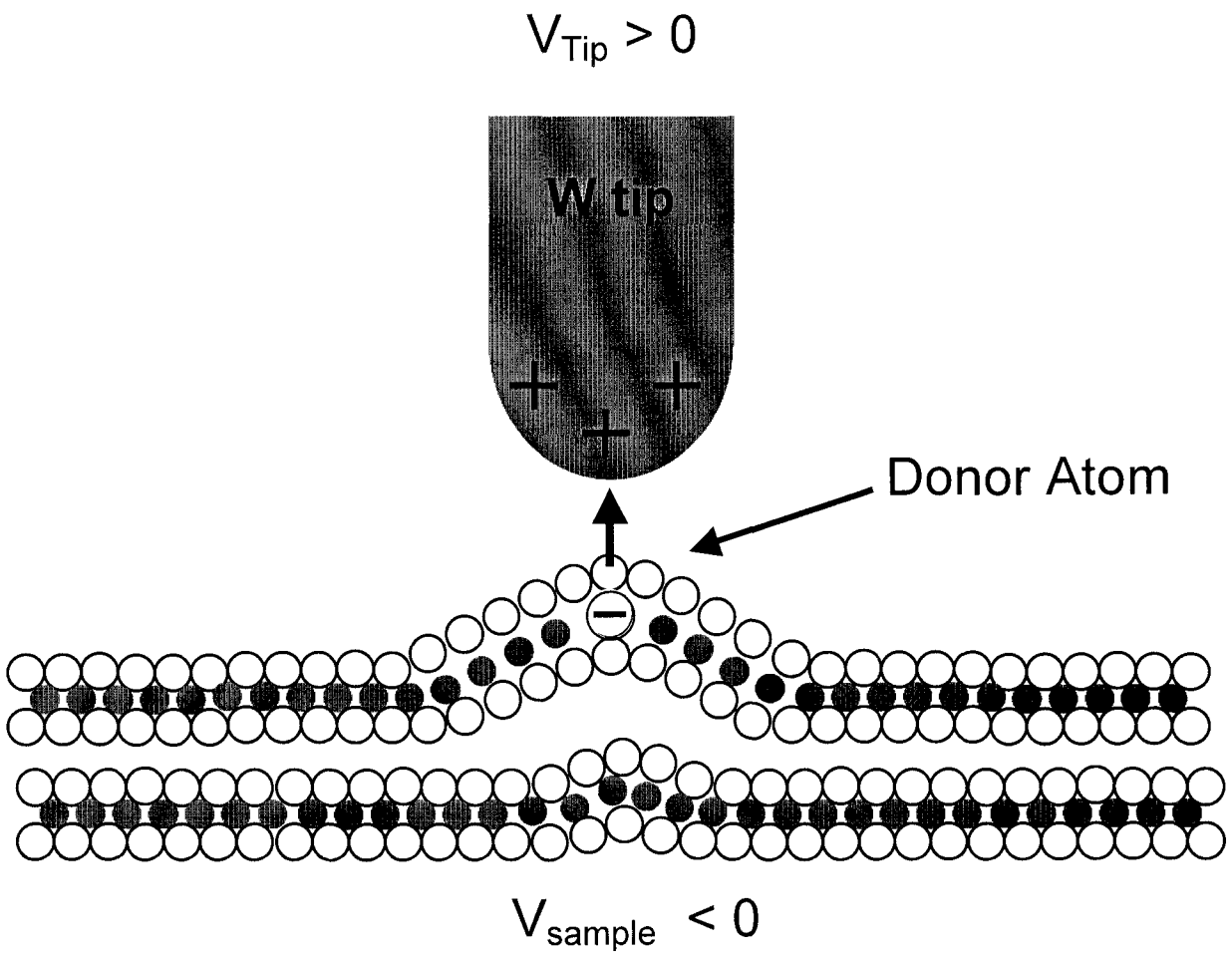

Figure 1.2.8. Diagram indicating the proposed mechanism by which van der Waals layers of a TMD are pull apart when imaging in the vicinity of a dopant atom with a negative sample bias.

magnitude in the area around the dopant.

Previous workers in the Parkinson group interpreted these big height changes in layered materials as the result of induced electrostatic forces between the tip and sample, resulting in a structural deformation of the surface near the dopant atoms.[14,15] In order to investigate the influence of the electrostatic forces, they performed STM measurements on p-type MoS_2 at different bias voltages. The images obtained at -1.5V show protrusion heights of about 1.2nm whereas the same protrusions appear much smaller (about 0.2nm) at -0.07 V. Additional measurements with CITS showed that the changes in the density of states of dopant sites plays only a minor role and cannot explain the large height changes. However, the electrostatic force measurements using a tapping mode AFM, with an applied DC bias voltage between cantilever and sample, showed that the electrostatic forces increase with applied DC bias and thus play an important role in the observed height changes. A sheet charge build up under an accumulation layer, produced at the negative sample biases in n-type materials, causes a high electrostatic force between the top most layer of the sample and the tip apex. This leads to an increase of the measured height since the soft layers are weakly bound to the subsurface layers and are pulled up towards the tip. Figure 1.2.8 shows a schematic how the surface is pulled toward the tip when the tip is in close lateral proximity to a dopant atom. Since the dopant atom in this

example is incorporated into the top van der Waals layer of the MoS_2, the pulling of the dopant toward the tip causes a distortion of the covalent lattice surrounding the ionized dopant. This phenomenon causes the top van der Waals layer in the region around the ionized dopant to be pulled up toward the tip, creating strong contrast changes of dopants in STM images.

REFERENCES

[1] I. Ekvall, *Charge density waves and alkali metal interactions in layered materials* (Goteborg University, Goteborg, 1999).

[2] K. K. Kam and B. A. Parkinson, J. Phys. Chem. **86,** 463 (1982).

[3] S. W. HLa, V. Marinkovic, A. Prodan, and I. Musevic, Surf. Sci. **352,** 105 (1996).

[4] A. Saidi, W. Hasbach, W. Raberg, and K. Wandelt, J. Vac. Sci. Technol. A **16,** 951-955 (1998).

[5] S. N. Magnov, H.-J. Cantow, and M.-H. Whangbo, Surf. Sci. **318,** L1175-L1180 (1994).

[6] J. S. Ha, H. S. Roh, S. J. Park, J. Y. Yi, and E. H. Lee, Surf. Sci. **315,** 62-68 (1994).

[7] H. Permana, S. Lee, and K. Y. Simon Ng, J. Vac. Sci. Technol. B **10,** 2297-2301 (1992).

[8] T. W. Matthes, C. Sommerhalter, A. Rettenberger, P. Bruker, J. Boneberg, M. C. Lux-Stainer, and P. Leiderer, Appl. Phys. A **66,** S1007-S1011 (1998).

[9] C. Sommerhalter, T. W. Matthes, J. Boneberg, M. Lux-Steiner, and P. Leiderer, Appl. Surf. Sci. **144-145,** 564-569 (1999).

[10] M.-H. Whangbo, J. Ren, S. N. Magnov, H. Bengel, B. A. Parkinson, and S. A., Surf. Sci. **326,** 311-326 (1995).

[11] J. G. Kushmerick, S. A. Kandel, P. Han, J. A. Johnson, and P. S. Weiss, J. Phys. Chem. B **104,** 2908-2988 (2000).

[12] M. Weimer, J. Kramer, C. Bai, and J. D. Baldeschwieler, Phys. Rev. B **37,** 4292 (1988).

[13] W. M. Heckl, F. Ohnesorge, G. Binnig, M. Specht, and M. Hashmi, J. Vac. Sci. Technol. B **9,** 1072-1078 (1991).

[14] R. Schlaf, D. Louder, M. W. Nelson, and B. A. Parkinson, J. Vac. Sci. Technol. A **15,** 1466-1472 (1997).

[15] R. Schlaf, P. G. Schroeder, M. W. Nelson, R. Stubner, S. Tiefenbacher, H. Jungblut, and B. A. Parkinson, Thin Solid Films **331,** 203-209 (1998).

1. 3 Hydrodesulfurization

Hydrodesulfurization catalysis

Petroleum plays a predominant role in our lives as a source of chemicals and fuels. Petroleum contains not only a series of hydrocarbons such as paraffins, alkanes, aromatic ring compounds, and naphthenes but also sulfur and nitrogen in the form of a variety of organic compounds.[1] The sulfur containing compounds found in petroleum are generally classified into two types: heterocyclic compounds and non-heterocyclic compounds.[1] Non-heterocyclic compounds are comprised of thiols, sulfides, and disulfides. Heterocyclic compounds are mainly composed of thiophenes with one to several rings and alkyl or aryl substituents. Examples of sulfur compounds are shown in Figure1.3.1.

Hydrodesulfurization (HDS) is the catalytic removal of sulfur from sulfur containing organic compounds in petroleum and coal feedstocks. HDS is very important process for two main reasons. First, the sulfur containing organic compounds deactivate Pt based catalysts used in the reforming oil and in automobile catalytic converters

Noncyclic compounds

RSH RSSR' RSR'

Heterocyclic compounds

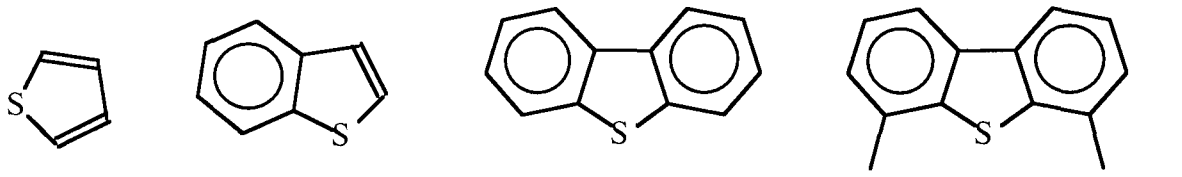

Thiophene Benzothiophene Dibenzothiophene 4,6-Dimethyldibenzo thiophene

Figure 1.3.1. The sulfur containing compounds found in petroleum are generally classified into two types: heterocyclic compounds and non-heterocyclic compounds

Second, HDS improves the quality of gasoline related products by reducing SO_x emissions produced by fuel combustion that creates detrimental effects on our environment. Due to its industrial and environmental importance, many approaches have been taken to understand this catalytic system. The mechanism of HDS on heterogeneous catalysts has been of considerable interest in recent years. However, the exact mechanism still remains unknown.

A generic reaction for the HDS process can be written as follows:

$$RS + nH_2 \xrightarrow{\text{Catalyst}} R'H + H_2S$$

The conventional industrial catalysts frequently contain a mixture of MoS_2 promoted with Ni and Co on alumina supports.[2] The performance of MoS_2 catalysts in the HDS process can be substantially improved by the addition of metal promoters. After comparing the effects of several metals (V, Co, Ni, Zn, Fe, Cr, and Cu) on the HDS activities of MoS_2 catalysts, it was found that Ni and Co were the best promoters.[3] However, the details of the mechanism and the structure of the active sites are still not known.

Active sites for Hydrodesulfurization

It was assumed, as early as the 1970's, that S atoms on the basal plane of MoS_2 are more strongly bonded to the Mo cations than at edges or corners.[1] Therefore, catalysis most likely occurs at the exposed Mo atoms at edges and corners. Experimental verification for this has been provided by surface science studies of the catalytic activity of MoS_2 single crystals. Salmeron *et al.*[4] showed that MoS_2 with a large ratio of basal plane to edge sites has a negligible activity for HDS of thiophene. However, sputtering of the basal planes to expose Mo atoms increased activity, consistent with the assumption that exposed Mo atoms at the edge sites are the active sites for HDS.[1]

The MoS_2 dispersion, that determines the ratio of edge to basal plane sites, plays a predominant role in the activity of HDS catalysts. An interesting study that measured catalytic activity as a function of MoS_2 crystal morphology suggested that the fraction of exposed basal plane affects the catalytic activity.[5] Daage and Chianelli modified the morphology of unsupported MoS_2 catalysts by treating with O_2 and HCl.[5] The experimental results were interpreted in terms of a simple physical model, called the "rim-edge" model, where the catalyst particle can be described as a stack of several layers. The top and bottom layers are called rim sites and the layers sandwiched between top and bottom are called edge sites. Sulfur hydrogenolysis occured on both rim and edge

sites, while the hydrogenation occurs exclusively on the rim sites. One of the interesting results was that the catalytic activity increased when stacking patterns contained a majority of rim sites. These studies indicated that, even though the basal plane is inactive for HDS, it plays an important role in the catalytic reaction.

Structure of Co or Ni Promoted catalysts

Promoters are catalytic additives and can be classified into two categories according to the method by which they promote and facilitate catalytic reactions: structural promoters and electronic promoters. A structural promoter alters the structure of catalyst to create new catalytic sites. An electronic promoter alters the electron density of the catalysts that enhances the catalytic activity (turnover frequency).[6]

In HDS studies, the structure of a catalyst containing promoters such as Co and Ni has been extensively investigated. Topsoe *et al.*[7] proposed that the active sites of Co or Ni promoted MoS_2 catalysts are located on the so-called "Co (Ni)-Mo-S" structure, where Co (Ni) atoms are bonded to the edges of MoS_2 crystals. Later studies by this group suggested that there are different types of Co (Ni)-Mo-S structures and that some of these Co (Ni)-Mo-S structures function as highly active catalytic sites in industrial catalysts. At present, these structures are generally accepted as the active catalytic sites for HDS

processes. However, the origin of the promoting role of Ni or Co and in particular the atomic scale location of the promoter atoms in Co (Ni)-Mo-S structures is still the subject of intense debate.[8]

Numerous studies indicate that the catalytic activity of the Co-Mo-S structures depends on the morphology of the supported MoS_2 cluster because the layered MoS_2 structure is highly anisotropic. It has been suggested that there are at least two types of Co (Ni)-Mo-S structures in the sulfided $CoMo/Al_2O_3$ catalysts: the first model, called Co-Mo-S(I), has a relatively strong interaction with the support and is less catalytically active, whereas the second model, called Co-Mo-S(II), has weak interactions with the support and is more catalytically active.[9,10] Figure 1.3.2 shows expected catalytic performance of Co-Mo-S structures depending on the orientation of the MoS_2 cluster on the support. The upper edge sites of "edge-bonded" MoS_2 clusters perpendicular to the support surface have weaker electronic interactions to the support surface and less steric hindrance, resulting in higher catalytic activity [Figure 1.3.2 (a)]. The single layered MoS_2 clusters that are "basal bonded" has a strong interaction with the support show lower catalytic activity [Figure 1.3.2 (b)]. The upper edge sites of the "edge-bonded" MoS_2 clusters have less steric hindrance and electronic interaction to the support, leading

(a) Edge-bonded MoS_2 cluster

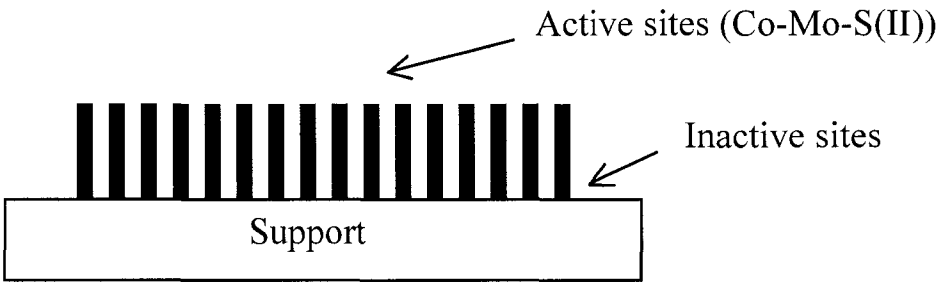

(b) Single-layered MoS_2 cluster basal bonded to the support

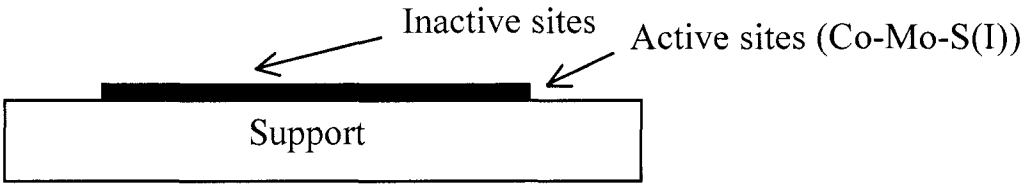

(c) Multi-layered MoS_2 cluster basal bonded to the support

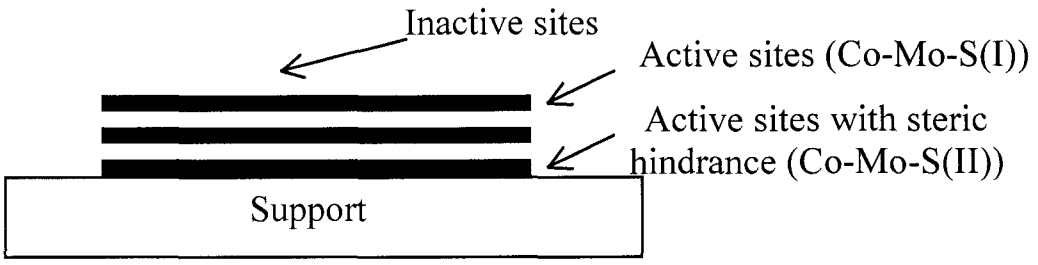

Figure 1.3.2. Schematic of the orientation of MoS_2 clusters on supports.

to higher catalytic activities [Figure 1.3.2 (c)]. Araki *et al.*[11] suggested that single layered MoS_2 cluster with Co at their edges are probably Co-Mo-S(I), whereas multilayered MoS_2 clusters with Co, except on the bottom layer, are Co-Mo-S(II).

Lauristsen *et al.*[12-14] measured atomic scale STM images of single layered Co-Mo-S clusters. Single MoS_2 clusters were initially produced by e-beam evaporating Mo onto a Au(111) surface under an H_2S atmosphere. While maintaining the H_2S pressure, Co and Mo are subsequently co-deposited to cap the initial nano-clusters, resulting in addition of Co atoms to the edge of MoS_2 nano-clusters. It was observed that the presence of the Co atoms causes the shape of the MoS_2 nano-clusters to change from triangular to hexagonal. This change in morphology appears to be induced by a preference for Co to be located at the S edge of MoS_2 (the edge terminated by S atoms, refer to Figure 1.2.1). On the basis of atomically resolved STM images, it is believed that the presence of Co atoms has a dramatic influence on the morphology of the MoS_2 structures and the Co atoms were present in only one type of MoS_2 edges, the so-called S edges. Besides morphological and structural information, the STM studies showed that there were changes in the local electronic environments of sulfur atoms neighboring the Co edge atoms.[13,15]

Weiss and co-workers proposed an additional role for Ni or Co promoters on the basis of their observation that Ni atoms are mobile on the MoS_2 basal plane even at

77K.[16-18] Spectroscopic measurement by STM showed that Ni adatoms create favorable electronic effects for binding nucleophilic reactants.[16,17] These Ni adatoms increase the sticking probability of sulfur containing compounds by binding them on the basal plane of MoS_2 and transporting these bound molecules to the active sites for reaction. For example, thiophene molecules impinging on the unreactive basal plane of the MoS_2 do not bind to S atoms on the basal plane. However, mobile Ni adatoms adsorbed to the basal plane are well suited to complex with the thiophene molecules, thus increasing the effective sticking coefficient of thiophene. These Ni-promoted complexes can diffuse around the surface until reaching an active step edge sites where the HDS can occur. Therefore, the transfer agent increases the reactant concentration at the active sites, increasing the catalytic activity.

Thiophenes on HDS catalysts

Thiophene and its derivatives form transition metal complexes by coordinating with Mo atoms through either their *p* electrons or S atom's lone pair of electrons.[19] The η^1(S) and η^2 binding types require only one-open coordination site where the superscript indicates the number of thiophene atoms bound to the metal. The thiophene in both of these binding modes is a formal two-electron donor to the metal. The η^4 thiophene will

require at least two sulfur vacancies and is a four-electron donor. The η^5 adsorption mode is most likely on a cluster of three sulfur vacancy sites and, in this form, the thiophene is a six-electron donor. Zonnevylle and coworker examined the coordination of thiophene to Mo atoms at the edge sites of MoS_2 using Huckel tight binding theory. Most of their calculations assumed a two-sulfur vacancy site. In this model, the η^1(S) thiophene binds more strongly than η^5 thiophene and the η^5 coordination weakens thiophene C-S bonds more efficiently. This C-S bond weakening is even greater if additional sulfur atoms are removed from the Mo coordination sphere. Moreover, η^5 thiophene binds more strongly to these lower coordinated Mo atoms. The greater weakening of the C-S bond in the η^5 form as compared with that in η^1(S) thiophene is consistent with the observed higher reactivity of η^5 thiophene in organometallic compexes, which suggest that η^5 coordination on a catalyst surface is the most activating mode of adsorption. However, no prior experimental result for the thiophene adsorption on MoS_2 has been announced.

REFERENCES

[1] T. Kabe, A. Ishihara, and W. Quian, *Hydrodesulfurization and Hydrodenitrogenation* (Kodansha, Tokyo, 1999).

[2] P. T. Vasudevan and J. L. G. Fierro, Catal. Rev. -Sci. Eng. **38,** 161 (1996).

[3] R. Prins, V. H. J. D. Beer, and Somorjai, Catal. Rev. -Sci. Eng. **331,** 1-41 (1989).

[4] M. Salmeron, G. A. Somorjai, A. Wold, R. R. Chianelli, and K. S. Liang, Chem, Phys. Lett. **90,** 105-107 (1982).

[5] M. Daage and R. R. Chianelli, J. Catal. **149,** 414-417 (1994).

[6] R. M. Heck, R. J. Farrauto, and S. T. Gulati, *Catalytic Air Pollution Control*, 2nd ed ed. (Wiley-Interscience, new york, 2002).

[7] H. Topsoe, B. S. Clausen, R. Candia, C. Wivel, and S. Morup, J. Catal. **68,** 433 (1981).

[8] H. Topsoe, B. S. Clausen, and F. E. Massoth, *Hydrotreating Catalysis*, Vol. 11 (Springer-Verlag, Berlin/Heidelberg, 1996).

[9] R. Candia, O. Sorensen, N. Topsoe, B. S. Clausen, and H. Topsoe, Bull. Soc. Chim. Belg. **93,** 763 (1984).

[10] D. D. Whitehurst, T. Isoda, and I. Mochida, Adv. Catal. **149,** 345 (1998).

[11] Y. Araki, K. Honna, and H. Shimada, J. Catal. **207,** 361-370 (2002).

[12] J. V. Lauritsen, S. Helveg, I. Lagsgaard, B. S. Clausen, H. Topsoe, and F. Besenbacher, J. Catal. **197,** 1 (2001).

[13] M. V. Bollinger, J. V. Lauritsen, K. W. Jacobsen, J. K. Norskov, S. Helveg, and F. Besenbacher, Phys. Rev. Lett. **87,** 196803 (2001).

[14] S. Helveg, J. V. Lauritsen, I. Lagsgaard, J. K. Stensgaard, J. K. Norskov, B. S. Clausen, H. Topsoe, and F. Besenbacher, Phys. Rev. Lett. **84,** 951 (2000).

[15] H. Schweizer, P. Raybaud, G. Kresse, and H. Toulhoat, J. Catal. **207,** 76 (2002).

[16] J. G. Kushmerick, S. A. Kandel, P. Han, J. A. Johnson, and P. S. Weiss, J. Phys. Chem. B **104,** 2908-2988 (2000).

[17] J. G. Kushmerick and P. S. Weiss, J. Phys. Chem. B **102,** 10094 (1998).

[18] S. A. Kandel and P. S. Weiss, J. phys. Chem. B **105,** 8102 (2001).

[19] R. J. Angelici, Bull. Soc. Chim. Belg. **104,** 265 (1995).

Chapter 2

Fabrication and Investigation of Nanostructures on MoS_2 and $MoTe_2$ Surfaces using a Scanning Tunneling Microscope (STM)

2. 1 Introduction

The scanning tunneling microscope (STM) is a powerful tool that is suitable for surface nano-fabrication from the nanometer scale dawn to the atomic scale. The STM has been used to manipulate individual atoms and molecules with atomic level precision as well as to generate the artificial structures such as pits, mounds, grooves, and single atomic vacancies.[1-14] Potential applications of this technology include nano-scale etching, high-density recording, and ultra fine lithography. Some specific examples of the use of STM in nanofabrication will be reviewed below.

Eigler *et al.* demonstrated single atomic manipulation with an STM tip by relocating individual xenon atoms and generating an atomic pattern on a Ni(110) surface at low temperatures (4K).[1] An STM tip could produce grooves on a Si (111) surface at a few nanometer scale by applying voltages above a critical value. The fabrication of grooves was explained by field emission of positive and negative silicon ions.[2,3] Nanometer scale pits and mounds on Au surfaces were fabricated by applying voltage pulses between a Pt-Ir tip and sample.[4] Positive and negative voltage pulses generated pits and mounds, respectively, where the produced mounds could then be removed by applying positive biases. York *et al.* showed that STM voltage pulses generated nanometer scale pits and islands simultaneously on Ag films grown on Cu (100) surface. It was proposed that ejected atoms from the pits diffused to the Ag step edges instead of being evaporated into vacuum.[14] Wada *et al.* fabricated "nano-needles" on a Si(111) surface with a diameter of 2nm and a maximum height of 20nm by ramping the tip voltage in the negative direction.[5,6] It was proposed that high applied voltages extracted silicon atoms from the surface that migrated to the tip apex and were re-deposited on the sample surface. In addition to the forementioned studies, other studies generated nanostructures using various tip materials (Pd[7], Pt[8], Al[9], and Au[10]) on substrates including graphite[8,11], Pd[7], SiO_2[12], polymers[13] and Ag[14]. In this work, we present nanostructure (pit)

fabrication on MoS_2 and $MoTe_2$ surfaces by applying voltage pulses between the tip and sample surface.

Various types of nanostructures were also fabricated on transition metal dichalcogenide (TMD's) surfaces such as MoS_2,[15-17] WSe_2,[18-20] and $SnSe_2$[15]. Schimmel *et al.* showed that the application of positive voltage pulses (3.2 V) to the WSe_2 surface produced small hill-shaped structures with a diameter of about 3 nm.[18] The features were attributed to a change in the local density of states since the atomic order was preserved in the nanostructures and their apparent heights changed at different imaging biases. In another experiment, voltage ramping between 1.0 V and –1.0 V removed several Se atoms from the WSe_2 surface, producing pits with a diameter of about 0.6 nm.[19] In later studies, Huang *et al.*[15] and Hosoki *et al.*[16] claimed that application of a positive voltage pulse to an STM tip in UHV generated single sulfur atomic vacancies on MoS_2. It was suggested that there is a voltage threshold for surface modification (3.6 ± 0.3 V).[15]

Even though nanostructure fabrication has been somewhat extensively investigated, the exact physical process responsible for the surface modification still remains unknown in many cases. Several mechanisms such as electric field evaporation, local sublimation by tunneling electrons, local heating, and mechanical contact have been proposed to explain this phenomenon. The various mechanisms will be discussed below

in order to clarify the possible physical processes occurring during our experiments using voltage pulses on MoS_2 and $MoTe_2$ surfaces.

Electric field evaporation

The electric field evaporation mechanism originates from a basic physical process exploited in field ion microscopy (FIM) where a strong electric field applied to the tip of a sharp metallic needle ionizes He or Ne atoms and accelerates them to a phosphor screen, resulting in an image representing individual atoms on the tip.[21] In the STM, a strong electric field is developed between the tip and sample when high biases are applied. A high field can ionize and/or evaporate atoms from the surface of metals and semi-conducting substrates. The field strength can be controlled by variation of the voltage pulse height or the tip-sample separation. Various field strengths can generate different types of nanostructures. e. g. mounds and holes were generated on a Si(111) surface by adjusting the applied electric fields between the tip and sample.[22] Tsong attempted to explain many of these experimental observations through a theoretical analysis based on a FIM model.[23] Although the electric field evaporation mechanism has explained many observations of nanostructuring with a considerable, it has failed to explain several experimental results. For an example, threshold electric fields proposed

for surface modification do not correspond to experimental results. The electric fields for field evaporation of carbon ($C \rightarrow C^{2+}$) and tungsten ($W \rightarrow W^{3+}$) require 85.4 V/nm and 33.7 V/nm, respectively.[23] The experimental results showed that application of voltage pulses of 10 V/nm between a W tip and graphite could modify a graphite surface.[24]

Local sublimation by tunneling electrons

Kondo *et al.* observed a linear relationship between the threshold voltages (V_t) for nanostructure fabrication and the binding energies of the materials and proposed that direct electron bombardments cause chemical bonds of surface atoms to be broken, resulting in sublimation of the atoms or atomic clusters.[25] Hence, sublimation occurs only from the surface at positive sample biases, provided that the applied bias is above a threshold level, whereas negative sample biases induce sublimation of the tip materials. Even though this mechanism is in good agreement with many experimental observations, it cannot explain several other experimental observations: transfer of silicon clusters between a tip and sample at positive going sample voltage pulse[22], deposition of gold particles from a gold tip by applying a positive going voltage pulse to the surface[26], and mound formation on WSe_2 using positive sample biases[18].

Mechanical contacts and local heating

Mechanical contact induced nanostrucuture fabrication has been reported on Si and Au surfaces.[3,27] Oyabu *et al.* showed that mechanical contact itself is enough to manipulate individual Si atoms on the Si (111)-(7 × 7) surface.[27] For single atom manipulations, an atomic force microscope (AFM) operated at low-temperature was utilized, demonstrating that the manipulation processes was purely mechanical since there was no applied bias. Gu *et al.* suggested that, when a small sample bias is applied ($V_{bias} < 0.5$ V), tip sample interactions dominate, whereas at $V_{bias} > 0.8$ V electric field evaporation plays a key role.[3] However, simple mechanical contact cannot explain all of the nanostructuring phenomena. For example, graphite due to its elasticity is not modified by mechanical contact without an applied bias.[28] Koning *et al.* demonstrated that mounds can be generated on Si (111) surface by deposition of gold from a gold tip without mechanical contact since the gold tip was intentionally retracted from the surface during the pulse application.[29] These results indicate that even if mechanical contact plays an important role in nanostructure fabrication, it is not always the dominant process.

The applied tunneling current and voltage from the tip can cause local heating of the surface, producing nanostructures due to rearrangements of the surface atoms through migration and diffusion.[30] However, there appears to be no correlation between threshold

voltages for nanostructure formation and the melting or boiling points of the materials as might be expected, although local heating may be complicated by the phonon coupling and thermal conductivity effects.

2. 2 Experimental Methods

Natural MoS_2 and synthetic $MoTe_2$ [chemical vapor transport (I_2)] crystals were utilized for studying nanostructure fabrication. All experiments were performed in a commercial Omicron Multi-Probe ultrahigh vacuum (UHV) system, with a base pressure of 5×10^{-11} mbar, equipped with a variable temperature scanning tunneling microscope (VT-STM). STM measurements were performed with electrochemically etched tungsten tips. Nanostructures were fabricated by interrupting the raster scanning of the STM tip, while obtaining topological images, and then moving the tip to a new position on the sample where a voltage pulse was applied. The tip and sample distance (gap) was reduced while the current feedback loop was turned off before a voltage pulse was applied between the tip and sample. Subsequently, the tip was rapidly returned to the imaging position and the feedback loop was reactivated. After this operation the sample surface was imaged with the same tip. The amplitude of the voltage pulses ranged from –

10 V to 10 V and the pulse duration ranged from 10 μsec to 70 msec. The tip sample distance (V_{sample}: 0.5 V and I: 1 nA) was estimated as ~ 0.6 nm from Z spectroscopic measurements. At this condition, the feedback loop was stabilized at a tunneling resistance of 5×10^9 Ω setting the relative tip sample separation. The tip was then moved 0.5 nm toward the surface before applying the voltage pulses. All of the images shown here were taken at room temperature in the constant current mode with a tunneling current of 1 nA at sample biases ranging from -2.0 V to +2.0 V. After image acquisition a background plane fit was applied to all of the images.

Tips were prepared from W wire (Goodfellow, 0.38 nm diameter) with a standard DC drop off technique (see introduction section for details). This technique generates tips with apex radii ranging from 70 to 300 nm depending on the cutoff time. For the fabrication of sharper tips, we used a specially built power supply. At the end of the etching process, the potential between the anode (W wire) and cathode (Pt loop) is suddenly switched off within 500nsec as the lower part of the W wire drops off. The rapid switching of the voltage results in very sharp tips with apex radii less than 30 nm. A JEOL 2000 transmission electron microscope (TEM) and JEOL 5600 scanning electron microscope (SEM) were utilized for the characterization of the tips before and after STM experiments.

2. 3 Results and discussions

Before nanostructure formation, the sample was imaged with the STM to make sure that neither natural defects nor surface deformations were present on the region of the surface to be used for nanostructure fabrication. Natural defects in p-type $MoTe_2$ and n-type MoS_2 samples are imaged as protrusions and depressions at positive sample biases, respectively, whereas the contrast was reversed at negative sample biases. Since STM images of natural defects can make it difficult to distinguish nanostructures (pits) produced by voltage pulses, we used positive sample biases (0.1 V ~ 1.5 V) for $MoTe_2$ and negative sample biases (-0.1 V ~ -1.0 V) for MoS_2 throughout the experiments where the natural defects are imaged as protrusions.

Fabrication of nanostructures

Application of positive voltage pulses (3 V ~ 10 V) produced various types of surface nanostructures on $MoTe_2$ and MoS_2 surfaces including mounds, holes, mounds surrounding holes, and mounds inside holes. Figure 2.1 shows STM images of examples of these nanostructures on a $MoTe_2$ surface. The probability of fabricating only a hole

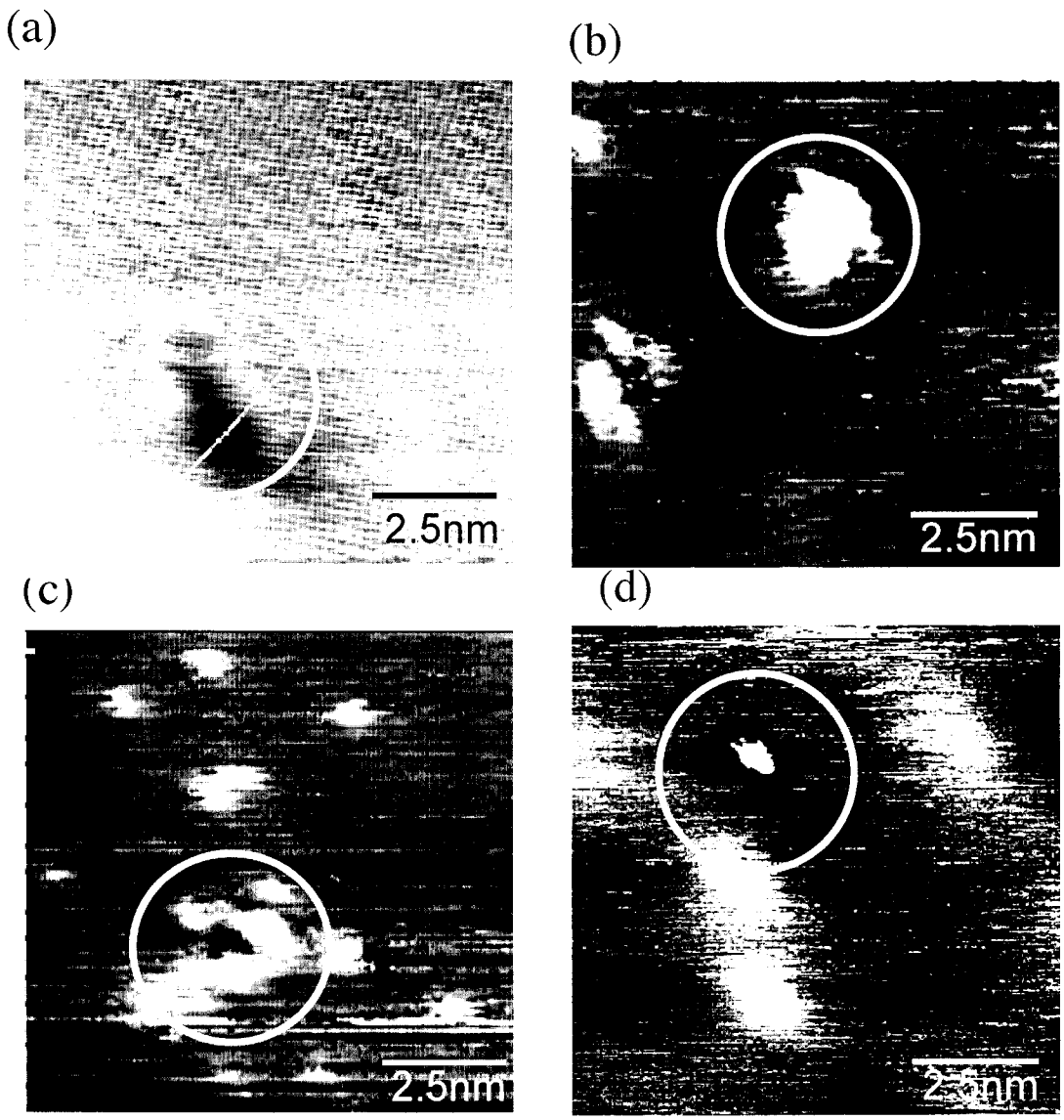

Figure 2.1. 20 x 20 nm^2 STM images of various types of nanostructures. (a) a mound (b) a hole (c) a mound surrounding a hole and (d) a mound inside the hole. All of the STM images were obtained at positive sample bias (V_{sample}= 0.5 V and I= 1.0 nA).

was less than 10% [Figure 2.1 (a)]. In most cases, mounds were randomly distributed around the hole [Figure 2.1 (b) ~ (d)]. The average depth of the fabricated holes was determined to be about 0.25 nm, close to the diameter of Te atom (0.27 nm), but less than the c unit cell value of $MoTe_2$ (0.64 nm). The holes thus could be associated with Te atomic vacancies. On the other hand, the average height of the mound-shaped features was about 0.3 nm regardless of the applied voltage pulse heights. The height and contrast of mound-shaped features were independent of the imaging biases, indicating that the mound shaped-features are not due to the electronic effects on the tunneling image in the vicinity of the holes, but rather can be attributed to deposited material either tellurium atoms or atomic clusters removed from the $MoTe_2$ surface as a result of the voltage pulses.The voltage pulses applied to $MoTe_2$ could remove Te atoms from the surface, producing chemically reactive dangling bonds of Mo and Te atoms inside the holes. If the Te atoms and their atomic clusters are not evaporated into the vacuum, they most likely react with these dangling bonds since the intact basal plane is inert due to the complete coordination of Te atoms. The arrangements of the clusters around the holes will depend on the interactions between the dangling bonds and atomic clusters, and those are imaged by STM as randomly distributed protrusions around hole [Figure 2. 1 (b) ~ (d)]. This

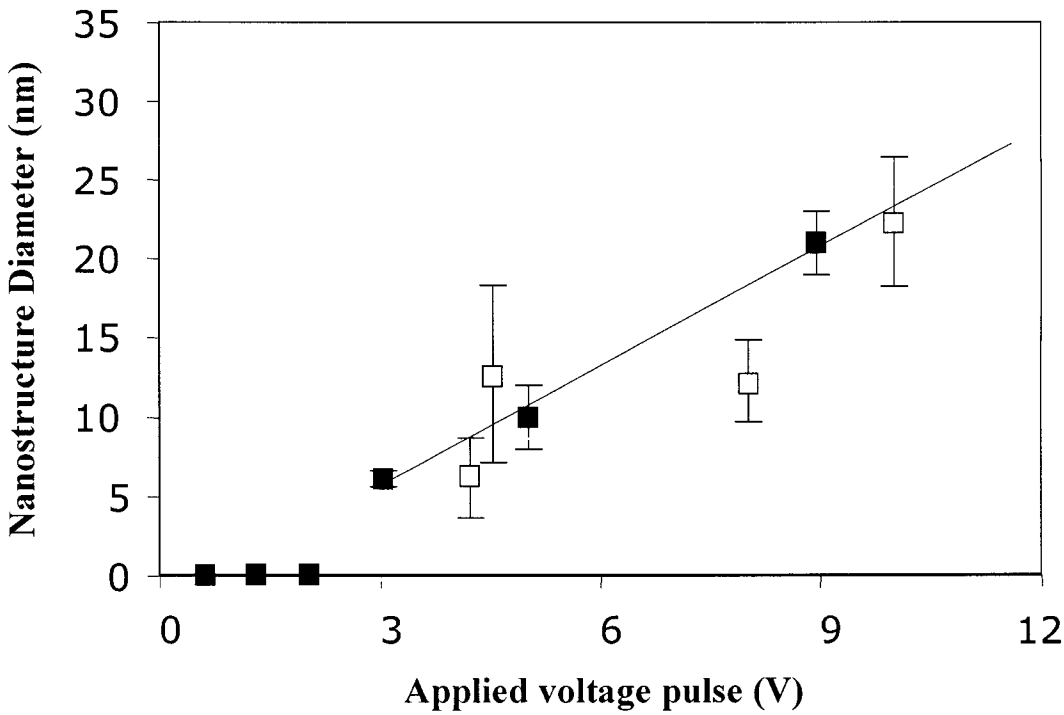

Figure 2.2. The schematic indicates nanostructure diameters (nm) produced on $MoTe_2$ as a function of applied voltage pulses with two different STM tips. Applied voltage pulses for the nanostructure fabrication were between 3V and 10V (pulse duration: 10 msec). Upper and lower bars indicate standard deviation of nanostructure diameters at given voltage pulse conditions.

explanation is similar to that given by York *et al.* where STM voltage pulses produced both pits and adatoms on Ag films grown on Cu (100) surface.[14]

We investigated the influence of the voltage pulse heights on the size of the nanostructures. Figure 2. 2 shows the diameter of the produced nanostructures as a function of the magnitude of the applied voltage pulses using two different W tips. The error bars indicate the standard deviations in the measured diameters of nanostructures. A linear relationship was obtained between nanostructure diameters and the magnitude of voltage pulses. A distinct threshold for nanostructure fabrications on $MoTe_2$ of 3.0 ± 0.3 V was observed, quite comparable to that of other TMD's (MoS_2: ~ 3.8 V[15,25], $SnSe_2$: ~1.5 V[15] and WSe_2: ~ 2 V[31]). On the other hand, it was found that the duration of the pulse (10 μsec to 70 msec) did not affect on the diameter of the produced nanostructures.

One of goals of this work is to fabricate atomic scale nanostructures to investigate the catalytic reactivity of the surface vacancies for hydrodesulfurization (HDS) activity. Therefore, we attempted to generate the smaller Te atomic vacancies using the voltage pulses near the threshold (3 V). The average diameter of holes generated by a 3V voltage pulse varied from 1nm to 20nm depending on the tip. Some tips did not produce any nanostructures even with the maximum voltage pulse height (10V) although they were capable of atomic resolution STM images. Even though single tellurium atom detachment

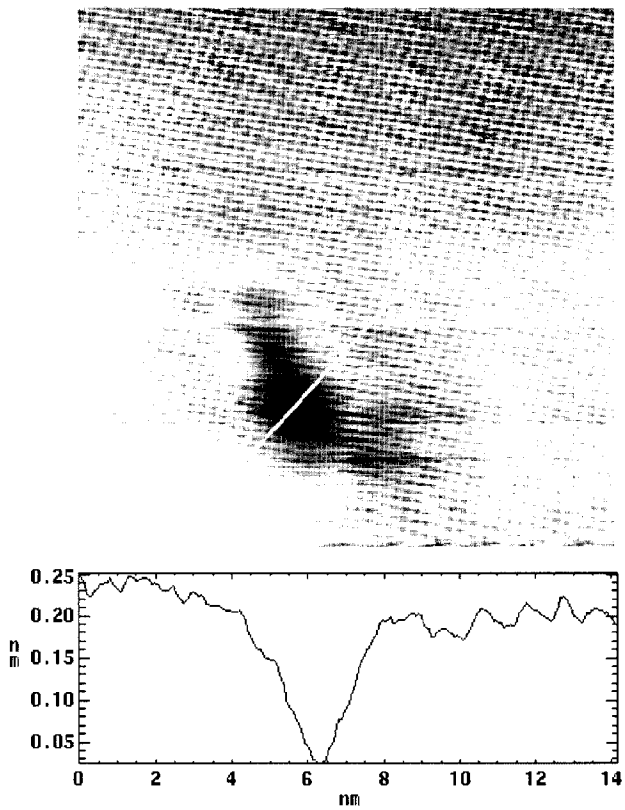

Figure 2.3. 20 x 20 nm^2 STM image of a hole fabricated on $MoTe_2$. The pulse conditions were V_{sample}: 3V and pulse duration: 0.1msec. The hole diameter is about 1.48nm and the depth is about 0.25 nm.

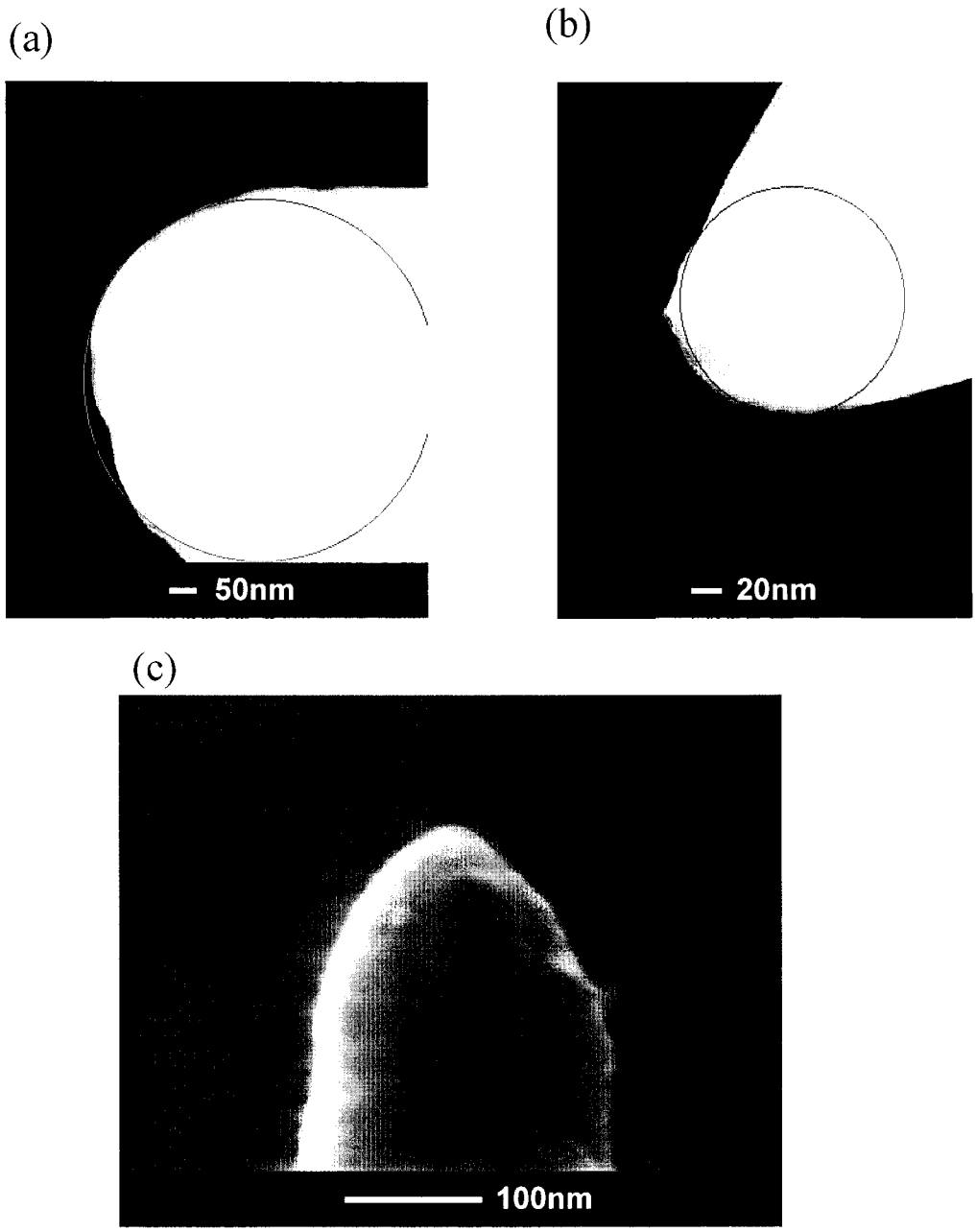

Figure 2.4 (a) and (b) Transmission electron microscope (TEM) images of STM tips. (c) Scanning electron microscope (SEM) image of a STM tip. The tip apex radii of the tips were determined to be (a) 340 nm (b)72 nm and (c) 25 nm.

was not observed by applying near threshold voltage pulses (pulse duration: 1.0 msec), a hole with a diameter of ~ 1.48 nm and depth of ~ 0.25 nm was fabricated as shown in Figure 2. 3. The area of the hole (about 1.7 nm^2) indicates that about 15 - 19 Te atoms were removed from the surface.

STM tip effects on nanostructure fabrication

In order to further investigate effects of tip morphology such as tip sharpness and shape on nanostructure fabrication, we imaged STM tips utilizing TEM and SEM after nanostructure fabrication. Figure 2. 4 shows TEM and SEM images of representative STM tips. It was found that a blunt or flat tip did not produce any nanostructures on the surface although it was capable of producing atomic resolution surface images. Figure 2. 4 (a) shows an example of blunt tip of an apex radius of 340 nm. A tip with a high apex radius or flat geometry has its electric field spread over a large area, making it difficult for Te atoms to be removed. When the tip apex radius is less than 150 nm, the tip begins to produce surface nanostructures. Figure 2. 4 (b) and (c) show TEM and SEM images of STM tips where the tip apex radii were determined to be 72nm and 25nm, respectively. Both tips reproducibly generated nanostructures and surface images.

Figure 2.5 shows the diameter of created holes as a function of tip apex radius at voltages near the threshold voltage pulse condition (3 V). For each tip apex radius more than 30 nanostructures were measured in order to obtain good statistics for nanostructure diameter. The error bars indicate the standard deviations of the measured diameters of the holes and the tip apex radii, respectively. The sharper tips with apex radius less than 30 nm were prepared by using the special power supply (automatic shut-off circuit) whereas the tips with apex radius ranging from 70 nm to 150 nm were prepared without using the circuit. A linear relationship was obtained between the tip apex radii and nanostructure diameters, suggesting that the size of holes strongly reflects the tip apex geometry. The extrapolation leads us to believe that a tip apex radius of less than 10 nm may be able to create single tellurium atom vacancies. Another interesting tip property, in addition to the tip apex radius, is the tip aspect ratio (tip height / tip diameter). A tip with higher aspect ratio produced neither atomic scale surface image nor nanostructure regardless of its sharpness. We speculate that it is due to tip vibration during imaging and voltage pulses. Therefore, the tip sharpness and shape are critical factors in the fabrication of atomic scale nanostructures using voltage pulses.

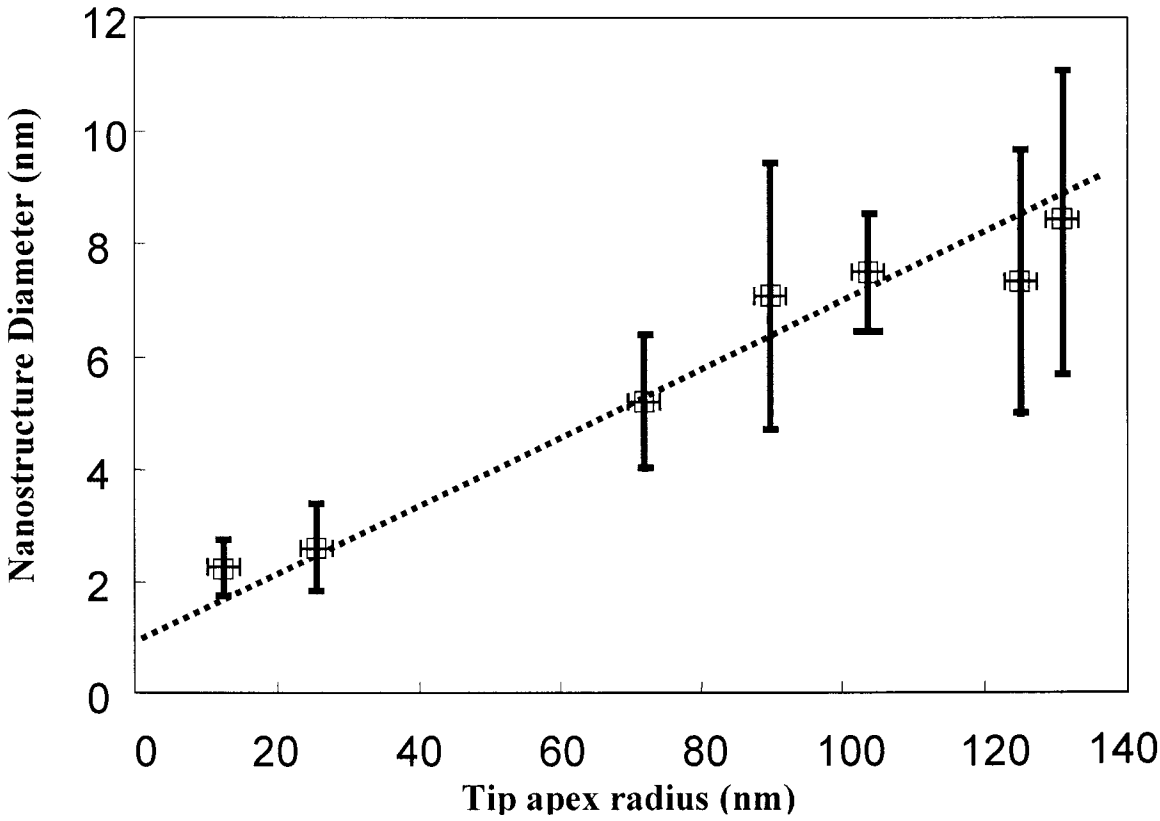

Figure 2.5. Schematic of nanostructure diameters (nm) produced on $MoTe_2$ as a function of tip apex radii. The pulse conditions were V_{sample}: 3V and pulse duration: 10msec.

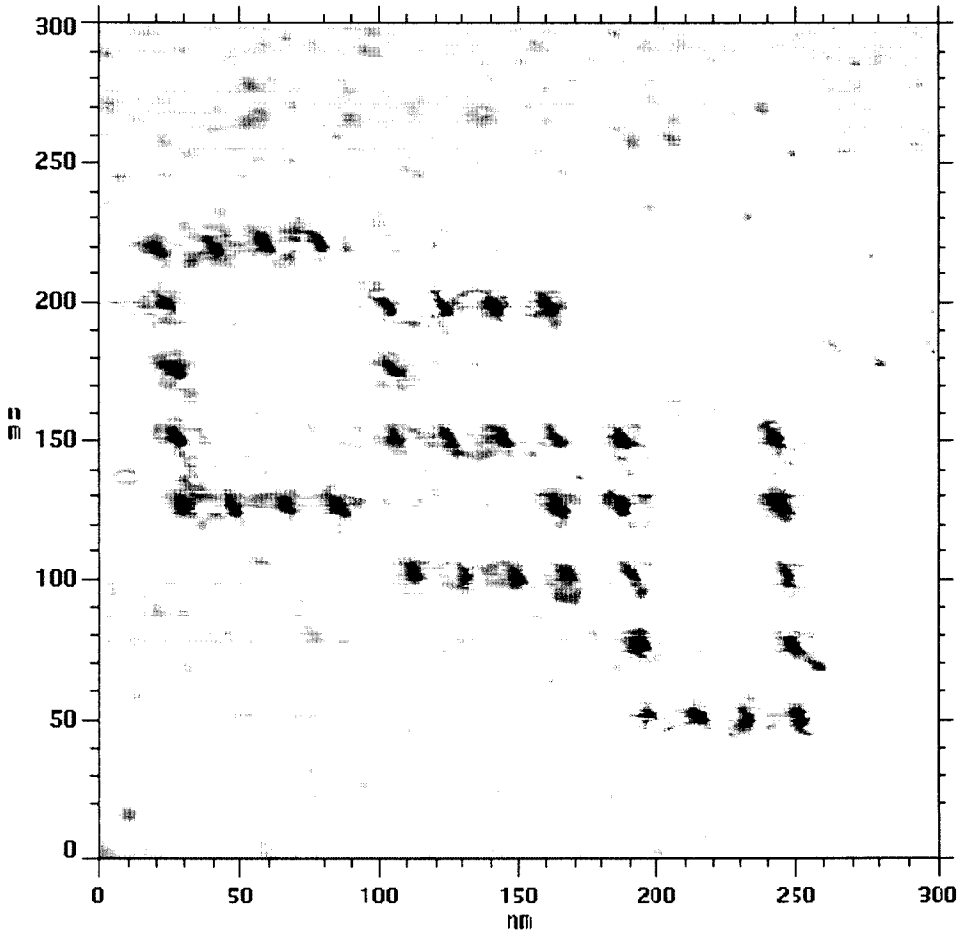

Figure 2.6. 300 x 300 STM image of CSU pattern. This pattern was fabricated on $MoTe_2$. The pulse conditions were V_{sample}: 3V and pulse duration: 10msec.

Figure 2. 6 shows a "CSU" written on $MoTe_2$ in letters only 50 × 100 nm in size made by voltage pulses near the threshold value (3 V, and 10 msec). The average diameter of the holes that make up the letters was determined to be 5.1 ± 0.2 nm, demonstrating that the production of nanostructures is highly reproducible. This pattern illustrates the potential for the ultra high density recording on $MoTe_2$ surface. We attempted to fabricate similar nanostructures on a MoS_2 surface using voltage pulse. The threshold voltage for surface modification of MoS_2 was determined to be 3.4 ± 0.3 V, close to the reported value of 3.6 ± 0.3 V and ~3.8 V reported by Huang *et al.*[15] and Kondo *et al.*.[25] Figure 2. 7 shows a nanostructure on MoS_2 surface produced by applying voltage pulses near the threshold value (3.5 V). A minimum and maximum diameters of the holes was determined to 2.6 nm and 3.2 nm, respectively. Cross sectional analysis shows that the maximum depth of the hole is about 0.25 nm, implying that only sulfur atoms were removed from the surface (sulfur atom diameter: 0.32 nm). The area of the hole (about 6.6 nm^2) indicates that about 80 sulfur atoms were removed from the surface.

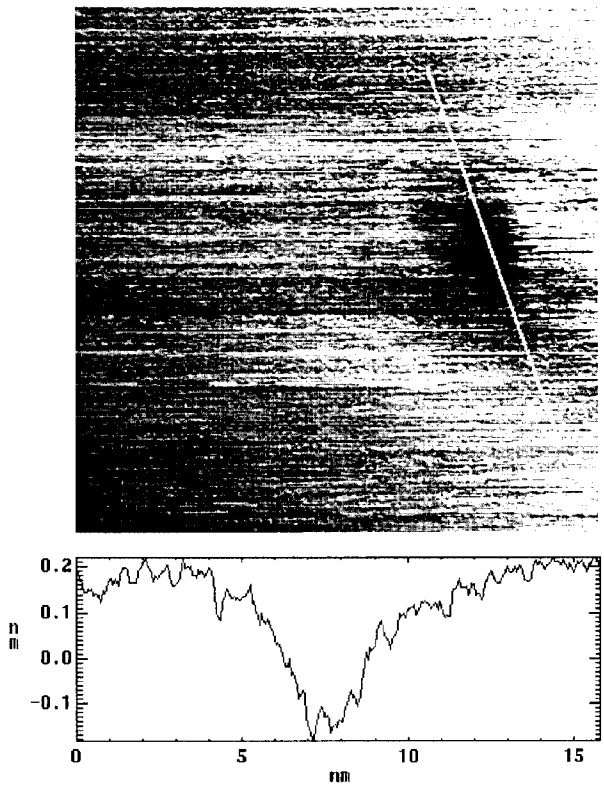

Figure 2.7. 20 x 20 nm^2 STM image of a hole fabricated on MoS_2. The pulse conditions were V_{sample}: 4V and pulse duration: 10msec. The hole diameter is about 2.6/3.2nm (Min/Max).

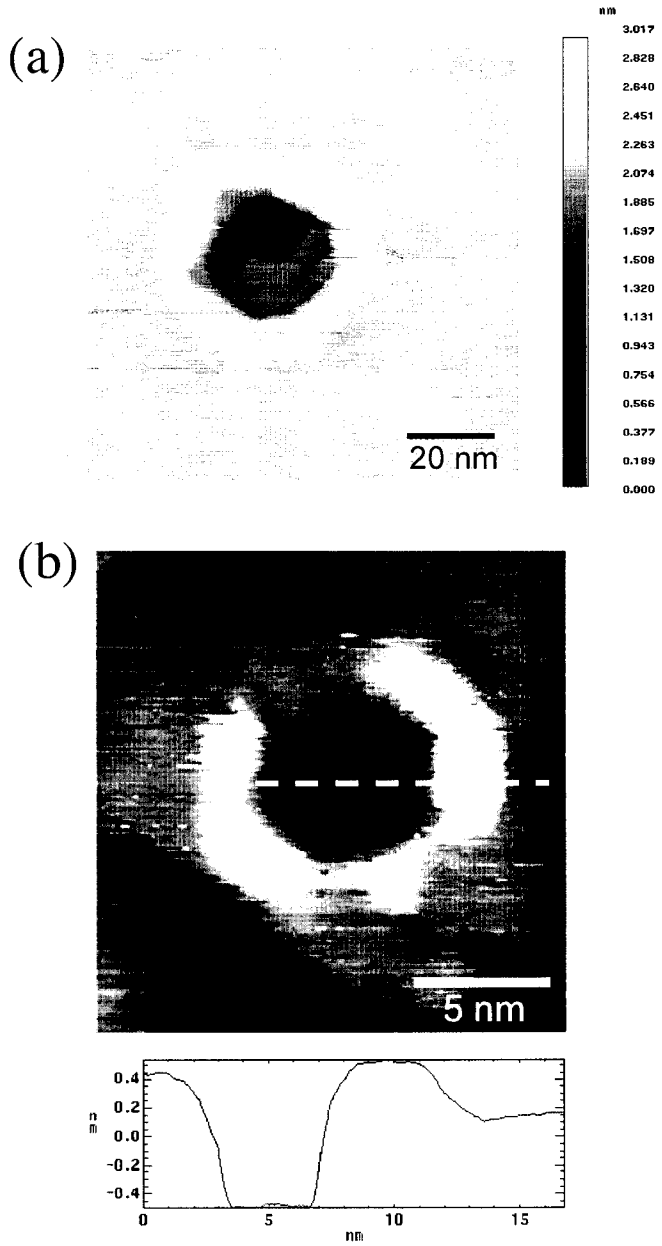

Figure 2. 8 (a) 100 x 100 nm^2 STM image of a hole fabricated by negative voltage pulse to the $MoTe_2$ sample. The pulse conditions were V_{sample} = - 5 V and t = 10 msec. (b) 20 x 20 nm^2 STM image of a hexagonal shape hole fabricated by negative voltage pulse to the $MoTe_2$ sample. The pulse conditions were V_{sample} = - 3 V and t = 10 msec.

Pulse polarity dependence of nanostructure fabrication

We also studied the application of negative voltage pulses to $MoTe_2$ to investigate if pulse polarity affected the production of nanostructures. It was observed that negative voltage pulses produced much larger nanostructures (holes) on $MoTe_2$ when compared with positive voltage pulses. Figure 2. 8 (a) shows a nanostructure produced by applying a negative voltage pulse of –5 V (pulse duration: 10 msec). The measured diameter of the hole (15 ~ 20 nm) is about eight times greater than the average diameter of holes (2.4 ± 0.5 nm) produced by positive voltage pulse of 5 V (10 msec). The variable depth of the nanostructure showed steps corresponding to three complete layers of $MoTe_2$ that were removed from the surface (the c-lattice constant for $MoTe_2$ = 0.64nm). By applying a –3 V pulse to the sample, a hexagonal shaped hole was fabricated as shown in Figure 2. 8 (b). A cross sectional analysis shows that the depth of the hole is about 0.7 nm, indicating that one complete $MoTe_2$ layer was etched away from the surface. The difference between positive and negative voltage pulses observed in nanostructure fabrication will be discussed in following mechanism section.

The nanostructures produced by the negative voltage pulses (–5 V) have a bright rim around the hole [Figure 2. 8 (a)]. The width and height of the bright feature were determined to be ~10 nm and less than 0.1 nm, respectively. In case of a –3V pulse, two

bright features, a hexagonal shape and a triangular shape protrusion, were observed around the hole [Figure 2. 8 (b)]. Similar bright features were observed at the edge of triangular shape pits on WSe_2 and MoS_2.[32-34] However, detailed explanations were not presented. Several groups including ours have previously demonstrated that dopant sites in semiconducting layered materials exhibit voltage dependent height changes when imaged with STM since the dopants can perturb the local density of states.[35-37] A sheet charge built up under an accumulation condition produced at the positive sample biases in p-type materials may cause a high electrostatic force (EF) between the top most layer of the sample and the tip apex. This leads to an increase of the measured surface height since the soft layers weakly bound to the subsurface layers are pulled up towards the tip. Even stronger effects (height changes) at the step edges were explained by either additional charges localized on edge-site dangling bonds or the lower work function at the edge sites due to the presence of an additional surface dipole, causing a stronger EF than on the flat terrace.[35-37]

The most feasible explanation for the bright rim involves electronic effects induced by dangling bond states at the edge sites in the nanostructures. The dangling bonds can be localized charge traps since their energy levels are often located in the band gap of the semiconductor. These localized trap states can contain additional static charges

that in an accumulation condition induce strong EF interactions between the localized charges and their image charges at the tip apex (positive sample bias of p-type sample). This results in pulling up the dangling bond sites at the edge of the pit. As a consequence, the feedback loop of STM retracts the tip from the surface in order to maintain constant tunneling current between the tip and sample, making that area of the sample appear as a protrusion.

The imperfection of hexagonal shape protrusion [Figure 2. 8 (b)], where one edge exhibits less or no brightness, appears to be related to different edge structures. In principle, there are four possible morphologies of $MoTe_2$ edge termination, a Te edge (I), a Mo edge (II), and both Mo and Te edges (III).

(I) Te edge

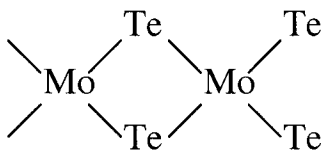

(II) Te edge

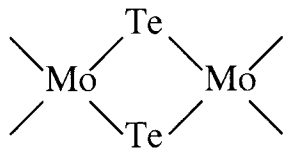

(III) Both Mo and Te edges

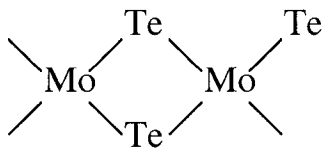

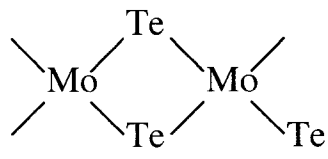

These edges would have different numbers and types of dangling bonds, resulting in a change in the tip sample interactions when the edges were imaged with STM. In case of both Mo and Te edges (III) the tip and sample interactions of two possible edges are most likely same and thus appear as same brightness in the STM images due to the same number of dangling bonds and types of atoms.

The triangular shape feature appears as an additional electronic effect involved in nanostructure produced by negative voltage pulse. It is very difficult to explain these features with only these STM images and further spectroscopic analysis and theoretical modeling would be needed to fully understand these features as was done previously.[38] These edge sites have also been implicated as active sites for HDS catalysis (refer to introduction section for details). HDS studies using STM at edge sites on MoS_2 surface are not widely reported since it is difficult to create them reproducibly. However, negative voltage pulses can generated oriented edge sites on MoS_2 surfaces in an atomic scale, implying that it has high potential to aid in the study of catalytic activity as well as the mechanism of HDS at the edge sites.

The mechanism of nanostructure fabrications on $MoTe_2$ and MoS_2

In order to explain the difference between positive and negative voltage pulses observed in nanostructure fabrication, we have to consider the electronic structure of the tunneling junction as schematically shown in Figure 2. 9. The application of positive sample voltage pulses to the p-type $MoTe_2$ results in the formation of an accumulation layer at the surface as described previous section [Figure 2. 9 (a)]. This leads to sheet charges located in the first few angstroms of both tip and sample surfaces. A sheet charge built up under an accumulation condition can cause a high electrostatic force (EF) between the top most layer of the sample and the tip apex, resulting in pulling up the top most surface layer of the sample. As a result, the electric fields between the tip and sample will be spatially localized in small area of the sample surface and the depth of built-in electric field will be restricted to the near surface (few angstroms), so that Te atoms are most likely to be etched away from the surface.

In contrast negative voltage pulses cause the surface of the sample to go into depletion or inversion [Figure 2. 9 (b)]. In the depletion region, the surface charges on the tip cannot be compensated by simply rearranging the charge densities in the top layer of the sample. Since there are very few carriers (electrons) the field penetrates into the sample surface creating a relatively thick space charge layer. This means that the EF

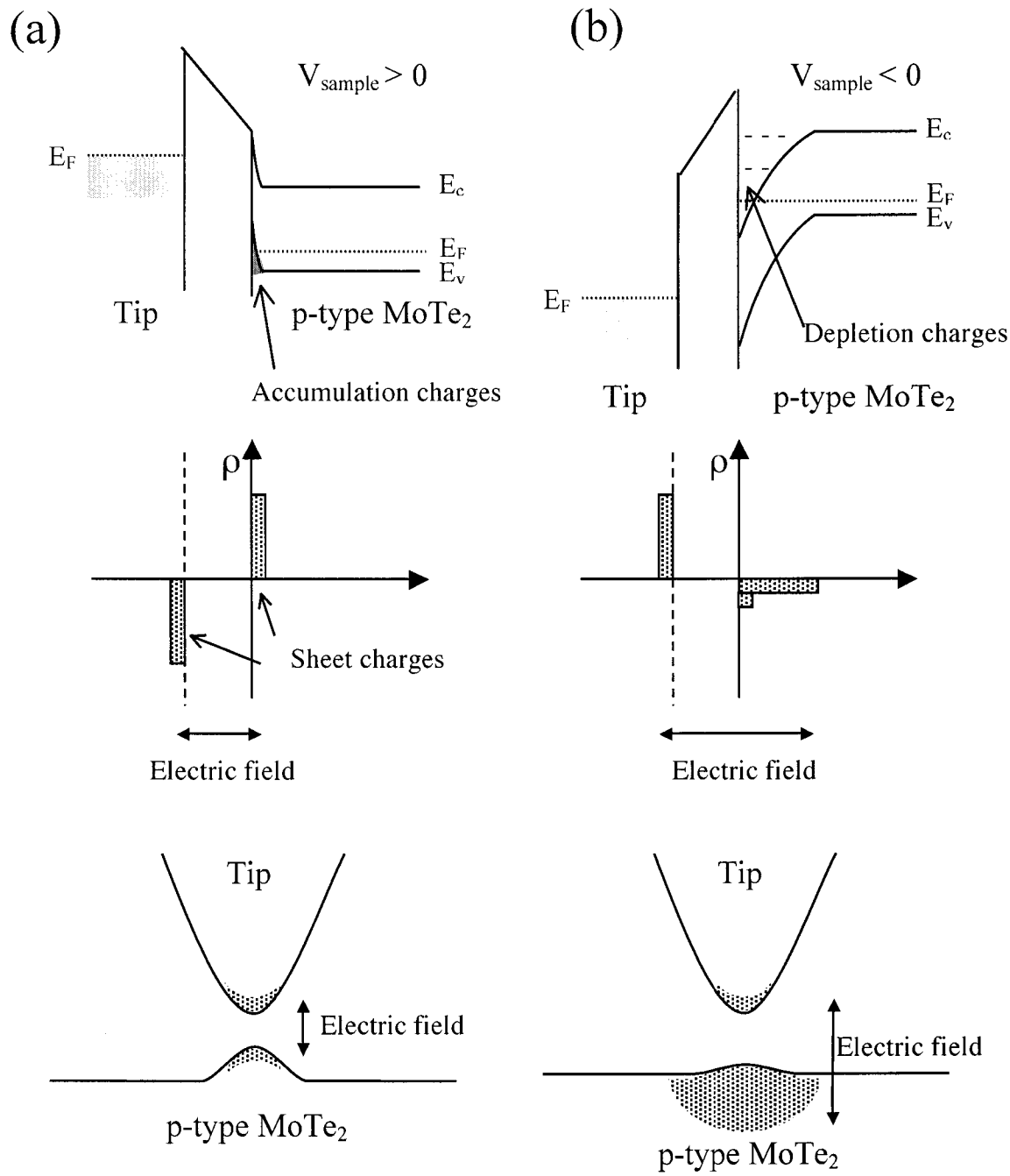

Figure 2. 9 (a) A positive sample voltage pulse causes hole "accumulation" in the p-type semiconductor. This causes a shallow electric field between the topmost layer (a few angstroms) and tip apex, resulting in detachment of only top surface Te atoms. (b) A negative sample voltage pulse causes hole 'depletion" in the p-type semiconductor. The hole depletion (or inversion) leads to electric field deep into the sample, resulting in detachment of several layers.

between tip and surface layer of sample is no longer strong enough, resulting in much weaker force on the top layer than under the accumulation condition. As a result, the electric fields will be generated from the tip through the space charge layer. Therefore, more than one complete layer can be under the influence of built-in electric fields, resulting that several complete layers can be etched away from the sample depending on the thickness of the space charge layer (depletion region).

A mechanical contact mechanism does not seem to be involved with the nanostructure fabrication of $MoTe_2$ and MoS_2 due to the observed flexibility of TMD's. The generation of the larger and deeper holes at the negative voltage pulses is opposite to the electron bombardment mechanism suggested by Kondo *et al.*[25] where negative voltage pulses cause only the tip materials to be etched, resulting in no damage on the substrates. The existence of threshold voltages for the surface modification and pulse polarity dependence of nanostructure fabrication suggest that an electric field evaporation mechanism is applicable to nanostructure fabrication in $MoTe_2$ and MoS_2. This is supported by the fact that voltage pulses applied without moving the tip toward the surface do not generate nanostructures. However, even though field evaporation may be the mechanism where the modification process is initiated, other processes such as

thermal and/or current effects most likely contribute to the later stages of material removal.

2. 4 Conclusions

We have used the STM to generate atomic scale nanostructures on $MoTe_2$ and MoS_2 surfaces by applying voltage pulses between the tip and sample. There exist distinct threshold voltages for surface modification of $MoTe_2$ and MoS_2 surfaces, 3.0 ± 0.3 V and 3.4 ± 0.3 V, respectively. It was found that the geometry of the STM tips (tip sharpness and shape) plays an important role in nanostructure fabrication. An extrapolation of this data predicts that small tip apex radii can produce atomic scale features. Positive voltage pulses applied to the sample removed only chalcogens (Te or S atoms) from the top most surface whereas negative voltage pulses etched away more than one complete layer of $MoTe_2$ depending on the magnitude of voltage pulses. This polarity dependence of nanostructure fabrication was explained by the difference of the magnitude of applied electric fields. The mechanism of atom removal by STM voltage pulses is discussed on light of our data.

References

[1] D. M. Eigler and E. K. Schweizer, Nature **344,** 524 (1990).

[2] A. Kobayashi, F. Grey, R. S. Williams, and M. Aono, Science **259,** 1724-1726 (1993).

[3] Q. J. Gu, N. Liu, W. B. Zaho, Z. L. Ma, Z. Q. Xue, and S. J. Pang, Appl. Phys. Lett. **66,** 1747-1749 (1995).

[4] K. Besso and S. Hashimoto, Appl. Phys. Lett. **65,** 2142-2144 (1994).

[5] S. Heike, T. Hashzume, and Y. Wada, J. Appl. Phys. **80,** 4182-4188 (1996).

[6] S. Heike, Y. Wada, and T. ashizume, J. Appl. Phys. **86,** 4220-4224 (1999).

[7] H. Fukuzawa, H. Kimijima, N. Yoshikawa, and M. Sugahara, Jpn. J. Appl. Phys. **34,** L1221-L1223 (1995).

[8] Z. Ma, C. Zhu, J. Shen, and S. Pang, Vacuum **43,** 1115-1117 (1992).

[9] J. Y. Park and R. J. Phaneuf, J. Appl. Phys. **92,** 2139-2143 (2002).

[10] C. Mascher and B. Demaschke, J. Appl. Phys. **75,** 54385440 (1994).

[11] J. P. Song, N. H. Pryds, K. Glejbol, K. A. Morch, a. R. Tholen, and L. N. Christensen, Rev. Sci. Instrum. **64,** 900-903 (1993).

[12] N. Li, T. yoshinobu, and H. Iwasaki, Appl. Phys. Lett. **74,** 1621-1623 (1999).

[13] S. L. Tang, A. J. McGhie, and M. E. Lewittes, Appl. Phys. Lett. **60,** 1821-1823 (1992).

[14] S. M. York and F. M. Leibsle, Appl. Phys. Lett. (2001).

[15] J. Huang, Y. Sung, and C. M. Lieber, Appl. Phys. Lett. **61,** 1528 (1992).

[16] S. Hosoki, S. Hosaka, and T. Hasegawa, Appl. Surf. Sci. **60/61,** 643-647 (1992).

[17] S. Hosoka, S. Hosoki, T. Hasegawa, T. Koyanagi, T. Shintani, and M. Miyamoto, J. Vac. Sci. Technol. B **13,** 2813-2818 (1995).

[18] T. Schimmel, R. Kemnitzer, J. Kuppers, H. Fuchs, and M. Lux-Steiner, Thin Solid Films **254,** 147-152 (1995).

[19] R. G. Garcia, Appl. Phys. Lett. **60,** 1960-1962 (1992).

[20] T. Schimmel, H. Fuchs, and M. Lux-Steiner, Phys. stat. sol. **131,** 47-57 (1992).

[21] E. M. Slayter, *Light and electron microsopy* (Cambridge University Press, New York, 1992).

[22] I. Lyo and P. Avouris, Science **253,** 173-176 (1991).

[23] T. T. Tsong, Phys. Rev. B **44,** 13703-13710 (1991).

[24] C. Wang, C. Bai, X. Li, G. Shang, I. Lee, X. Wang, X. Qui, and F. Tian, Appl. Phys. Lett. **69,** 348-350 (1996).

[25] S. Kondo, S. Heike, M. Lutwyche, and Y. Wada, J. Appl. Phys. **78,** 155-160 (1995).

[26] H. J. Mamin, P. H. Guethner, and D. Rugar, Phys. Rev. Lett. **65,** 2418-2421 (1990).

[27] N. Oyabu, Q. Custance, I. Yi, Y. Sugawara, and S. Morita, Phys. Rev. Lett. **90,** 176102 (2003).

[28] T. R. Albrecht, M. M. Dovek, M. D. Kirk, C. A. Lang, C. F. Quate, and D. P. E. Smith, Appl. Phys. Lett **55,** 1727 (1989).

[29] R. Koning, O. Jusco, L. Koenders, and A. Schlachetzki, J. Vac. Sci. Technol. B **1996,** 48-53 (1996).

[30] U. Staufer, R. Wiesendanger, L. Eng, L. Rothenthaler, H. R. Hidber, H.-J. Guntherodt, and N. Garcia, Appl. Phys. Lett. **51,** 244-246 (1987).

[31] T. Schimmel, H. Fuchs, S. Akari, and D. Dransfeld, Appl. Phys. Lett. **58,** 1039-1041 (1991).

[32] B. A. Parkinson, J. Am. Chem. Soc. **112,** 7498-7502 (1990).

[33] J. Boneberg, M. Lohrmann, M. Bohmisch, M. Burmeister, M. Lux-Steiner, and P. Leiderer, Z. Phys. B **99,** 567-570 (1996).

[34] S. Akari, R. Moller, and D. Dransfeld, Appl. Phys. Lett. **59,** 243 (1991).

[35] T. W. Matthes, C. Sommerhalter, A. Rettenberger, P. Bruker, J. Boneberg, M. C. Lux-Stainer, and P. Leiderer, Appl. Phys. A **66,** S1007-S1011 (1998).

[36] R. Schlaf, D. Louder, M. W. Nelson, and B. A. Parkinson, J. Vac. Sci. Technol. A **15,** 1466-1472 (1997).

[37] R. Schlaf, P. G. Schroeder, M. W. Nelson, R. Stubner, S. Tiefenbacher, H. Jungblut, and B. A. Parkinson, Thin Solid Films **331,** 203-209 (1998).

[38] M.-H. Whangbo, J. Ren, S. N. Magnov, H. Bengel, B. A. Parkinson, and S. A., Surf. Sci. **326,** 311-326 (1995).

Chapter 3

STM investigation of nanostructures produced by Ar^+ and He^+ bombardment of MoS_2 surfaces

(This chapter has been submitted to the Journal of Vacuum Science Technology B for publication)

3. 1 INTRODUCTION

Molybdenum disulfide (MoS_2) is a layered material consisting of stacked chalcogenide-metal-chalcogenide layers held together by van der Waals interactions.[1,2] Sulfur atoms on the basal planes of MoS_2 have a complete coordination sphere below the plane, making them relatively unreactive. Despite the inert basal plane, MoS_2 has been of interest due to its catalytic activity for hydrodesulfurization (HDS) where organic sulfur is removed from petroleum and coal feedstocks by reaction with hydrogen gas to form

H_2S.[3,4] The catalytic activity of MoS_2 for HDS has been associated with edge sites, which are more numerous on the small particles employed in supported HDS catalysts.[5-11] Basal plane defects (sulfur vacancies) produced at high temperatures during HDS have been also proposed to be active catalytic sites.[12,13] The structure of MoS_2 impacts lubricating properties due to the ease of slippage between cleavage planes.[14-16]

The easy cleavage of MoS_2 and other layered transition metal dichalcogenides (TMD's) ($MoSe_2$, WS_2, WSe_2...) can produce large, stable, and atomically flat areas, making these materials ideal substrates for scanning tunneling microscopy (STM) investigations. Various natural defects such as ring shape structures, topological hillocks, and depressions have been observed on the MoS_2 crystal surfaces with STM.[17-24] Natural defects have been interpreted as impurities intercalated between van der Waals layers produced during the natural formation process.[24] Secondary ion mass spectrometry (SIMS) of natural MoS_2 crystals was used by Permana et. al. to show that these natural defects could be caused by intercalated vanadium or fluoride ions. These ions have been imaged as protrusions and ring structures depending on their ionic charges.[19] A later study by Ha and coworkers supported these results by analyzing impurities using glow discharge mass spectroscopy (GDMS).[18] Titanium and vanadium induced electronic effects that produced band bending near the impurities and were suggested to produce the

ring structures in STM images. Matthes et. al. proposed that the topological contrast and the ring structure near acceptor sites on p-type WSe_2 were induced by two competing tunneling current mechanisms involving tunneling into valence band and conduction band states.[20] The effect of impurity atoms on STM image imperfections has been investigated by doping $MoSe_2$ with Re and depositing alkali metal atoms onto MoS_2.[25] All of impurity atoms were imaged at negative sample biases as bright ring shape features surrounded by depressions whereas the bright features disappeared at positive sample biases. It was suggested that these locally modulated structures were induced by interactions between excess electrons donated by impurity atoms and electrons in d-orbitals of neighboring Mo atoms. Whangbo et. al. attempted to classify STM images of point defects through a theoretical analysis.[23] However, the exact chemical nature of these natural defects in STM images still remains unknown.

Basal planes of MoS_2 have been ion sputtered to study their catalytic activity[26] and to fabricate nanostructures.[27] Ar^+ sputtering of MoS_2 in vacuum resulted in large increases in the catalytic activity when compared with unsputtered MoS_2.[26] Ar^+ sputtering is believed to remove S atoms and expose coordinately unsaturated Mo atoms that act as active sites. It has been reported that 3keV Ar^+ bombardment produced preferential sputtering of sulfur atoms from MoS_2 powder, resulting in a surface composition of

$MoS_{1.12}$.[28] Ar^+ bombardments of WSe_2, at the energies between 5 and 10 keV, produced nanostructures with diameters less than 10 nm as imaged with STM.[27] Sengogu, et. al showed that 1 keV Ar^+ bombardments on MoS_2 basal plane produced nanostructures with a bright feature at the center of a dark region.[29] They proposed that the bright features contained negatively charged sulfur atoms and dark regions were attributed to electron depletion due to the coulomb repulsion around the negatively charged species.

Nanostructures have also been produced by low energy ion bombardment of another layered material, graphite, where the nanostructures produced by ion bombardment appear as protrusions in STM images.[30-38] Several interpretations of these features have been put forward: First, STM images of the graphite surface bombarded with low energy Ar^+ (~50 eV) exhibited point defects as well as dome-like structures (protrusions).[31-33] It was postulated that Ar^+ penetrate the topmost layer, and are trapped between the first and second layer of graphite sheets. These trapped ions deform the carbon network and appear as topological protrusions in the STM images. Secondly, thermal spike effects have been used to explain hillocks created by single ion impacts on the basal plane of graphite.[34,35] In this model a portion of the impinged ion energy is transferred to the lattice causing a locally intense lattice vibration. If the local temperatures as a result of the lattice vibrations were sufficiently high, permanent

rearrangement of the lattice atoms through migration and diffusion would be induced giving rise to the observed hillocks. Finally, atomic vacancies produced on a graphite surface by Ar^+ bombardment with low energies (50~80eV) could enhance the density of states (DOS) at the surrounding carbon atoms.[30] This DOS increase appears to be concentrated in both filled and empty states near the Fermi level (E_F) producing hillock structures in STM images. These structures were not imaged with atomic force microscopy (AFM), indicating that these protrusions are electronic rather than topological effects.[30]

Even though sputtering has been widely used in MoS_2 investigations, a systematic investigation of the sputtering phenomenon has not been reported. The purpose of our study is to use STM to investigate the initial stages of sputtering MoS_2 with the atomic scale resolution. Specifically, we report on the production and morphological characterization of nanostructures on MoS_2 generated by Ar^+ and He^+ bombardment with energies between 100eV and 5keV.

3. 2 EXPERIMENTAL METHODS

Different sources of natural MoS_2 crystals (obtained from Colorado in the USA, Australia, and Quebec in Canada) were examined to find crystals with low defect

densities, since a high density of natural defects makes it difficult to distinguish nanostructures produced by ion sputtering. Natural MoS_2 crystals from Colorado, showing the lowest defect density (~200 defects per μm^2), were selected for our experiments. Clean and atomically flat MoS_2 surfaces were prepared by cleaving in air using adhesive tape immediately prior to insertion into the UHV chamber.

All experiments were performed in a commercial Omicron Multi-Probe ultrahigh vacuum (UHV) system, with a base pressure of 5×10^{-11} mbar, equipped with a variable temperature scanning tunneling microscope (VT-STM), XPS and an ion sputtering source (IES 100). MoS_2 crystals were irradiated at room temperature with a rastered Ar^+ and He^+ beam from the Omicron ISE 100 ion gun with acceleration energies ranging from 100eV to 5 keV and the ion flux between 7.0×10^2 ions/μm^2sec and 1.2×10^3 ions/μm^2sec. The bombarded samples were characterized *in situ* using the VT-STM and XPS. STM measurements were performed with electrochemically etched tungsten tips. All of the images shown here were taken at room temperature in the constant current mode with a tunneling current of 1 nA at sample biases, ranging from -1.0 V to +1.0 V. After image acquisition, a background plane fit was applied to all of the images. Some high-resolution STM images were enhanced through the lateral linearity calibration and plane correction

process using a commercially available scanning probe image processing software (SPIP™, Image Metrology).

3. 3 RESULTS AND DISCUSSION

Nanostructure fabrication by Ar^+ bombardments on MoS_2

Figure 3. 1 (a) shows a 150 nm × 150 nm STM image of a typical MoS_2 surface before Ar^+ sputtering. The small white protrusions are natural defects in this sample. The difference between the maximum and minimum height in the image was less than 0.2nm and the average natural defect diameter and height with a - 0.1 V sample bias was determined to be 5.0 nm and 0.2 nm, respectively. The surface density of natural defects was about 200 μm^{-2} corresponding to a doping density of 10^{17} cm^{-3} if it is assumed that dopants are only imaged in the top three layers of MoS_2 as has been previously reported.[20,39] Figure 3. 1(b) and (c) show STM images obtained after the sample was bombarded with Ar^+ of different energies. Ar^+ sputtering creates randomly scattered circular depressions (dark spots) on the surface. Ar^+ energies of more than 100eV produce nanostructures with protrusions (bright spots) on the surface as shown in Figure

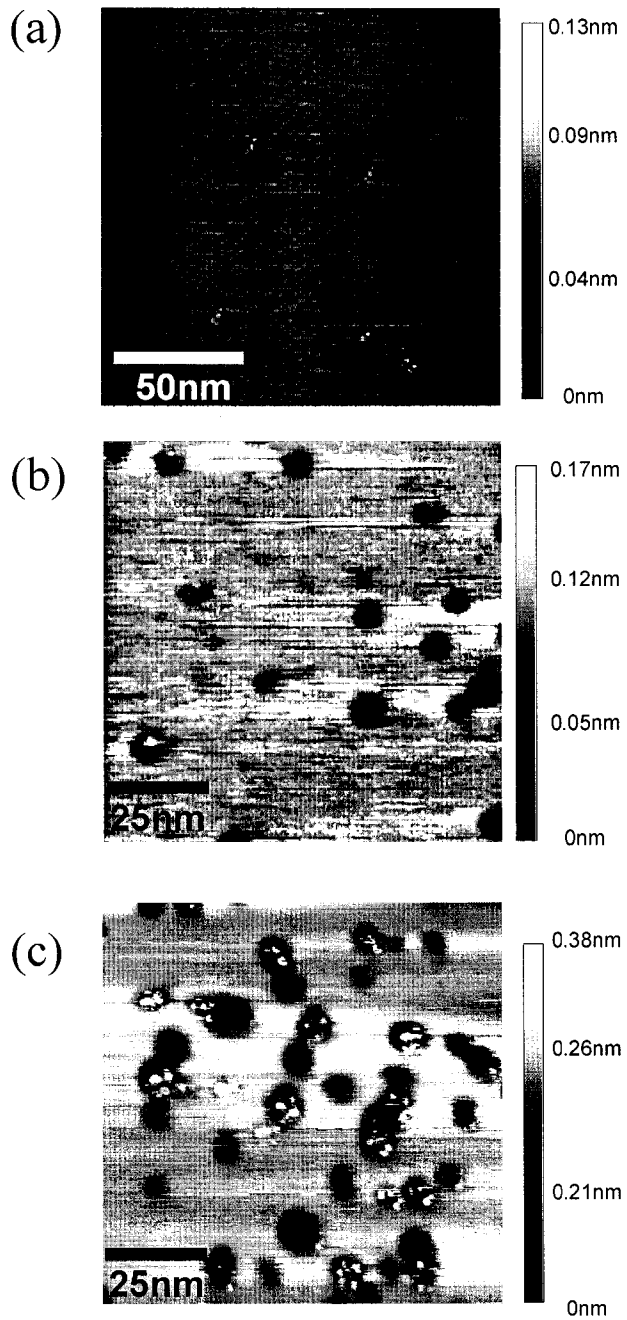

Figure 3. 1 (a) 150 nm × 150 nm image of MoS_2 before Ar^+ bombardment. Each white protrusion indicates a natural defect. (b) and (c) show 100nm × 100nm STM images of a nanostructured MoS_2 surface after Ar^+ sputtering with energies of 100 eV and 500 eV, respectively. The scanning conditions for all images are: sample bias = -0.1V, tunneling current = 1.0nA, and scanning rate = 5 Hz, and room temperature. Min./Max. height difference: (a) 0.17nm, (b) 0.24nm, and (c) 0.31 nm

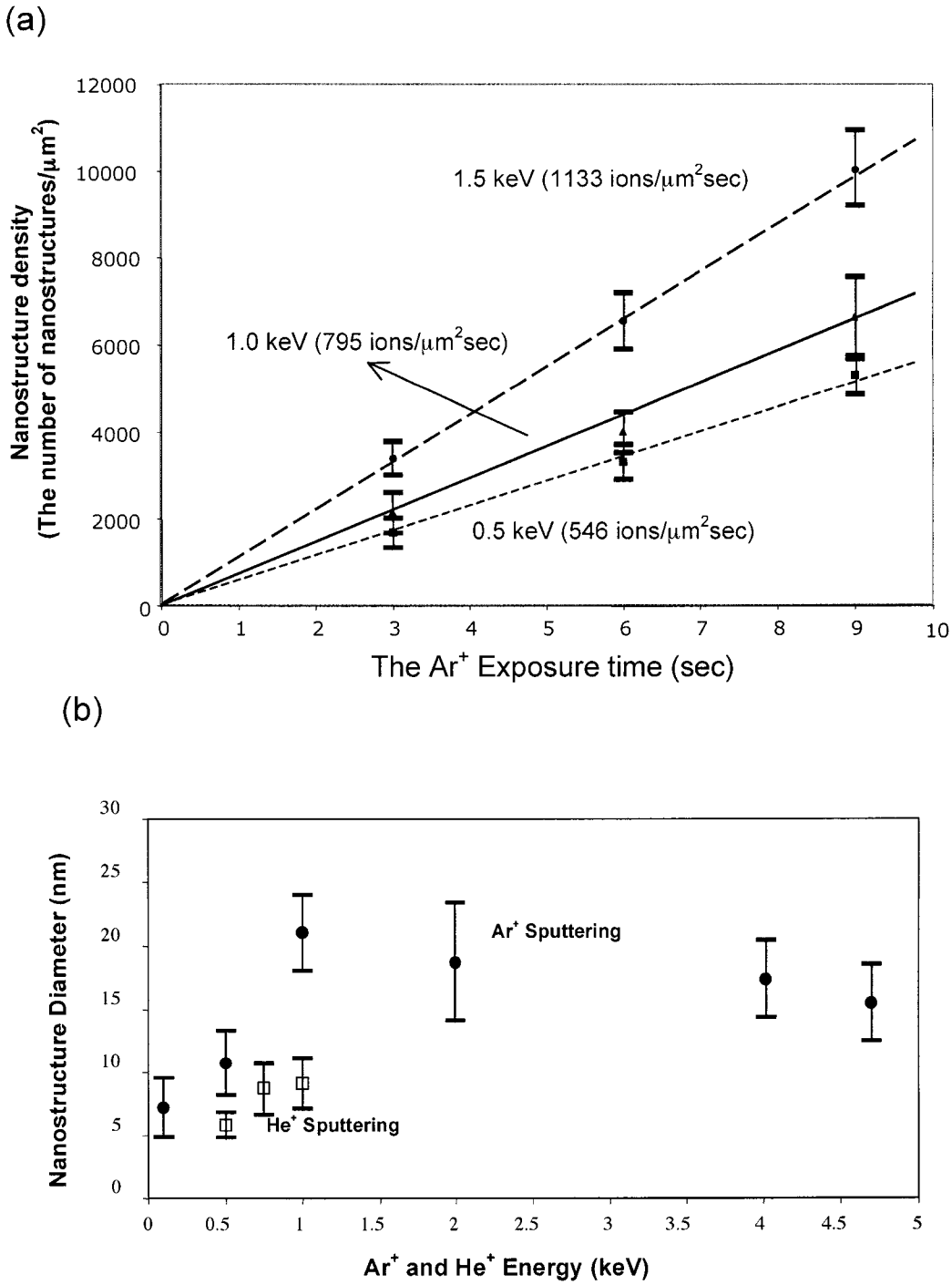

Figure 3. 2 (a) The density of nanostructures as a function of the dose of Ar^+ at three different Ar^+ energies 500 eV, 1 keV, and 1.5 keV. (b) The distributions of nanostructure diameters plotted as a function of Ar^+ and He^+ energy at normal incidence.

3. 1(c), whereas the nanostructures produced by 100eV Ar^+ bombardment usually did not [Figure 3. 1(b)].

Figure 3. 2(a) shows the density of nanostructures (the number of nanostructures/μm^2) as a function of ion exposure time (dose) at three different Ar^+ energies, 500 eV, 1.0 keV and 1.5 keV. Note that the produced nanostructure density is well above the background of natural defects (200 μm^{-2}). An ion flux of 7.0×10^2 ions/μm^2sec was used for 500 eV Ar^+ sputtering while 8.7×10^2 ions/μm^2sec and 1.2×10^3 ions/μm^2sec were used for 1keV and 1.5 keV, respectively. The error bars indicate the standard deviations in the measured density of nanostructures. A linear relationship was obtained between the ion dose and density of nanostructures at the fixed sputtering energy and ion flux, indicating that each nanostructure is fabricated by an individual Ar^+ impact on the surface.

Based on nanostructure density from the STM images [Figure 3. 2 (a)] and the calculated ion dose, the sputtering yields (a ratio of generated nanostructures per an ion impact) of Ar^+ for the MoS_2 sample with energies of 500 eV, 1 keV and 1.5 keV were determined to 0.77, 0.92 and 0.95 nanostructures/ion, respectively. It appears that the sputtering yield remains close to 1 at the energies of 1 keV and 1.5 keV within experimental errors (the number of features observed from the STM images corresponded

to the calculated dose) while it slightly decreases at 500 eV. This trend is quite comparable to gallium ion bombardments on graphite where a focused ion beam was utilized to expose graphite substrates to gallium ions with energies ranging from 10 eV to 2.5 keV.[40] For ion energies of 250 eV and above, every ion impact generated cluster-like protrusions of 1 ~ 5 nm in diameter (sputtering yields were close to 1). As ion energy is decreased from 100 eV to 10 eV, the sputtering yield decreased from 0.1 to 0.01 and it became negligible below 10 eV.

When ions impinge on a solid surface a series of complex interactions occur by which the primary ions transfer a part of their energy and momentum to the solid.[41-43] The primary ions can be back scattered from the surface and target atoms can recoil into or out of the surface. In addition, some fraction of the energy of the impinged ions can be transferred to the solid in the form of local heating that can also create lattice damage. The deposited energy can cause target atoms to undergo a series of collisions, called collision cascades, where some atoms near the surface receive a sufficient kick to leave the target surface, resulting in atomic vacancies. Other defects such as substitutional impurities, interstitials (an atom moves into a site in the lattice that is not occupied by a lattice atom), and Frenkel pairs (vacancies-interstitial pairs) can also be produced. At much higher ion energies impinged ions spend less time near the surface, due to the fast

ion velocities, and are most likely embedded deep into the target, the basis of ion implantation. Finally, as a result of these perturbations, the solid can emit photons and electrons.

STM imaging of the nanostructures produced by ion bombardment revealed that, in general, the higher energy ions produced larger nanostructures. The distribution of nanostructure diameters is plotted as a function of Ar^+ energy in Figure 3. 2(b). For each ion energy more than 40 nanostructures were measured in order to obtain good statistics for the nanostructure diameter. The average diameter of the nanostructures on a 100 eV Ar^+ sputtered MoS_2 surface was determined to be 7.2 ± 2.3 nm. 500 eV and 1 keV Ar^+ ions produce nanostructures with the diameters of 10.7 ± 2.6 nm and 21.1 ± 3.0 nm, respectively. The diameters increase with the Ar^+ energy up to 1 keV, after which there is little change.

To obtain detailed information about the nanostructure diameter dependence on the impinged ion energies, Ar^+ bombardments on MoS_2 surface were simulated by a Monte Carlo method (TRIM 2003).[44] In the simulation, the MoS_2 target was treated as repeated sulfur-molybdenum-sulfur amorphous layers. The densities of sulfur and molybdenum layers were 2.1 g/cm^3 and 10.2 g/cm^3, respectively and the interactions between layers were ignored. This MoS_2 target was bombarded with Ar^+ ions with

acceleration energies ranging from 100 eV to 5.0 keV at surface normal. It was found that the probability of ion implantation increased with impinged ion energies. However, the sputtering yields of sulfur atoms in the top sulfur layer increased with Ar^+ energy up to 1 keV while at Ar^+ energies greater than 1keV, the sputtering yields began to decrease. These results imply that the size of the nanostructures may increase with Ar^+ energy up to 1 keV due to the increased probability of starting collision cascades that locally enlarges the nanostructure. At Ar^+ energies greater than 1keV, ion implantation becomes a more probable process. The larger ion energy likely increases the penetration depth of the ions, resulting in a small decrease of nanostructure size due to more energy dissipation deeper in the crystals, which is not detected by the surface sensitive STM. The nanostructures created on MoS_2 were quite stable over time. They could still be observed even after imaging the surface for more than 12 hours. Ion sputtered gold surfaces showed the nucleation and growth of holes from the merger of closely spaced holes produced by Ar^+.[45] However, gold atoms are known to be mobile at room temperature whereas the strong covalent bonds in MoS_2 would not allow atom movement at room temperature.

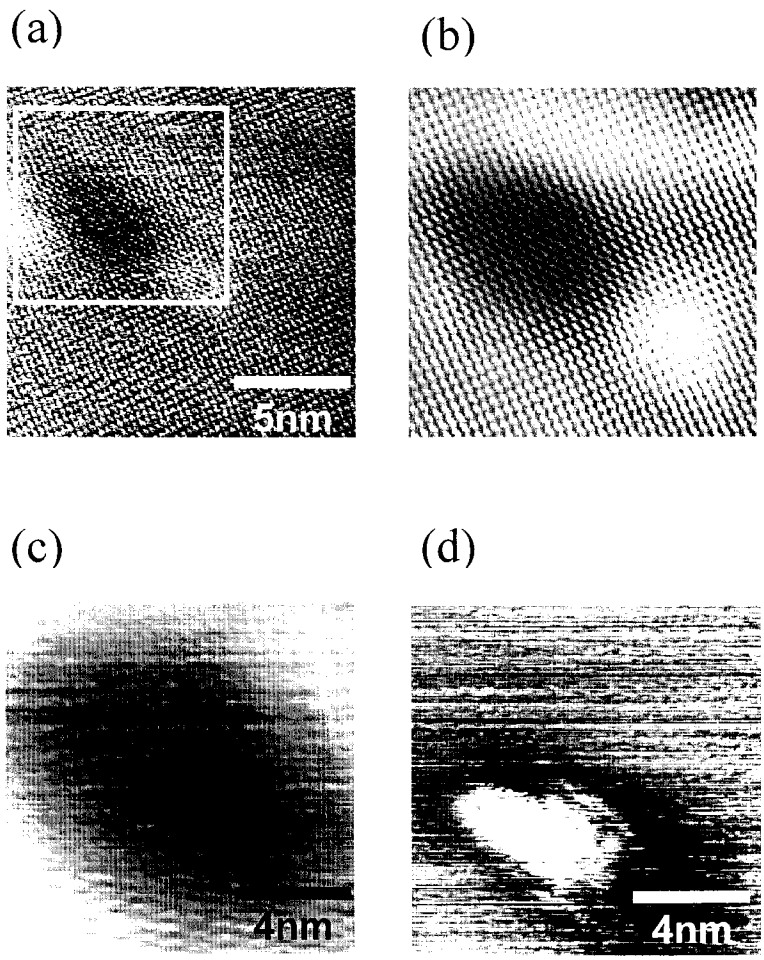

Figure 3. 3 STM images of a 100 eV Ar^+ bombarded MoS_2 surface. (a) 15 nm × 15 nm image of a nanostructure. (b) A magnified and SPIP processed image of the nanostructure in (a). (c) 12 nm × 12 nm image of a nanostructure at the tunneling sample bias of -0.1V and tunneling current of 1.0nA. (d) The same nanostructure image as (c) at the tunneling sample bias of -1.0V and same current.

Atomic scale investigation of nanostructures produced by 100eV Ar^+ bombardments

Figure 3. 3 presents atomically resolved STM images of nanostructures created by 100eV Ar^+ bombardments. Figure 3. 3 (a) and (b) show the same nanostructure where Figure 3. 3 (b) is an enlarged and processed image of Figure 3. 3 (a) (refer to experimental section for details). The bombarded and surrounding areas show that the atomic order of the sulfur lattice is preserved. The lack of missing sulfur atoms inside the nanostructures indicates that 100eV Ar^+ did not physically remove sulfur atoms from the MoS_2 surface, however it did induce damage on or near the MoS_2 surface that imaged by the STM. Figure 3. 3 (c) and (d) show STM images of the other type of nanostructure produced by 100 eV Ar^+ bombardments under different scanning conditions (sample bias for Figure 3. 3 (c) = - 0.1 V and sample bias for Figure 3. 3 (d) = - 1.0 V). The depression at - 0.1 V sample bias appears as a protrusion at a - 1.0 V sample bias.

Previous reports have shown similar height changes in STM images of point defects on TMD's (i.e. atomic vacancies and substitutions) when the tunneling bias is changed.[22,23,46] For example, shallow donors and acceptors give rise to energy states between the conduction and valence bands. Those are localized in the vicinity of the defect sites and can influence the electron tunneling process. The polarity and the magnitude of imaging bias strongly affects the tunneling process and can perturb these

states, resulting in bias dependent height changes. This modified local density of states (LDOS) also affects the electrostatic force (EF) acting between the tip and sample, which can also result in apparent height changes in STM images.[22] A purely topological depression or protrusion, not associated with altered electronic states, should have the same dark or bright appearance under both tunneling conditions. Therefore, the height changes measured for the nanostructures in Figure 3. 3 (c) and (d) are most likely the result of differences in the density of electronic states near the band gap and thus a change of the EF between the tip and sample. More detailed discussions of this phenomenon will be presented in following sections.

Baker et al. have used XPS to demonstrate preferential sputtering of sulfur atoms from MoS_2 powder by using the Mo $3d_{5/2}$ peak shift and the Mo/S ratios to determine that after extensive sputtering the surface elemental stoichiometry changes from MoS_2 to $MoS_{1.12}$.[28] A peak shift from 229.25 to 228.35 eV was caused by changes in the chemical environment around Mo atoms as a result of the loss of sulfur atoms. Lince et. al. showed that 10 keV Ar^+ sputtering of natural MoS_2 crystals results in shifts of both Mo $3d_{5/2}$ and S $2p_{3/2}$ peaks to lower binding energy (~0.85 and ~0.73 eV, respectively) and a drop of ~ 15 % in the S/Mo peak area ratio indicating the preferential sputtering of sulfur.[47] The shift of the Mo $3d_{5/2}$ photoemission peak was caused by a lowering of the Mo^{4+} oxidation state

within the depth range of the detected photoelectrons. However, an appropriate explanation was not presented for the S $2p_{3/2}$ peak shift.[47]

We also used XPS to look for any changes in the Mo-S bonding environment induced by 100 eV Ar^+ sputtering. It was observed that the Mo $3d_{5/2}$ and S $2p_{3/2}$ peaks progressively shifted from 230.1 eV to 229.4 eV and from 163.3eV to 162.5eV, respectively, during sputtering (total 5 min) at an Ar^+ beam energy of 100 eV. The 230.1 eV and 163.3 eV peaks are assigned to Mo^{4+} and S^{2-} of intact MoS_2 [Figure 3. 4 (a) and (b)]. The Mo $3d_{5/2}$/S $2p_{3/2}$ peak ratios before and after Ar^+ sputtering of MoS_2 were determined to be identical, indicating that within experimental error no sulfur atoms are removed from the MoS_2. On the other hand, the FWHM (the full width at half-maximum) for Mo $3d_{5/2}$ and S $2p_{3/2}$ peaks broadens by ~ 13% and ~7%, respectively. The peak broadening in both the Mo and S spectra after Ar^+ sputtering is not surprising, because ion sputtering of a solid causes defect formation and, consequently, a loss of symmetry in the crystal lattice. Such a loss of symmetry affects the local electronic environment of each atomic type in the lattice differently, and a greater binding energy (BE) width is detected for each element.

(a)

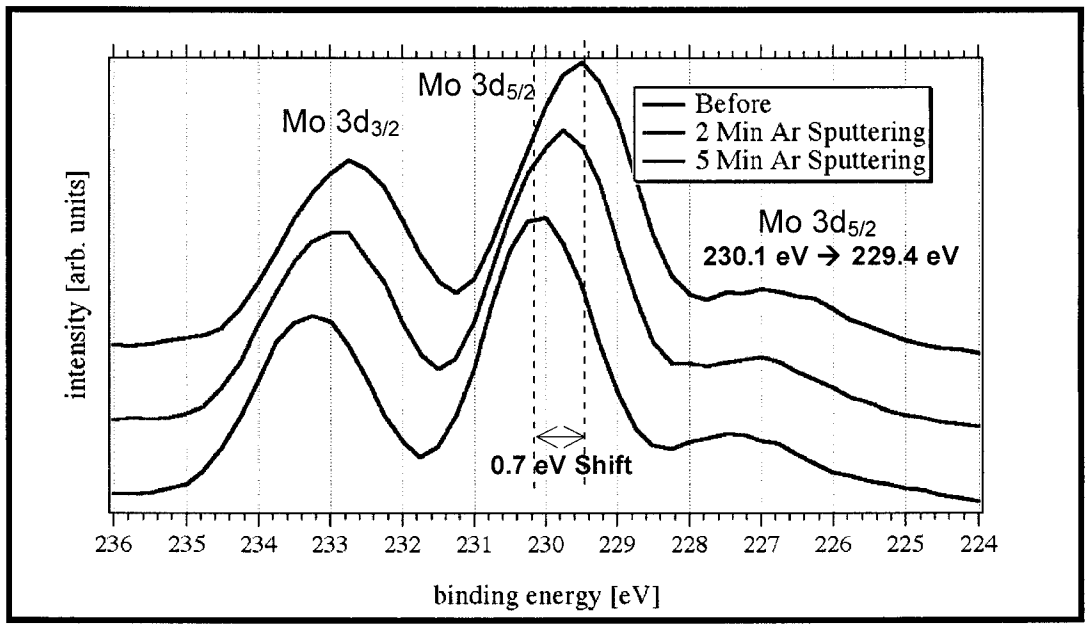

(b)

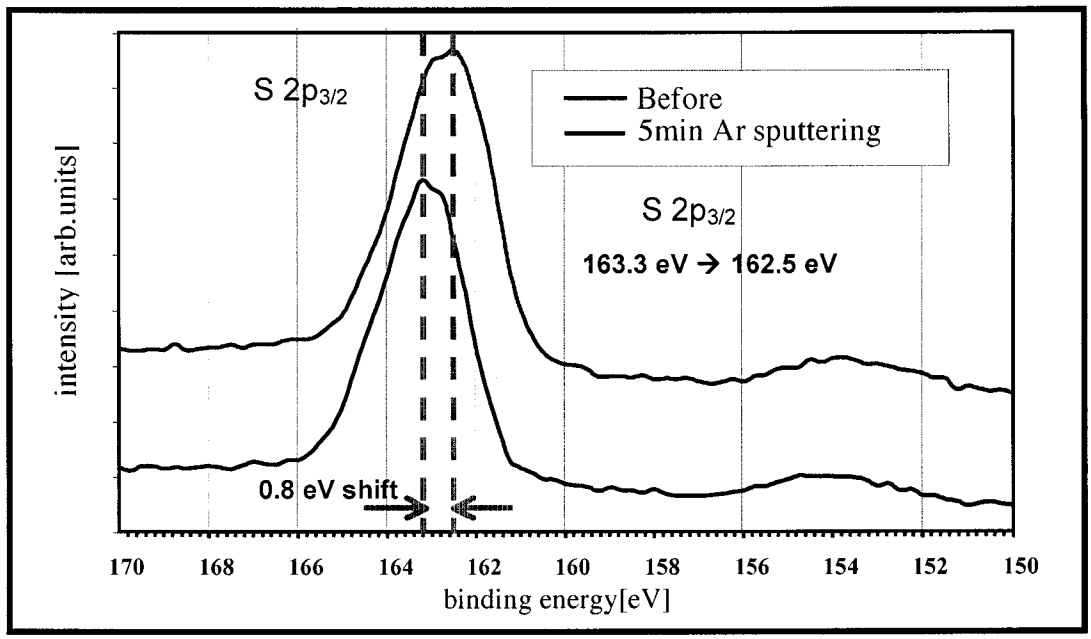

Figure 3. 4 XPS spectra obtained before and after Ar^+ sputtering of MoS_2 surface with the energy of 100 eV (total 5 min.). The binding energies of 230.1 eV and 163.3 eV are assigned to (a) Mo $3d_{5/2}$ and (b) S $2p_{3/2}$ of intact MoS_2.

The most interesting effect of Ar^+ bombardment is that both the Mo and sulfur peaks shift to lower binding energies by ~ 0.7 eV and ~ 0.8 eV, respectively. These peak shifts cannot be explained by local changes in the chemical environment for Mo-S bonding (changes of formal oxidation state) since sulfur cannot be reduced further than an oxidation state of -2. These peak shifts may be caused by the fact that 100eV Ar^+ sputtering changes the density of electronic states near the surface. During the Ar^+ sputtering, the impinged Ar^+ induce surface damage that produces dopant states. The dopant states induced by Ar^+ sputtering are p-type or acceptor states as judged by their contrast dependence on STM imaging bias,[20,23] whereas the natural background defects are n-type since they have the opposite contrast relationship [Figures 3. 1(a) and 1(b)]. A calculation of the number of surface defects created shows that there are enough to compensate the natural n-type defects and to then produce a p-type surface with a doping density of about $4.2 \times 10^{18} cm^{-3}$.[48] The expected shift in the surface Fermi level (E_F) from n-type to p-type is about 0.7 eV (the band gap of MoS_2 is about 1.2 eV[49]) very near the value of the binding energy shift for the Mo $3d_{5/2}$ and S $2p_{3/2}$ peaks. We therefore attribute the parallel shift to lower binding energy in both Mo $3d_{5/2}$ and S $2p_{3/2}$ peaks to shift of E_F of MoS_2 to a more positive value due to a change in surface doping density. These results

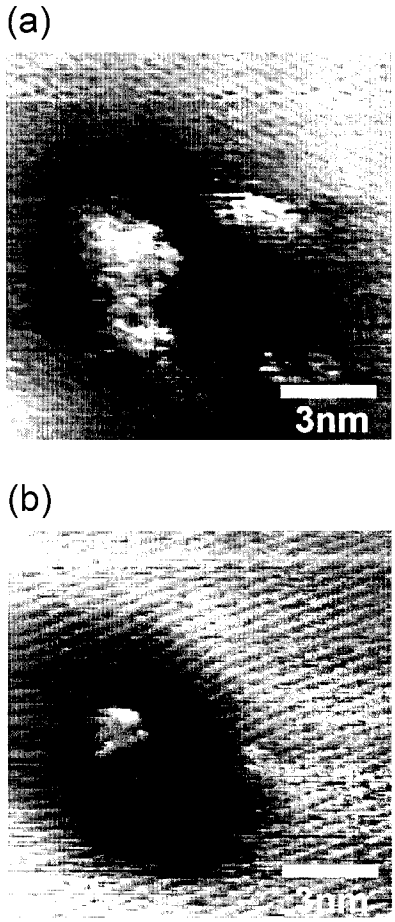

Figure 3. 5 Two different types of nanostructures produced by 500eV Ar^+ bombardment of a MoS_2 surface: (a) 12 nm × 12nm (Type A) (b) 12 nm × 12 nm (Type B). The scanning conditions for all images are: sample bias = -0.1V, tunneling current = 1.0 nA, and scanning rate = 5 Hz, and room temperature.

indicate that, even though 100eV Ar^+ sputtering does not effectively remove sulfur atoms from the surface, changes in the electronic structure do occur that are observable with STM.

Atomic scale investigation of nanostructures produced by Ar^+ bombardments with the energies greater than 100eV

Figure 3. 5 shows atomically resolved STM images of nanostructures created by 500 eV Ar^+ impacts. Two types of nanostructures were commonly observed type A [Figure 3. 5 (a)] and type B [Figure 3. 5 (b)]. The density of Type A and B nanostructures were nearly equal. The type A nanostructure has a central crater surrounded by protrusions (hillocks) [Figure 3. 5 (a)]. The average height of the protrusions was determined to be 0.2 nm or approximately 1 atom high. Protrusions generated with higher Ar^+ energies were of similar height. It appears that the protrusions are produced by the deposition of sputtered material or more likely by the deformation of the lattice near the crater via ion-atom collisions and/or backscattered atoms. Figure 3. 5 (b) shows the type B nanostructure produced where the protrusion exists inside a crater

The protrusions are unlike natural defects since they are three times wider. 1 keV Ar^+ can be implanted into graphite, since ions implanted with energies ranging from

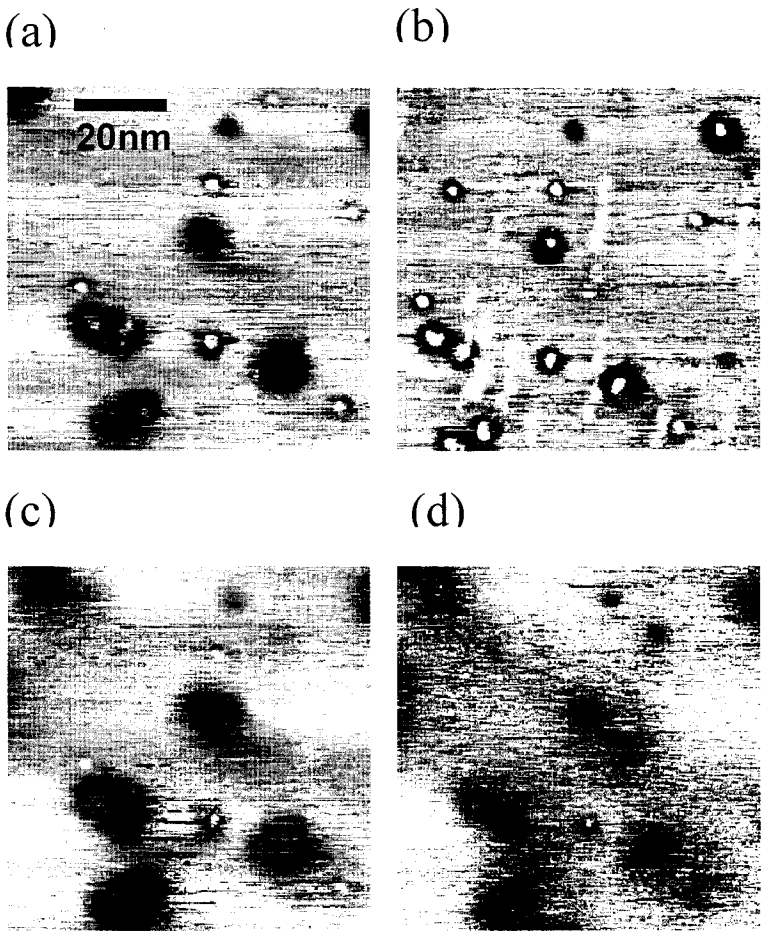

Figure 3. 6 A series of four STM images of nanostructures taken from the same area bombarded with 1keV Ar^+ beam at different tunneling sample bias of (a) -0.1 V, (b) -0.5 V, (c) +0.1 V, and (d) +0.5 V. (80nm × 80nm) (b) The protrusions inside the craters appear much brighter at higher negative sample bias. (c) and (d) indicate that the protrusions disappear at the positive sample bias. Min./Max. height difference: (a) 0.3nm, (b) 0.3nm, (c) 0.2nm, and (d) 0.1nm

50eV to 600eV could be detected with temperature program desorption (TPD).[33] However, we have been unable to detect an Ar peak in the XPS spectra of our MoS_2 samples even after extended 1 keV Ar^+ bombardment (total 3 hours). Therefore, we have concluded that the protrusions are not associated with implanted Ar atoms. Since initially implanted Ar^+ are most likely neutralized by electrons from the MoS_2 valence band, they will be chemically inert. We speculate that they are sufficiently mobile to diffuse into and out of the MoS_2 lattice within the time scale between Ar^+ bombardment and XPS analysis. The larger spaces between atoms in the MoS_2 lattice, when compared to the closely packed net of smaller carbon atoms in graphite, may account for the difficulty of Ar atom diffusion out of the graphite lattice.

To investigate the type B nanostructures [Figure 3. 5 (b)] in detail, bias dependent STM studies were performed. Figure 3. 6 shows a series of four STM images taken at various sample biases of an area (100 nm × 100 nm) that has been bombarded with a 1 keV Ar^+ ion beam. The image of the nanostructures taken at a - 0.1 V sample bias [Figure 3. 6 (a)] shows small bright areas inside the craters while the same areas appear much brighter in the image taken at a - 0.5 V sample bias [Figure 3. 6 (b)]. The bright features disappear at a + 0.1 V bias [Figure 3. 6 (c)] and as the sample bias is increased to + 0.5 V the apparent depth of the craters is reduced [Figure 3. 6 (d)].

We and others have previously demonstrated that dopant sites in semiconducting layered materials exhibit strong voltage dependent height changes when imaged with the STM since the dopants perturb the lateral density of states.[20,22,39,50] A sheet charge built up under an accumulation layer produced at the negative sample biases in n-type materials causes a high electrostatic force (EF) between the top most layer of the sample and the tip apex. This leads to an increase of the measured height since the soft MoS_2 layers are weakly bound to the subsurface layers and are pulled up towards the tip. Even stronger effects (height changes) at the step edges were explained by either additional charges localized on edge-site dangling bonds or the lower work function at the edge sites due to the presence of an additional surface dipole, causing a stronger EF than on the flat terrace.

Similarly, the most feasible interpretation of the height changes in Figure 3. 6 involves electronic effects induced by dangling bond states in the nanostructures. Ar^+ impacts on the MoS_2 surface could create near-surface sulfur or molybdenum atom vacancies producing dangling bonds inside the nanostructures. The dangling bonds can be localized charge traps since their energy levels are often located in the band gap of the semiconductor. These localized trap states can contain additional static charges that

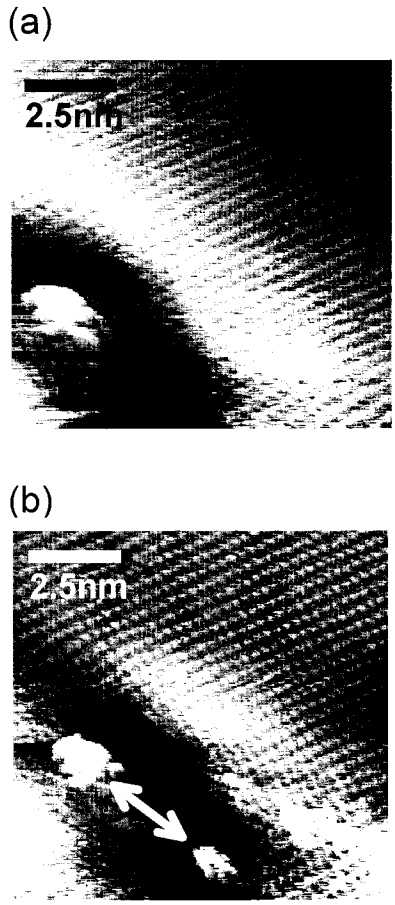

Figure 3. 7 (a) A type B nanostructure (10nm × 10nm). (b) The same nanostructure as (a) after 5 min of scanning the surface. The protrusion was separated into two parts by tip-sample interactions. The scanning conditions for all images are: sample bias = -0.1 V, tunneling current = 1.0 nA, scanning rate = 5 Hz and room temperature. Min./Max. height difference: (a) 0.6nm and (b) 0.5nm

induce strong EF interactions between the localized charges and their image charges at the tip apex in an accumulation condition (negative sample bias). This results in pulling up the surface. As a consequence, the feedback loop of STM retracts the tip from the surface in order to maintain constant tunneling current between the tip and sample, making that area of the sample appear as a protrusion.

Some of nanostructures could be influenced by repeated scanning of the STM tip. Even though this nanostructure appears as type B of Figure 3. 5 (b), their properties were quite different. Figure 3. 7 shows a nanostructure that was separated into two parts after 5 minutes of scanning the surface with a tungsten tip at the sample bias of -0.1 V and a current of 1.0 nA. The center of the nanostructures appear as a protrusion at all sample biases, unlike the nanostructures associated with electronic effects discussed previously [Figure 6]. The area of the original cluster is about 1.30 nm^2 representing about 12-18 atoms. The small cluster separated from the original by the action of the STM tip is about 0.24 nm^2 representing about 3-5 atoms. Sulfur or molybdenum atoms are the two possibilities for atoms sputtered from the substrate and redeposited onto the surface or pushed up onto the surface by a backscattered atom. Sulfur atoms are expected to have a high vapor pressure and so we expect that they would be pumped away in the UHV rather quickly. Mo atoms, on the other hand, have a low vapor pressure and are reactive enough

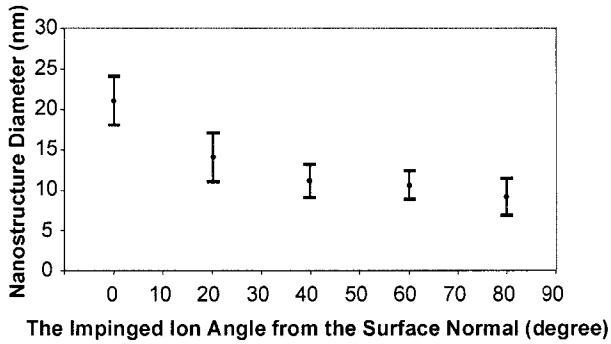

Figure 3. 8 The distribution of nanostructure diameters plotted as a function of incident angle for 1 keV Ar^+ bombardment. The incident angle is defined as an angle of the impinged Ar^+ from the surface normal.

to chemically interact with the MoS_2 van der Waals surface and/or with some sputtered sulfur atoms to form a cluster on the surface. We then associate these nanostructures with ad-atom clusters of Mo and S that are bound weakly enough to the MoS_2 surface to be influenced by the interaction with the STM tip.

One of the goals of these studies is to selectively remove surface sulfur atoms to investigate the catalytic reactivity of the vacant surface sites for HDS. Low angle ion sputtering is believed to confine the sputtering effects to the near surface region. Therefore, we investigated the effects of the incident Ar^+ beam angle on the produced nanostructures. Figure 3. 8 shows the measured diameters of nanostructures from impinged 1 keV Ar^+ as a function of the incident angle in the range between 0° and 80° degree (0 ° is defined as surface normal). The vertical bars indicate the standard deviations of the diameters of the nanostructures. The diameter of nanostructures decreased with angle between 0° and about 40°, whereas above 40° it remained relatively constant at about 9 nm. This trend is similar to what was observed for graphite where, with 1.5 keV Ar^+ bombardment, the diameters of the bumps decreased (10%) and the heights were increased (82%) with incident ion angles from 0° to 70° since the energy transfer of the impinged ions is confined to the near surface region.[34,35] We also observed that the higher angle ion sputtering with the same ion energy increases the proportion of

Type B nanostructures (more than 90% at 60^0) with respect to Type A. These results confirm that higher angle ion sputtering does induce more near surface damage.

Nanostructure fabrication by He^+ bombardments on MoS_2

We also performed He^+ sputtering of MoS_2 to investigate whether single sulfur atom vacancies could be fabricated more reproducibly with a higher yield using a lighter ion. Figure 3. 2 (b) also shows the distribution of nanostructure diameters as a function of He^+ energy at normal incidence. 500 eV and 1 keV He^+ produced nanostructures with average diameters of 5.8 ± 1.0 nm and 9.1 ± 2.1 nm, respectively, whereas Ar^+ sputtering with the same energies produced larger diameters of 10.7 ± 2.6 nm and 21.1 ± 3.0 nm. The smaller nanostructures from He^+ sputtering may be related to the lower atomic mass of He^+ since the momentum of a He^+ is about three times less than that of an Ar^+ at the same ion energy. Atomic scale STM investigations of the nanostructures showed that 500 eV He^+ sputtering produced depressions but not protrusions that are similar to the shape of nanostructure seen in 100eV Ar^+ sputtering [Figure 3. 3]. The atomic order of the sulfur lattice is also preserved inside the nanostructures. These results suggest that 500 eV He^+ sputtering does not effectively remove sulfur atoms from the surface, however it can induce damage to the near surface region.

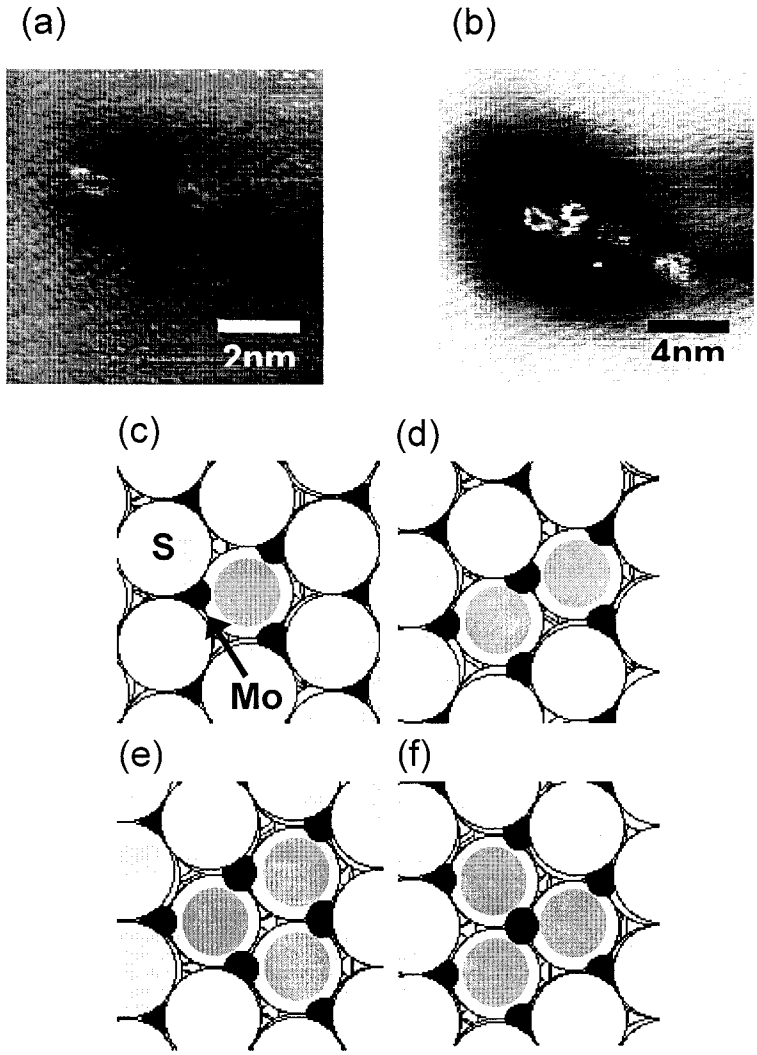

Figure 9. (a) STM image of a nanostructure produced by 750 eV He^+ sputtering of MoS_2. Three ring shape features could be seen inside the nanostructure. The average diameter of the rings was determined to be 0.33 nm. (b) STM image of a nanostructure produced by 1 keV He^+ sputtering of MoS_2. The average diameter of the rings was determined to be 0.68nm. (c) Model of a single sulfur atom vacancy. Black and grey circles indicate Mo and sulfur atoms, respectively. Three Mo atoms are partially exposed below the basal plane. (d) Model of two-sulfur atom vacancy. Five Mo atoms are partially exposed below the basal plane. (e) and (f) Models of three-sulfur atom vacancy with two possible geometries. Six and seven Mo atoms, respectively, are partially exposed below the basal plane.

He^+ with energies greater than 500 eV begin to produce nanostructures with bright areas like those seen in Figure 3. 5 for Ar^+ (Type A and B nanostructures), as well as new types of features. Figure 3. 9 (a) shows an STM image of nanostructures produced by 750 eV He^+ sputtering where bright ring shapes were observed inside the nanostructure. The elongated ring shape is a result of thermal drift in the STM since only a background plane fit was applied to this image. The average apparent height and diameter of the ring were determined to be about 0.15 nm and 0.33 nm.

A single sulfur atom vacancy on a MoS_2 basal plane [Figure 3. 9 (c)] will have a diameter equal to the unit cell distance (0.316nm), very close to the measured diameter of the nanostructure in Figure 3. 9 (a) (0.33 nm). Therefore, the ring-shaped bright areas can be associated with a single sulfur atom vacancy. Removal of a surface sulfur atom exposes a dangling bond from three, now five-coordinate, Mo atoms on the metal layer below. The dangling bond states have energies in the band gap of MoS_2 making them appear bright at certain STM imaging biases and not imaged at all at other biases, much like the electronic defects discussed earlier. The bright ring shapes associated with the S atom vacancy do disappear at positive sample biases, supporting our claim that they are associated with the dangling bond states of the sub-surface Mo atoms. Another interesting observation is that most of the nanostructures contain more than one bright

ring shape. A possible explanation of these multiple bright rings in the nanostructures is that they result from collision cascade processes where the impinging He^+ imparts energy to several other atoms that then eventually eject a surface S atom near the original impact site.

Figure 3. 9 (b) shows a nanostructure produced by a 1 keV He^+ impact on the MoS_2 surface. Two bright ring shapes can be seen inside the nanostructure along with several other less bright features. The brighter features appear to be triangles with an average diameter of about 0.68 nm, about twice the diameter of the ring shaped structures produced by 750 eV He^+ sputtering in Figure 3. 9 (a). These bright ring shapes may be related to multiple sulfur atom vacancies as modeled in Figure 3. 9 (d) - (f). A two-sulfur atom vacancy is illustrated in Figure 3. 9 (d) where five Mo atoms with incomplete coordination (dangling bond states) are partially exposed. Figure 3. 9 (e) and (f) show the two possible geometries for a three-sulfur atom vacancy where six and seven Mo atoms, respectively, are partially exposed. We speculate that the triangular structures in Figure 3. 9 (b) may be three-sulfur atom vacancies with six exposed Mo atoms [Figure 3. 9 (e)]. We favor the triangular structure in Figure 3. 9 (e) since there is no bright central feature evident in the STM images that would be associated with the exposed three-coordinate

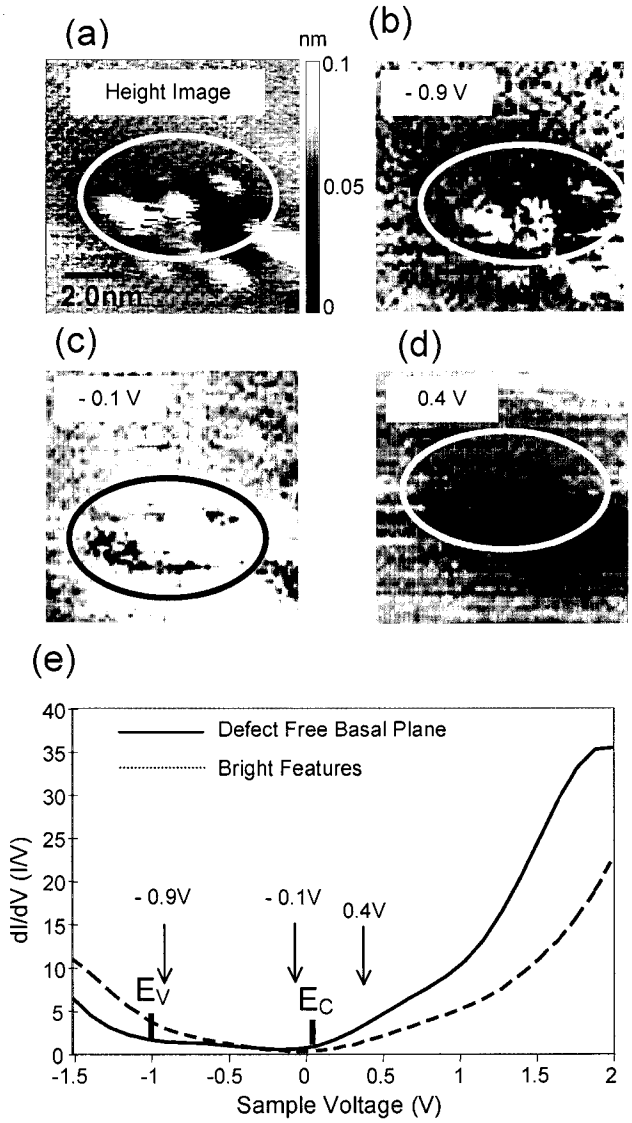

Figure 3. 10 Constant current STM image, 2-D current maps, and differential conductance curves (dI/dV) of a nanostructure with bright features on MoS_2. (a) Constant current STM image of a nanostructure (8nm × 8nm). The scanning conditions for this image are: sample bias = -0.5V, tunneling current = 1.0 nA, and scanning rate = 5 Hz, and room temperature. (b) ~ (d) 2-D current maps of the same nanostructure for the tunneling current measured from CITS at (b) – 0.9V, (c) – 0.1V, and (d) 0.4V (sample bias). These 2-D current maps were taken simultaneously with the STM image displayed in Figure 9 (a) and the tip and sample distance was stabilized at the tunneling conditions for the constant current STM image. (e) Comparison of differential conductance (dI/dV) curves of bright features and basal plane of MoS_2.

Mo atom. We also believe that this low coordination is unstable whereas the four-coordinate edge sites of Figure 3. 9 (e) are more stable.

Current imaging tunneling spectroscopy (CITS) studies of nanostructures with bright features

To obtain detailed electronic information of these bright ring shape features, current imaging tunneling spectroscopy (CITS) measurements were performed on nanostructures with bright features produced by 750eV He^+ bombardments. A constant current STM image along with CITS data are shown in Figure 3. 10. Figure 3. 10 (a) shows the constant current STM image while Figure 3. 10 (b) ~ (d) indicate 2-D current maps at sample bias of (b) – 0.9V, (c) – 0.1V, and (d) 0.4V. Figure 3. 10 (e) shows scanning tunneling spectroscopy (STS) data of both basal plane and bright features obtained from CITS measurements where more than 100 I/V curves in each region were averaged. The constant current image (8×8 nm^2) [Figure 3. 10 (a)] shows several bright features in the nanostructure (indicated by the circle) and was taken simultaneously with the 2-D maps. The CITS images do not show an atomic scale resolution due to the thermal drift that occurs over the time scale of these measurements (15minutes).

The bright features are more clearly distinguished in the 2-D current maps at selected voltages [Figure 3. 10 (b) ~ (d)]. At – 0.9V sample bias [Figure 3. 10 (b)], the bright features could be observed whereas other areas in nanostructure appear as a depressions i.e. reduced current. However, as the sample bias is decreased, the bright features become less prominent. The feature is no longer imaged at the sample bias of – 0.4 V. At sample bias less than –0.4 V, a contrast reversal is observed. Figure 3. 10 (c) is a 2-D current map of the same area with a sample bias of – 0.1 V where the protrusions and depressions in Figure 3. 10 (a) are reversed. At the positive sample bias of 0.4V, the image contrast was low and the bright features are not imaged [Figure 3. 10 (d)].

The contrast changes can be explained by comparing the constant current image with characteristic STS spectra. Figure 3. 10 (e) shows differential conductance (dI/dV) spectra of the defect free basal plane of MoS_2 and the bright features. The spectrum of the basal plane reveals that the electrons predominantly tunnel out of valence band (occupied) states at sample biases more negative than – 1.0 V and tunnel into conduction band (unoccupied) states at sample biases more positive than 0.1V. These bands are separated by a gap of ~1.1 eV, quite close to bulk band gap of MoS_2 (1.2eV).[49] The Fermi level (E_F) is located close to E_C due to the n-type doping of this sample. At negative sample biases (greater than –0.4 V), the STS curve of bright features shows a

higher differential conductance (dI/dV) than the defect free basal plane, whereas at negative sample biases (less than –0.4 V) and positive sample biases, the differential conductance of the bright features is reduced. These conductance changes at the bright features are most likely caused by E_F shift toward the valence band (~0.7 eV) when compared with defect free basal plane. [Figure 3. 10(e)] As discussed earlier, the impinged He^+ ion creates sulfur atomic vacancies that appear as bright features at negative sample biases. These bright features were associated with p-type dopant states as judged by their contrast dependence on STM imaging bias. These p-type energy states induce the E_F shift (~ 0.7 eV) toward the valence band. This E_F shift in STS data corresponds well to our previous XPS results where individual ion bombardments induced E_F shift of MoS_2 (~ 0.7 eV) to lower binding energy due to a change of surface doping density. Therefore, we believe that He^+ sputtering of the MoS_2 sample with the energies greater than 500eV produces sulfur atom vacancies (dangling bond states associated with sub-surface Mo atoms). These vacancies contain altered local densities of electronic states, resulting in the E_F shift of MoS_2 toward the valence band. The altered electronic states make them appear as bright features at sample biases more negative than –0.4 V.

An important aspect from the above results is that CITS measurements represent the localized electronic states of the individual sulfur atomic vacancies whereas XPS measurements are sensitive to global energy states of Ar^+ bombarded MoS_2 surface. Even though there is a similar trend in the XPS and CITS results, the collective energy states of Ar^+ bombarded MoS_2 surface may differ from the individual energy states of sulfur atomic vacancies due to contributions from other areas of the surface in the XPS measurement..

When only a few sulfur atomic vacancies exist on the MoS_2 surface, we can be confident that charge transport or delocalization does not take place within energy levels of the sulfur atomic vacancies since sulfur atomic vacancies are so widely spaced throughout the sample surface. However, if we continue to increase the number of sulfur atomic vacancies, thus p-type doping density, a point is reached where the sulfur atomic vacancies become so closely packed within the surface lattice that interactions between them cannot be ignored. For example, sulfur atomic vacancies present in high concentrations are so close together that we can no longer consider the energy level of the individual sulfur atomic vacancies as being composed of discrete and non-interacting energy states. Instead, sulfur atomic vacancies form a band, which may overlap the top of the valence band due to their p-type characteristics. When the hole concentration of p-

type sulfur atomic vacancies of valence band exceeds the effective density of states, the Fermi level is no longer within the gap but lies within the valance band (degenerate p-type states). Thus, we speculate that at the low density of sulfur atomic vacancies we can ignore charge transport or delocalization between vacancies whereas the delocalization will play an important role at the high density of vacancies.

Our group has previously demonstrated that STM[51] and atomic force microscopy (AFM)[52] can be used to etch off individual layers from the surface of two-dimensional materials (i.e. $SnSe_2$, $TiSe_2$, and $NbSe_2$). Other groups have also observed similar phenomena in WSe_2[53,54], HgI_2[55] and TaS_2[56]. Our model to explain the etching starts with chalcogenide atom vacancies acting as the nucleation sites with subsequent material being removed according to the number of nearest neighbor coordination sites. A model that made four coordinate sites stable produced triangular nucleation sites that continued to grow as triangular features. In our experimental results, the triangular structures in Figure 3. 9 (b) may have grown from STM scanning of the single atom vacancies produced by He^+ sputtering of the surface of MoS_2. We think that removal of three adjacent S atoms from a single low energy He^+ impact will be very unlikely.

3. 4 CONCLUSIONS

Ar^+ bombardments with energies of 100 eV or less showed a low yield for removing sulfur atoms from the surface. Sub-surface ion-atom collisions can break sub-surface Mo-S bonds and create features that, due to electronic effects, appear as depressions in the STM images. Ar^+ ions with energies greater than 100 eV can create S atom vacancies with much higher efficiency, thus producing craters (pits) and protrusions on the surface. These protrusions can be redeposited atoms, deformation of the lattice structures, or electronic effects of dangling bond states of sulfur atomic vacancies in the nanostructures. With ion energies of more than 1keV, the ions would have a short residence time near the surface and lose energy as they penetrate deeper into the lattice.

He^+ sputtering of MoS_2 showed similar trends in nanostructure fabrication to Ar^+ sputtering. However, it produced smaller nanostructures when compared to Ar^+ at the same ion energy. He^+ with the energy of 500eV or less produced mostly dent-like structures with a low yield of sulfur atom detachments. At the energies greater than 500eV, He^+ creates sulfur atom vacancies with higher efficiency. 750 eV He^+ sputtering of MoS_2 generate single sulfur atom vacancies whereas three sulfur atomic vacancies are produced with higher efficiency by 1 keV He^+ sputtering. These vacancies appear in STM images as bright ring and triangular shapes, respectively, with the negative sample bias

greater than –0.4V. CITS analysis shows that these bright features can be attributed to the altered local density of states due to the E_F shift to the valence bands.

REFERENCES

[1] M. G. Youngquist and J. D. Baldeschwieler, J. Vac. Sci. Technol. B **9,** 1083-1087 (1991).

[2] M. Weimer, J. Kramer, C. Bai, and J. D. Baldeschwieler, Phys. Rev. B **37,** 4292-4295 (1988).

[3] R. R. Chianelli, Catal. Rev. -Sci. Eng. **34,** 361-393 (1984).

[4] A. N. Startsev, Catal. Rev. -Sci. Eng. **37,** 352-423 (1995).

[5] R. Prins, H. J. De Bear, and G. A. Somorjai, Catal. Rev. -Sci. Eng. **31,** 1-41 (1989).

[6] F. Pedraza, S. Fuentes, M. Vrinat, and M. Lacroix, Catal. Lett. (1999).

[7] Y. Araki, K. Honna, and H. Shimada, J. Catal. **207,** 361-370 (2002).

[8] S. Helveg, J. V. Lauritsen, E. Lagsraard, I. Stensgaard, J. K. Norskov, B. S. Clausen, H. Topsoe, and F. Besenbacher, Phys. Rev. Lett. **84,** 951-954 (2000).

[9] M. Daage and R. R. Chianneli, J. Catal. **149,** 414-427 (1994).

[10] J. V. Lauritsen, S. Helveg, E. Lagsraard, I. Stensgaard, B. S. Clausen, H. Topsoe, and F. Besenbacher, 197, 1-5 (2001).

[11] M. V. Bollinger, J. V. Lauritsen, K. W. Jacobsen, J. K. Norskov, S. Helveg, and F. Besenbacher, Phys. Rev. Lett. **87,** 196803 (2001).

[12] S. L. Peterson and K. H. Schulz, Langmuir **12,** 941-945 (1996).

[13] C. G. Weigenstein and K. H. Schulz, J. phys. Chem. B **103,** 6913-6918 (1999).

[14] J. Moser, F. Levy, and J. Bussy, J. Vac. Sci. Technol. A **12,** 221 (1994).

[15] T. Spalvins, J. Vac. Sci. Technol. A **5,** 494 (1987).

[16] X. Chu and L. D. Schmidt, J. Catal. **144,** 77-93 (1993).

[17] S. N. Magnov, H.-J. Cantow, and M.-H. Whangbo, Surf. Sci. **318,** L1175-L1180 (1994).

[18] J. S. Ha, H. S. Roh, S. J. Park, J. Y. Yi, and E. H. Lee, Surf. Sci. **315,** 62-68 (1994).

[19] H. Permana, S. Lee, and K. Y. Simon Ng, J. Vac. Sci. Technol. B **10,** 2297-2301 (1992).

[20] T. W. Matthes, C. Sommerhalter, A. Rettenberger, P. Bruker, J. Boneberg, M. C. Lux-Stainer, and P. Leiderer, Appl. Phys. A **66,** S1007-S1011 (1998).

[21] C. Sommerhalter, T. W. Matthes, J. Boneberg, M. Lux-Steiner, and P. Leiderer, Appl. Surf. Sci. **144-145,** 564-569 (1999).

[22] R. Schlaf, D. Louder, M. W. Nelson, and B. A. Parkinson, J. Vac. Sci. Technol. A **15,** 1466-1472 (1997).

[23] M.-H. Whangbo, J. Ren, S. N. Magnov, H. Bengel, B. A. Parkinson, and S. A., Surf. Sci. **326,** 311-326 (1995).

[24] J. G. Kushmerick, S. A. Kandel, P. Han, J. A. Johnson, and P. S. Weiss, J. Phys. Chem. B **104,** 2908-2988 (2000).

[25] H. Murata, K. Kataoka, and A. Koma, Surf. Sci. **478,** 131-144 (2001).

[26] M. H. Farias, A. J. Gellman, S. G. A., R. R. Chianelli, and K. S. Liang, Surf. Sci. **140,** 181-196 (1984).

[27] T. Schimmel, H. Fucus, K. Graf, R. Sander, and M. Lux-Steiner, Phys. Sat. Sol. **131,** 89-98 (1992).

[28] M. A. Baker, R. Gilmore, C. Lenardi, and W. Gissler, Appl. Surf. Sci. **150,** 255-262 (1999).

[29] N. Sengoku and K. Ogawa, Jpn. J. Appl. Phys. **34,** 3363-3367 (1995).

[30] J. R. Hahn, H. Kang, S. Song, and I. C. Jeon, Phys. Rev. B **53,** R1725-R1728 (1996).

[31] H. Kang, K. H. Park, C. Kim, B. S. Shin, C. Kim, and D. W. Moon, Nucl. Instrum. Methods B **67,** 312-315 (1992).

[32] D. Marton, H. Bu, K. J. Boyd, S. S. Todorov, A. H. Al-Bayati, and J. W. Rabalais, Surf. Sci. **326,** L489-L493 (1995).

[33] W. Choi, C. Kim, and H. Kang, Surf. Sci. **281,** 323-335 (1993).

[34] Q. Yang, T. Li, B. V. King, and R. J. MacDonald, Phys. Rev. B **53,** 3032-3038 (1996).

[35] T. Li, B. V. King, R. J. MacDonald, G. F. Coterill, D. J. O'Connor, and Q. Yang, Surf. Sci. **312,** 399-410 (1994).

[36] H. J. Steffen, D. Marton, and J. W. Rabalais, Phys. Rev. Lett. **68,** 1726 (1992).

[37] D. Marton, K. J. Boyd, T. Lytle, and J. W. Rabalais, Phys. Rev. B **48,** 6757-6766 (1993).

[38] H. J. Steffen, C. D. Roux, D. Marton, and J. W. Rabalais, Phys. Rev. B **44,** 3981-3990 (1991).

[39] D. Louder, Thesis, Colorado State University, 1996.

[40] G. M. Shedd and P. E. Russell, J. Vac. Sci. Technol. A **9,** 1261-1264 (1991).

[41] *Sputtering by particle bombardment I*; *Vol. 47*, edited by R. Behrisch (Springer_Verlag, New York, 1981).

[42] J. W. Rabalais, *Principle and Applications of Ion Scattering Spectroscopy* (Wiley-Interscience, 2003).

[43] M. V. Ramana Murty, Surf. Sci. **500,** 523-544 (2002).

[44] http://www.srim.org/

[45] C. A. Lang, C. F. Quate, and J. Nogami, Appl. Phys. Lett. **59,** 1696-1698 (1991).

[46] S. N. Magonov and M.-H. Whangbo, *Surface Analysis with STM and AFM* (VCH, Weinheim, 1996).

[47] J. R. Lince, D. J. Carre, and P. D. Fleischauer, Langmuir **2,** 805-808 (1986).

[48] The STM images show that 100 eV Ar^+ bombardments of MoS_2 sample produce 27 nanostructures/μm^2sec. If it is assumed that the nanostructures in the top three layers of MoS_2 sample are only imaged by STM (the lattice distance c is 0.64 nm), the surface density of defects created by 100 eV Ar^+ sputtering for 5 minutes is about 4.2×10^{18} cm^{-3}.

[49] K. K. Kam and B. A. Parkinson, J. Phys. Chem. **86,** 463 (1982).

[50] R. Schlaf, P. G. Schroeder, M. W. Nelson, R. Stubner, S. Tiefenbacher, H. Jungblut, and B. A. Parkinson, Thin Solid Films **331,** 203-209 (1998).

[51] B. A. Parkinson, J. Am. Chem. Soc. **112,** 7498-7502 (1990).

[52] E. Delawski and B. A. Parkinson, J. Am. Chem. Soc. **114,** 1661-1667 (1992).

[53] J. Boneberg, M. Lohrmann, M. Bohmisch, F. Burmeister, M. Lux-Stainer, and P. Leiderer, Z. Phys. B **99,** 567-570 (1996).

[54] S. Akari, R. Moller, and K. Dransfeld, Appl. Phys. Lett. **59,** 243-245 (1991).

[55] H. P. Lang, A. Rossberg, M. Piechotka, and E. Kaldis, J. Crystal Growth **144,** 371-374 (1994).

[56] W. Yamaguchi, O. Shiino, H. Sugawara, T. Hasegawa, and K. Kitazawa, Appl. Surf. Sci. **119,** 67-75 (1997).

Conclusions and Future work

We have fabricated nanostructures on MoS_2 and $MoTe_2$ surface by bombarding them with Ar^+ and He^+ with energies ranging from 100 eV to 5 keV and with voltage pulses from a tip of scanning tunneling microscope (STM) in an ultrahigh vacuum environment. In the case of Ar^+ sputtering of MoS_2, Ar^+ with energies of 100 eV or less remove very few sulfur atoms from the surface, but x-ray photoemission spectroscopy (XPS) studies reveal that the electronic structure of the MoS_2 surface is altered. Ar^+ ions with energies greater than 100 eV have a higher probability of sputtering sulfur atoms from the surface. Two types of nanostructures were commonly observed with this energy region. The type A nanostructure has a central crater surrounded by protrusions (hillocks) whereas the type B nanostrucutre has the protrusion inside the crater. With ion energies of more than 1 keV, ion implantation becomes a more probable process, resulting in a small decrease of nanostructure size due to more energy dissipation deeper in the crystal.

He^+ sputtering of MoS_2 showed similar trends in nanostructure fabrication to Ar^+ sputtering, but produced smaller nanostructures when compared to Ar^+ at the same ion energy. He^+ with the energy of 500eV or less produced mostly dent-like structures with a low yield of sulfur atom detachment from the surface whereas at the energies greater than 500eV, He^+ begins to produce sulfur atomic vacancies with higher efficiency. He^+ with

an energy of 750eV selectively removed 1 ~ 3 sulfur atoms per ion. These vacancies appear in STM images as bright rings or triangular shapes at a negative sample bias. Current imaging tunneling spectroscopy (CITS) showed that these bright features are attributed to an altered local density of states due to a shift in E_F towards the valence band and thus are associated with the exposed Mo atoms below the basal plane.

We have also used the STM to generate atomic scale nanostructures on $MoTe_2$ and MoS_2 surfaces by applying voltage pulses between the tip and sample. There exist distinct threshold voltages for surface modification of $MoTe_2$ and MoS_2 surfaces, 3.0 ± 0.3V and 3.4 ± 0.3V, respectively, whereas the current and pulse duration did not show any correlation with the size of the nanostructures. It was found that the geometry of STM tips (tip sharpness and shape) plays an important role in nanostructure fabrication. A tip with apex radius less than 10nm may be able to reproducibly generate atomic scale vacant sites. The positive voltage pulses applied to p-type $MoTe_2$ selectively removed only tellurium atoms from the basal plane whereas negative voltage pulses removed more than one complete layer. This pulse polarity dependence of nanostructure fabrication was explained by the difference of the magnitude of applied electric fields.

We have generated and investigated the nanostructures on $MoTe_2$ and MoS_2 surfaces in order to produce individual catalytic sites (exposed Mo atoms) for atomic

scale investigation of hydrodesulfurization (HDS) reaction. Thus, the next step in this research will be to investigate the catalytic reactivity of these nanostructures by exposing sulfur containing compounds to the nanostructured MoS_2 surface. A possible molecule is 1-pentanethiol since it has a combination of high vapor pressure at room temperature and a long enough hydrocarbon chain to make it obvious in the STM image. The chain length can be easily varied to optimize vapor pressure and imaging since these alkyl thiols are commercially available. We may need to use the low temperature facility of our variable temperature STM (VT-STM) to cool the substrate, thus facilitating adsorption of the thiol molecules to the catalyst surface. We have tested the low temperature STM using liquid nitrogen (77K), and obtained quite stable atomic scale images of nanostructures (extremely low thermal drift). The variable temperature capability will also be used to determine the activation barriers for the various HDS reactions.

He^+ bombardments allow for controlled production of sulfur atomic vacancies with a variety of sizes and shapes. For example, 750 eV He^+ sputtering of MoS_2 produces single sulfur atomic vacancies with three partially exposed Mo atoms whereas 1 keV He^+ sputtering generates three sulfur atomic vacancies with six or seven exposed Mo atoms [Figure 3. 9 (c) ~ (f)]. This controlled production of sulfur atomic vacancies implies the preparation of a specific geometry of catalytic sites for HDS reactions. In one geometry

[Figure 3. 9 (f)] the three sulfur atoms above a single Mo atom have been removed, allowing for possible adsorption of a thiol's sulfur atom to the d_z^2 orbital of centrally exposed Mo atom. During the adsorption process the thiol eliminates hydrogen which should associate with a nearby unsaturated sulfur atom at the edge of the vacancies forming an S-H termination. In the case of the other three atom vacancy [Figure 3. 9 (e)], the sulfur atom of the thiol might bind to a threefold Mo site with the H atom again bound as a terminal SH moity. There may be significant reactivity differences between these two types of threefold sites. We intend to investigate differences in threefold site reactivity as well as reactivity of single sulfur atomic vacancies and larger vacancy sites where four or more sulfur atoms have been removed.

Once sulfur containing compounds are bound to catalytic sites, small amounts of H_2 gas will be admitted to the chamber with the same dosing system, so that the adsorbed molecules will react with H_2 gas. Two possible routes for the hydrogenolysis reaction are then possible. Hydrogen can dissociatively adsorb to dangling sulfur bonds in nanostructures created by removal of a sulfur atom from the surface. Alternatively, the H_2 can dissociate on the STM tip especially if a Pt or Pt-Ir tip is used. Either way the activated hydrogen will then be available to continue the HDS of the adsorbed thiol, resulting in desorption of alkane and H_2S, or the plugging of the catalytic site by the

sulfur left behind when the alkane desorbs. Distinguishing between these mechanisms should be possible from the resulting STM images.

Edge planes have also been implicated as active sites for HDS catalysis. HDS studies at edges are not widely reported since it is difficult to reproducibly create high-index, well-defined step edges on single-crystal MoS_2 surfaces. We can, however, prepare oriented edge planes on a very small scale by applying negative voltage pulses [Figure 2. 8] where one van der Waals layer thick etched pits are created on the basal plane. We will investigate the edge reactivity using similar technique described above. First we will create etch pits of a controlled size by adjusting a voltage pulse height. This will be followed by dosing the surface with thiol compounds and observation of the molecular orientation relative to the edge using the STM. Observation of reactivities and orientations of thiols would give us valuable information related to the HDS mechanism when compared with the vacancies of basal plane.

Industrial HDS catalysts contain Co and/or Ni as activity promoters. The actual role of these promoters in the HDS catalysis still remains unknown. We have shown that it is possible to image impurity atoms in the first few surface layers of TMD's by STM imaging [Figure 1. 2. 5]. Investigating the different morphologies and electronic structures of promoters such as Co and Ni on MoS_2 catalysts using both STM and

scanning tunneling spectroscopy (STS) will give us insight into their role in HDS reactions. Localized electron density variations resulting from the added promoters can be imaged. If the local density of states (DOS) of pure vacant sites with Co and Ni promoted vacant sites are compared, it would provide information about the arrangement of promoters at the active sites and the reactivity of sulfur compounds in the vicinity of promoter atoms.

When are observed single catalytic events using the simplified alkane thiol model, work will be extended to many of the more common model reactant molecules such as thiophene, benzothiophene or dibenzothiophene. These systems will be more difficult to study since they involve many more reaction steps than the alkane thiols. The size of the binding site required for HDS catalysis of these larger molecules is currently unknown. Varying the size and shape of the surface vacancies using STM voltage pulse technique or He^+ sputtering with different ion energies will allow us to examine how these more bulky molecules fit into different types of active sites. At the same time, experiments with other metal dichalcogenide substrates such as WS_2 and WSe_2 can be done in order to investigate their catalytic reactivities and sizes of the binding site required for HDS process. The removal of Se atoms from WSe_2 will result in larger holes (lattice constant

for WSe_2 a = 0.328 nm while for MoS_2 a = 0.316 nm) providing more space for substrate molecules to bind.

Research Proposal

A Systemic Investigation of Potential Induced Phase Transition and Orientation of Organic Adsorbates at the Gas-Solid Interface

A Proposal Submitted as a Degree Requirement
for the Chemistry Doctoral Work at Colorado State University

Joon Bum Park
Department of Chemistry
Colorado State University
Fort Collins, Colorado 80521

Abstract

Organic monolayers are interesting due to their broad range of applications from device technology to biology as well as their importance as a nice model system for studying two-dimensional phenomena such as phase transition and molecular orientation. Understanding of surface phenomena of organic adsorbates and developments of thermodynamically stable organic adlayers should be necessary for the future organic device technology. Even though several potential induced phase transitions and orientations have been studied recently, the direct observation of intermolecular interactions at the gas-solid interface has not succeeded. We propose to systematically investigate potential induced

intermolecular interactions and phase transitions using properly functionalized molecules at gas-solid interface. The objectives of this proposal include identification of stable adsorbates, kinetic analysis of adsorbates, and investigation of molecular interactions depending on the polarity and magnitude of the applied electrostatic field. An overall research plan is described to fabricate islands of dielectric materials as a supporter of electric fields, supply potentials to them via scanning tunneling microscopy (STM) voltage pulses, and monitor the whole process of molecular interactions using *in situ* STM.

Background

Organic thin films are attractive due to their broad applications ranging from transistor and organic light emitting diodes (LEDs) to photo-detectors and chemical sensors.[1-10] Precise control of organic molecular structures would be essential for the future mass fabrication of nanoscale devices. However, controlled assembly of individual molecules demands fundamental understanding of the roles of molecule-molecule and molecule-substrate interactions as well as surface phenomena such as phase transition and surface diffusion. Controlling of organic molecules by potential induced phase transitions and reorientation would facilitate development of new device technology. Even though several studies related to these subjects have been performed, direct measurements of individual molecular surface interactions and orientation at the gas-solid interphase have not yet succeeded.[6,7,11-13] Another requirement for reliable device fabrication is that most nano-scale organic structures are formed as meta-stable states during nucleation and growth, and their stability has been a limiting factor to prepare

reproducible organic layers. The development of thermodynamically stable nanostructures would be a promising approach for the future mass fabrication of nanoscale structures.

The first molecular scale study of a surface charge induced order-disorder transition was performed in a 2-2' bipyridine (22BPY) monolayer at the solid-liquid interface using EC-STM (electrochemical scanning tunneling microscopy).[12] At a positive sample bias, the planar molecules stand vertically on the surface and form a linear chain where two nitrogen atoms are facing the Au (111) surface. Decreasing charge density below critical value leads the molecular chain to be randomly disoriented on the surface and this transition is fully reversible. The transition from disordered to ordered phase starts by forming small ordered domains that quickly increase in number and coalesce into larger domains. The reverse transition occurs as new domains form within old domains, resulting in smaller domains that eventually lead to the disordered phase. This phase transition was explained by analogy to the isotropic-nematic transition

of liquid crystals in three dimensions.[12,14] Further investigation of this transition was attempted using 4-4' bipyridine (44BPY) on Au (111) system.[13] The driving force of phase transition reveals a potential dependent attractive force between the ordered chains. The attractive force is considered as a substrate mediated effective force, which arises as an adsorbed 22BPY perturbs its surrounding local surface potential (neighboring molecules).

Recently, it has been reported that 5, 10, 15, 20-tetra(4-pyridyl)-21H, 23H-porphirine (TyTP) forms ordered or disorderd structures at the Au (111) / 0.1M H_2SO_4 solution interface, depending on the Au electrode potential where the molecules self-assemble.[11] These results were explained by the role of potential induced molecule-substrate interaction (binding energy) and surface mobility. At positive bias (> 0.5V vs SEC), a disordered layer is formed due to the strong molecule-substrate interaction (low surface mobility), preventing surface diffusion for ordered layers. At negative sample bias (< -0.2V), the molecules are highly mobile and could not be imaged by STM.

However, intermediate potentials (-0.2 ~ -0.5V) provide highly ordered TyTP adlayers due to the moderate surface mobility and molecule-substrate interaction. These results suggest that by tuning the electrode potential, one can control the mobility of molecules on the surface and ultimately the self-assembled process.

On the other hand, self-assembly of thermodynamically stable nanostructures from appropriate funtionalized molecules has been attempted.[15-17] Bohringer and co-worker demonstrated energetically stable self-assembled adlayers of dipolar organic molecule 1-nitronaphthalene (NN) on a Au(111) surface using low temperature STM under ultra high vacuum.[15-17] NN molecules lie flat on the surface, which is typical for planar aromatic molecules keeping the π electron system parallel to the substrate surface. Low coverage deposition of NN molecules produced "magic two dimensional supramolecular cluster" which are mainly formed within the fcc domain of reconstructed Au (111) surface. These clusters are predominantly composed of ten molecules (decamer) and resemble "pinwheel" structures with eight-molecule ring surrounding a

two-molecule core. The formation of decamers was attributed to specific intramolecular interactions of NN molecules. Tip manipulation experiments showed that the decamers behaved like stable supramolecules where the complete decamers moved laterally without a change in internal structures. At monolayer coverage, stable self-assembly of N molecules are arranged in a head to tail orientation by hydrogen bonding between negatively charged oxygen atom and hydrogen atom (C4) on the naphthalene group of adjacent molecules.

All of these studies are of fundamental importance in that potential induced phase transitions are achievable to aid in fabrication of ordered arrays of organic adsorbates and thermodynamically stable layers can be prepared from appropriately funtionalized molecules. However, they still fail to provide a comprehensive understanding of the rules for the phase transition and molecular interactions. The biggest dilemma to the previous phase transition study is that all the experiments were performed in liquid phase. The approach for the transition and orientation in gas-solid interface

would be more promising to understand direct molecules-substrate and/or molecule-molecule interactions due to the nonexistence of intermediary phase such as solvent. Here, this proposed research is aimed at the fundamental study of organic molecules at the solid-gas interface related to their orientation and transition, and production of energetically stable organic adlayers from molecular interactions of dipolar molecules. These studies would provide invaluable information toward designing molecular system and the thin film development of molecular based technological devices.

Research Design

System design

To attempt to investigate potential induced phase transition and molecular orientation at the gas-solid interface, we will utilize dielectric materials as an applied potential source to the molecules [Figure 1]. A dielectric material is a substance with poor electrical conductivity, but that can efficiently support an electric field.[18] If the flow

of current to the dielectric material is interrupted or impeded, the dielectric material can store the applied electrostatic field. The proportionality constant between the applied voltage and the stored charge is called the capacitance (C) through the relationship $C=\varepsilon_r\varepsilon_0$ A/L where A and L are surface area and thickness of dielectric materials, and ε_r and ε_0 is the dielectric constant and the permittivity, respectively. In this study, the islands of dielectric materials such as Si_3N_4 (ε_0=7.5), Al_2O_3 (10.95), or SiO_2 (3.9) will be used as supporter of electric field and the electric field will be provided by an STM tip voltage pulse. As a first step, Au will be evaporated onto the mica substrate using knudsen cell. From the repeated cycles of sputtering and annealing (600K) in high vacuum environment, the reconstructed Au(111) surface with wide and flat terrace will be prepared. Other metals such as Ag, Cu, and Al will be also available for this study. For the fabrication of the islands of dielectric materials, small amount of Si_3N_4 will be deposited on the metal surface from PVD (Physical Vapor Deposition). Al_2O_3 and SiO_2 can be prepared by depositing Al and Si islands followed by thermal oxidation or by the

conventional patterning process based on resist lithography followed by dry etching of oxide film.[19]

Molecule design

The adsorbate-substrate interaction plays important roles in fabrication of ordered adlayers. Weak adsorbate-substrate interaction will hinder us from producing stable ordered layers due to higher surface mobility of adsorbates. Strong adsorbate-substrate interaction will result in reduced surface diffusion of adsobates due to lower mobility, preventing formation of ordered structures. On the other hand, molecule-molecule interactions need to be strong enough for stable ordered layers. The charge separation in molecules may adjust the intermolecular force, producing thermodynamically stable structures. Table 1 shows a set of potential organic molecules that we proposed to investigate. This table is not an all-exclusive list, but provides initial collection of interesting molecules to investigate. The proposed organic molecules are all

composed of homogeneous aromatic rings. The planar π systems of the rings are expected to have a flat orientation due to their tendency to maximize the π bonding to the surface, providing adequate adsorbate-substrate interaction. And also, it makes STM observations easier because the benzene rings are imaged as circular protrusions. Another interesting aspect for the proposed molecules is that their functional groups can make possible intermolecular interactions between adjacent molecules in terms of inductive and resonance effects. The polarization of π conjugation system by the influence of a substituted group can induce partial negative and positive charges on the molecules, resulting in dipolar interactions between adjacent molecules such as hydrogen bonding. For example, aniline can have charge separated resonance structures [Table 1 (a)]. Ortho and para position of the ring have partial negative charges and nitrogen group has a positive charge. These charge separation of one molecule can act as driving force of intermolecular interaction. Moreover, if dielectric materials provide additional charges and polarities to these molecules, the molecular interactions and orientations can be

modified and adjusted.

Fabrication of dielectric islands

The first approach of this proposed research will be fabrication of dielectric islands on Au (111) surface. As a first step, the reconstructed Au (111) surface will be prepared from the repeated cycles of sputtering and annealing under the UHV environment as described in system design section. Aluminum dioxide (Al_2O_3) islands will be used as a primary dielectric material due to its higher efficiency as a capacitor (higher dielectric constant, ε_0 = 10.95) and simple preparation on Au. As a first step for the fabrication of dielectric islands (Al_2O_3), Al will be evaporated on the reconstructed Au (111) surface. It has been reported that the size and density of Al islands can be controlled by adjusting substrate temperature.[20] Figure 2 shows STM images of the evolution of Al island density, size and shape as a function of deposition temperatures on Au(111) (Θ=0.1 ML and F=3.1 X 10^{-4} ML/s). The density of islands decreases and the

diameter of the islands increases with the temperature due to the increasing mean free path of diffusing adatoms prior to nucleation while the Al islands are homogeneously distributed on the substrate terraces. For the atomic scale STM study of potential induced phase transition and orientation, Al islands with the diameters less than 5nm will be prepared at 200K by evaporating Al from a Knudsen cell (less than 0.01 ML coverage). After preparation of Al islands, thermal oxidation of the sample under the O_2 gas environment will produce oxide layer above Al islands as shown in Figure 1. The island size and oxide thickness will be a critical factor to store the applied electric field since the capacitance depends on oxide surface area and thickness. The oxide surface area, thus island size, can be controlled by substrate temperature during Al evaporation. The oxide thickness can be adjusted by varying O_2 exposure time, oxidation periods and temperatures. On the other hands, the reconstructed Au (111) surface has the lowest tendency to react with O_2 to form oxide even when heated and thus will be quite stable during oxidation. [9]

Potential induced phase transition and molecular orientation

After preparation of dielectric islands, we will begin to investigate potential induced phase transition and molecular orientation. Molecules will be deposited onto the surface by sublimation from a resistively heated boron nitride crucible, monitored by QCM (quartz crystal micro-balence) for the precise control of the amount of molecules. Volatile molecules with high vapor pressure can be easily admitted to the STM chamber via a leak valve attached to the chamber. We will first try 1-notronaphthanlene [Table 1 (f)] since it has a high vapor pressure and its asymmetric molecular geometry will make clear phase transition and orientation in the STM image. After deposition of molecules on the surface, STM study without applied electric field will be performed to characterize topological STM images of the individual molecules. We may need to cool down the sample using low temperature facility if surface mobility of the molecule is too high to obtain stable STM image.

Once stable and clear STM image is obtained, a voltage pulse will be applied to the tip to electrically charge up the dielectrics. [Figure 3 (a) and (b)]. The STM tip is moved to a position over the particular dielectric island. The tip sample distance is reduced to less than 0.1nm to prevent current dissipation to the Au surface while the feedback loop is off.[21,22] Negative voltage pulse to the tip will result in negative charge up to the dielectric islands, which will act as an induced dipole for the molecules to be lined up [Figure 3 (a) and (b)]. After the voltage pulse, the tip will be recessed back to the observation position and image the surface. However, the stored charges in the dielectric layer will be dissipated through discharging process to the ground as well as a form of the heat with a time.[19] After charge dissipation, the ordered array may or may not maintain their structure, depending on the strength of intrinsic dipoles. Here, we will apply opposite tip voltage pulse to the dielectric islands, which will make the orientation of the molecules to reverse direction [figure 4 (a) and (b)]. STM investigations of the whole processes will allow molecules to be observed while rearranging into their new

orientation. This will provide us with kinetic information of the transition and thermodynamic stability of adlayers. The main hypothesis of the potential induced phase transition and orientation using a voltage pulse is that dielectric material can retain required electric field for the molecular orientation and transitions. Therefore, the first objective of this proposed research would be focus on finding reproducible voltage pulse conditions such as applied bias, current, and pulse duration time. If necessary, we may need to spend more time on fabricating appropriate dielectric islands related to the oxide thickness and island size for the efficient charge storage.

Once we obtain reproducible voltage pulse conditions for electrical charge up to the dielectric layer, next objective will be dynamic analysis of the molecules and determination of rate of the potential induced phase transition from the *in situ* STM observation. Imaging the surface during the change of polarities will visualize induced molecular transition and reorientation. If the induced charge is high enough, it may induce intermolecular interactions between adjacent molecules. The STM observation of

these whole processes will provide obvious proof of the molecular transition and orientations by induced dipoles. And also, by measuring a capacitance, we can predict the charges required for the individual molecular transition and orientation. The capacitance (C) of each dielectric layer can be measured by scanning capacitance microscope (SCM) or *in situ* STM using the same probe and input electronics.[23] From the capacitance (C) measurement, the stored charges (Q) in dielectric layers can be calculated through the relationship C=QA/V where A is the surface area and V is the applied voltage, respectively. If we apply voltage pulse to different size of dielectric islands and determine statistically the number of molecules responding to the applied charges, then a good idea of the required charges (Q) for the individual molecular phase transition can be obtained.

As mentioned earlier, we may need to use low temperature STM using liquid He or N_2. However, the phase transitions and reorientations may not occur at low temperature where molecules are strongly bound to the substrate. In order to overcome

the activation barrier for the transition and orientation, the substrate temperature needs to be increased gradually and we can determine the temperature required for the transition and reorientation. Alternatively, the temperature can be kept constant at a certain point and transition time can be measured for the individual molecular transition. If we statistically determine the individual molecular transitional rate at a certain capacitance, the activation barrier for the transition or reorientation can be determined from the Arrhenius relationship.

After we can observe potential induced phase transition and molecular orientation, the experiments will be expanded to the systemic investigations of molecules that we proposed to investigate. Table 1 is presented in a fashion that a molecular aromatic composition increase from top to bottom with different substituted group. The different polarity of substituted groups will allow for the determination of how the polarity can affect the potential induced phase transition and orientations while maintaining constant aromatic contents. Increase of aromatic size of the molecules with

same polarity will suggest how molecular-substrate interactions (π bonding) affect on the phase transition and orientation. Steric effects of substituted groups, vapor pressure of molecules, and molecular weight will also be analyzed to determine if any relation to the molecular transition and orientation exists. The molecules with both electron withdrawing and donating group will show how the interactions of substituted groups can affect on phase transition and reorientation. [Table 1 (n) and (o)] This dynamic piece of understanding for the system will allow for fundamental rules of potential induced phase transition to be determined, allowing for the predictions of charges and polarities for the transition and orientation as well as their stability.

Another interesting approach for this study is to investigate photochemically interesting molecules such as azobenzene, which also can have a charge separation in molecules [Table 1 (p)].[10] The major feature of azo group is its capability of photo and thermal isomerization into E-Z forms as shown in Table 1 (q).[9] On E-Z conversion, it changes its absorption spectrum considerably and its molecular shape, increasing the

dipole moment from 0 to 3 Debye and reducing the molecular maximum distance from 1.0nm to 0.59nm.[10] In this study, kinetic and thermodynamic information for each isomer can be obtained through the potential induced phase transition. Besides, *in situ* UV/VIS illumination of sample during STM observations of the phase transition and orientation will provide a good idea related to the role of dipole moments in the phase transitions and orientations.

This proposed research can reveal many fundamental principles concerning potential induced phase transitions, orientations, and molecular interactions. The development of a fundamental set of rules will provide the ability to predict intermolecular interaction, molecular structures to be formed, and the rate at which the change will occur. Understanding of this phenomenon coming from the basic interactions of the constituent molecules will lead to development of new methods to controlling the self-assembled organic films with desired orientation.

Additional studies

The electronic properties of the molecules may affect on the potential induced transition and orientation through a different electron transfer process. In addition to the conventional topological image of the adlayers, STM studies of individual adsorbates will provide us spectroscopic information as a function of location. STS (Scanning Tunneling Spectroscopy) allow us to measure electronic properties such as DOS (density of states) of adsorbates on atomic scale by measuring the tunneling current as a function of tunneling bias at various positions on the sample. CITS (Current Imaging Tunneling Spectroscopy) will provide additional insight into the nature of the local electronic characteristics and the interactions between the adsorbates and substrate by mapping out complete electronic structures of the surface. At the same time, x-ray photoelectron and ultraviolet photoelectron spectrometers (XPS and UPS) will be useful to obtain the valence band spectra of the adsorbates. The correlation of these results to the CITS spectra will provide reliable information about the molecular electronic properties and

their interactions.

Reference

[1] B. Dong, F. Huo, L. Zhang, X. Yang, Z. Wang, X. Zhang, S. Gong, and J. Li, Chem. Eur. J. **9,** 2331-2336 (2003).

[2] J. J. W. M. Rosink, M. A. Blauw, L. J. Geerings, E. Van Der Drift, and E. J. M. Fakkeldij, langmuir **16,** 4547-4553 (2000).

[3] I. J. Campbell, J. D. Kress, R. L. Martin, D. L. Smith, N. N. Barashkov, and J. P. Ferraris, Appl. Phys. Lett. **71,** 3528-3530 (1997).

[4] M. Eremtchenko, J. A. Schaefer, and F. S. Tautz, Nature **425,** 602-605 (2003).

[5] N. Katsonis, A. Marchenko, S. Taillemite, D. Fichou, G. Chouraqui, C. Aubert, and M. Malacria, Chem. Eur. J. **9,** 2574-2581 (2003).

[6] S. W. Lee, H. A. MacNally, D. Guo, M. Pingle, D. E. Bergstrom, and R. Bashir, Langmuir **18,** 3383-3386 (2002).

[7] N. Katsonis, A. Marchenko, and D. Fichou, J. Am. Chem. Soc. **125,** 13682-13683 (2003).

[8] A. R. MacDairmid, M. C. Gallagher, and J. T. Banks, J. Phys. Chem. B **107,** 9787-9792 (2003).

[9] M. Rosoff, *Nano-surface Chemistry* (Marcel Dekker, New York, 2002).

[10] Z. Sekkat and W. Knoll, *Photoreactive organic thin films*, Vol. 1 (Elsevier Science, New York, 2002).

[11] Y. He, T. Ye, and E. Borguet, J. Am. Chem. Soc. **124,** 11964-11970 (2002).

[12] F. Cunha and N. J. Tao, Phys. Rev. Lett. **75,** 2376-2379 (1995).

[13] F. Cunha, N. J. Tao, X. W. Wang, Q. Jin, B. Duong, and J. D'Agnese, langmuir **12,** 6410-6418 (1996).

[14] P. G. Gennis and J. Prost, *The Physics of Liquid Crystals* (Oxford University, 1993).

[15] M. Bohringer, W. Schneider, and R. Berndt, Angew. Chem. Int. Ed. **39,** 792-795 (2000).

[16] M. Bohringer, W. Schneider, and R. Berndt, Surf. Rev. Lett. **7,** 661-666 (2000).

[17] M. Bohringer, K. Morgenstern, W. Schneider, and R. Berndt, J. Phys.: Condens. Matter **11,** 9871-9878 (1999).

[18] C. Galassi, M. Dinescu, K. Uchino, and M. Sayer, *Piezoelectric materials: Advances in Science, Technology, and application*, Vol. 76 (Kluwer Academic, Belgium, 2000).

[19] S. M. Sze, *VLSI Technology*, 3 ed. (McGraw-Hill, New York, 1988).

[20] B. Fischer, H. Brune, J. V. Barth, A. Fricke, and K. Kern, Phys. Rev. Lett. **82,** 1732-1735 (1999).

[21] S. Kondo, S. Heike, M. Lutwyche, and Y. Wada, J. Appl. Phys. **78,** 155-160 (1995).

[22] S. Hosoka, S. Hosoki, T. Hasegawa, and M. Miyamoto, J. Vac. Sci. Technol. B **13,** 2813-2818 (1995).

[23] S. Lanyi and M. Hruskovic, Rev. Sci. Instrum. **73,** 2923-2927 (2002).

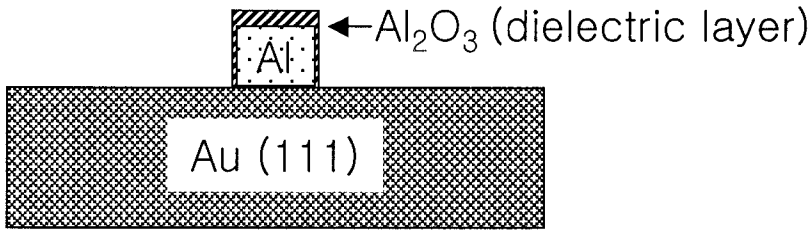

Figure 1. Schematic of proposed dielectric materials (Al_2O_3) on Au (111) surface

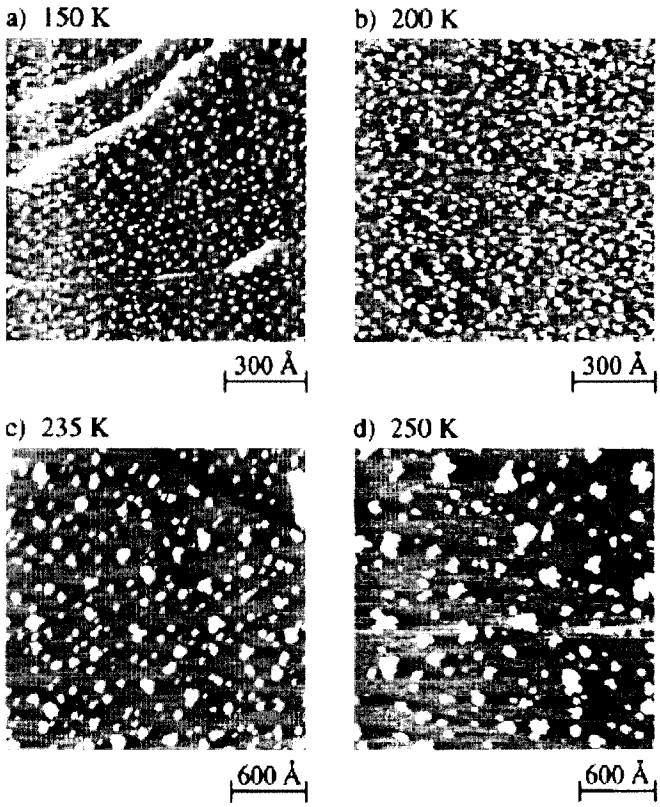

Figure 2. STM images [(a)-(d)] showing the evolution of island density, size, and shape as a function of temperature for Al deposition onto Au(111) [Θ=0.1ML and F=3.1 X 10^{-4}ML/sec]

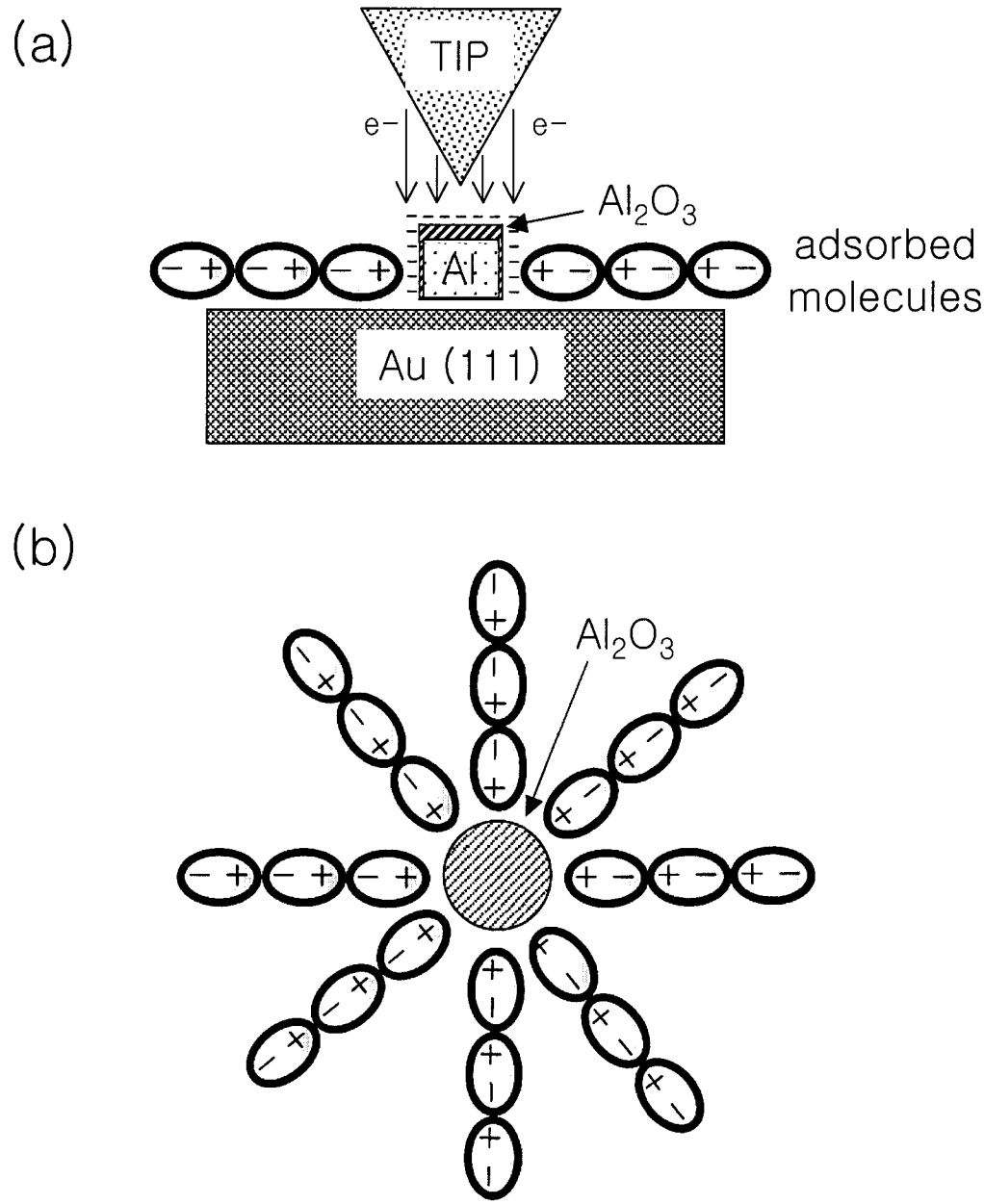

Figure 3. (a) Side view and (b) Top view of negative voltage pulse applied to the dielectric layer from the STM tip

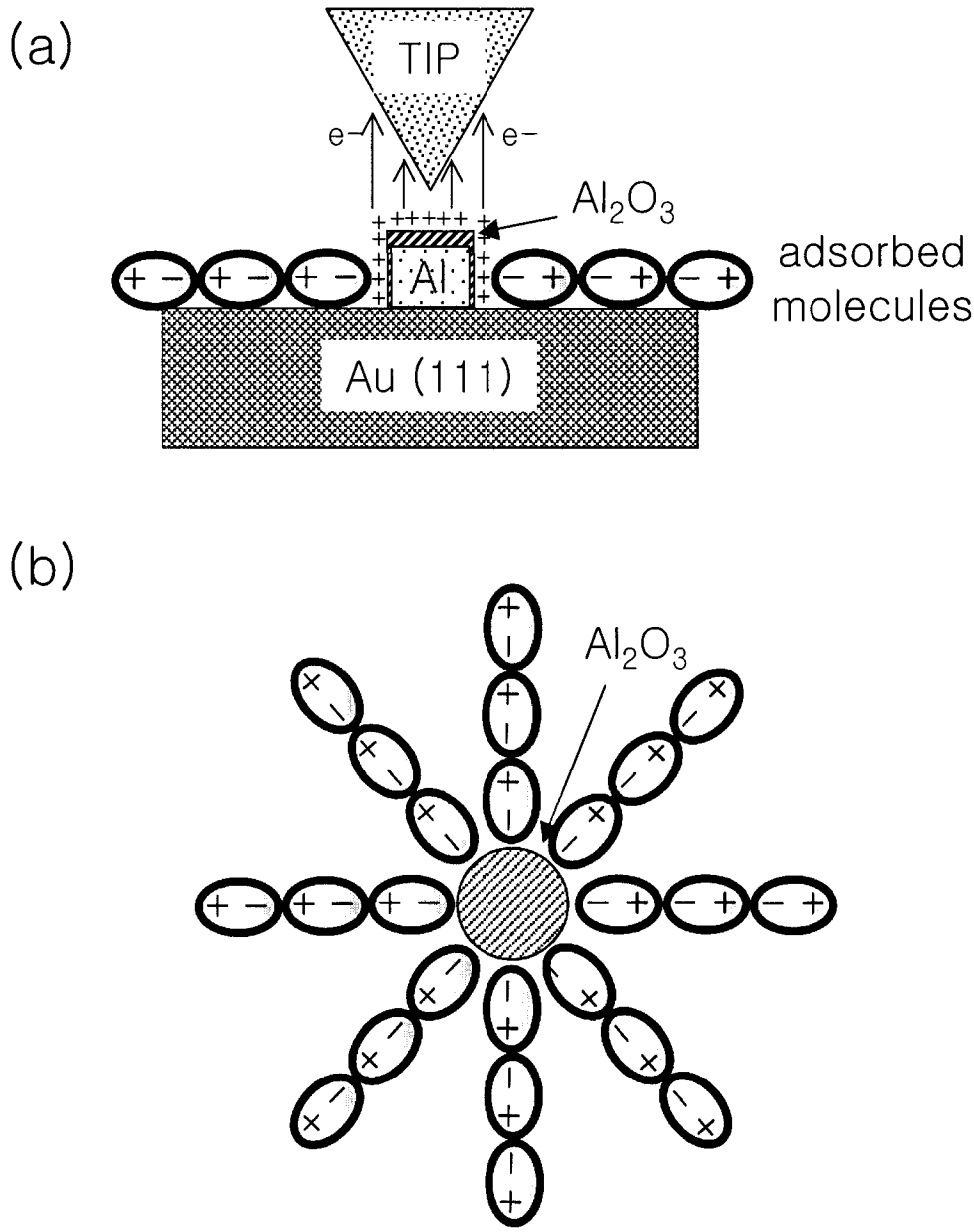

Figure 4. (a) Side view and (b) Top view of positive voltage pulse applied to the dielectric layer from the STM tip

Table 1.

Proposed Molecules for the phase transition and orientation

a) 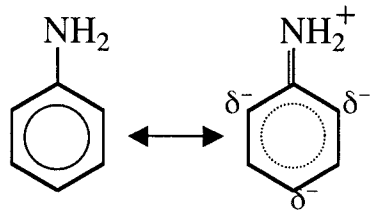

b) 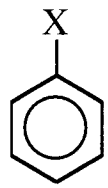

X = Cl, Br, or I

c) 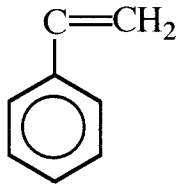

d) 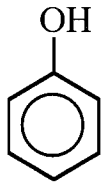

e) 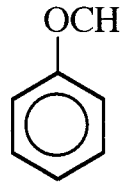

f) 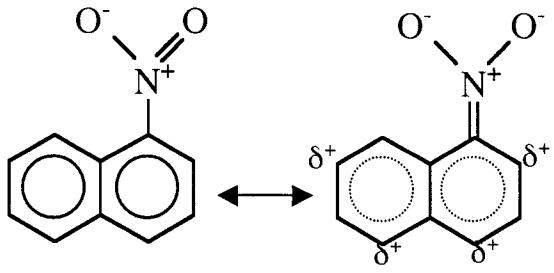

g) 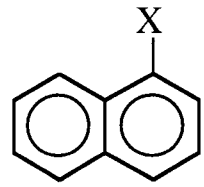

X = Cl, Br, I, NH_2 OH, or $CH = CH_2$

h) 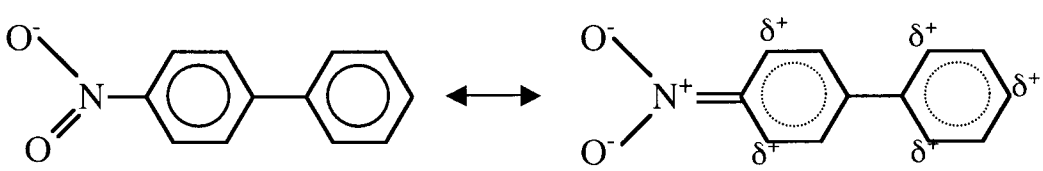

i) 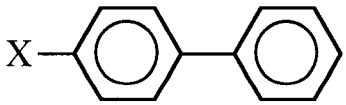

X = Cl, Br, I, NH_2, OH, or $CH = CH_2$

Proposed Molecules for the phase transition and orientation

j)

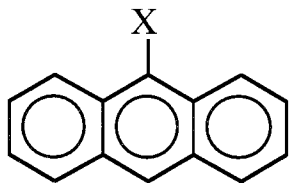

k)

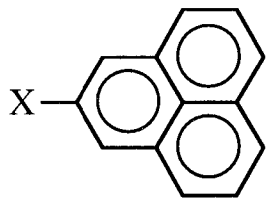

l)

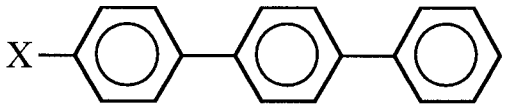

m)

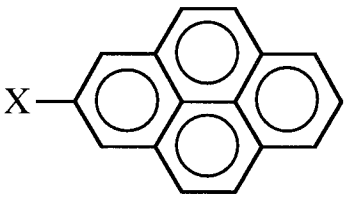

X = Cl, Br, I, NH_2, NO_2, OH, or $CH = CH_2$

n)

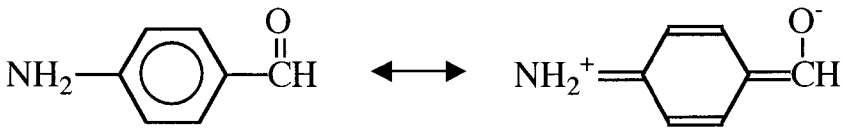

o)

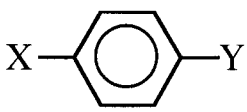

X = Cl, Br, I, NH_2, OH, or $CH = CH_2$

Y = COH, $COCH_3$, or NO_2

p)

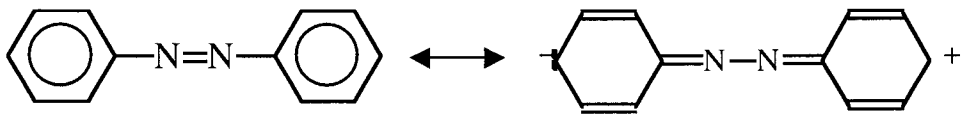

q)

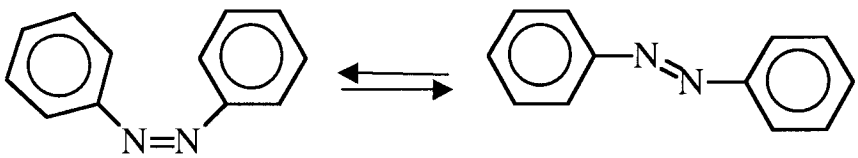

Z-form E-form